

Direct Photon - Hadron Correlations Measurement in Au+Au Collision at Nucleon  
Center-Of-Mass Energy of 200 GeV With Isolation Cut Methods

A dissertation presented to  
the faculty of  
the College of Arts and Sciences of Ohio University

In partial fulfillment  
of the requirements for the degree  
Doctor of Philosophy

Nowo Rivel  
August 2014  
© 2014 Nowo Rivel. All Rights Reserved.

This dissertation titled

Direct Photon - Hadron Correlations Measurement in Au+Au Collision at Nucleon  
Center-Of-Mass Energy of 200 GeV With Isolation Cut Methods

by

NOWO RIVELI

has been approved for

the Department of Physics and Astronomy

and the College of Arts and Sciences by

Justin Frantz

Professor of Department of Physics and Astronomy

Robert Frank

Dean of College of Arts and Sciences

## Abstract

RIVELI, NOWO, Ph.D., August 2014, Physics

Direct Photon - Hadron Correlations Measurement in Au+Au Collision at Nucleon Center-Of-Mass Energy of 200 GeV With Isolation Cut Methods (160 pp.)

Director of Dissertation: Justin Frantz

Quark Gluon Plasma (QGP), a hot and dense medium that consists of deconfined quarks and gluons, have been created in heavy ion collisions both at RHIC and LHC. Properties of the medium are investigated via measurements of the energy loss of hard scattered partons that travel through the medium, which manifest themselves as jets on the detector. Partonic energy loss is represented by the modification of the fragmentation function of the parton. In this dissertation, modification of the fragmentation function is examined through the measurement of direct photon - hadron pair correlations, both in gold+gold (Au+Au) and proton+proton (p+p) collision systems at RHIC, using the data collected by PHENIX in 2007 and 2010. Direct photons are produced at leading order mainly via Compton scattering of a gluon from a quark, and secondarily via quark-antiquark annihilation. Direct photons do not interact with the medium since it is colorless, therefore its momentum provides the unmodified initial momentum of the opposing parton, and it is used as a reference in determining the fraction of the momenta ( $z$ ) of the opposing hadrons. The fragmentation function is represented by the conditional yield of the away-side hadrons. The medium induced modification of the fragmentation function is obtained from the ratio of its value when measured in

Au+Au and in p+p, defined as  $I_{AA}$ . To reduce the uncertainties in the direct photon measurement, isolation cut technique is implemented to improve the ratio of direct photon signals over the background that primarily consists of hadronic decay photons. It is shown from the final results that indeed isolation cut has produced a level of improvement. A non-constant behavior of the  $I_{AA}$  as function of  $z$  at the most central Au+Au events is observed. This is interpreted as a mechanism in which the energy loss of high  $p_T$  particles is redistributed to the production of lower  $p_T$  particles. Measurement of the direct photon - hadron correlations is also performed over more peripheral (less dense) events, and the non-constant feature of the  $I_{AA}$  seems to shows dependency on the medium density. Measurement of the away-side hadronic conditional yields on several centrality bins and different integration ranges, with an improved significance that is obtained by means of isolation cut, can provide additional constraints in understanding the physics mechanism of the partonic energy loss in the medium.

*To Mom and Dad, Fitri, Fatima, Hammam and Hasan.*

*I am coming home soon.*

## Acknowledgements

I would like to first of all thank my advisor Justin Frantz for his guidance throughout my study years. From him I received invaluable training in becoming better researcher in the field of experimental physics. His support extended from encouraging independent study, to providing assistance of sorting out the sloppy details of data analysis, which manifest in late-night stays at the office. Through him I also obtained the opportunity of getting involved in large scale physics experiments; being a part of PHENIX collaboration, as well the inestimable experience of conducting a short experiment at CERN. Those are privileges for me, and I can only hope for whatever I will do in the future I can exploit the lessons that I gain to provide contributions in any kind of ways. I didn't have a lot of chances to meet and get to know the many people of PHENIX the collaboration, but I am fully aware that I am indebted to every single one. Without the work on the so many components of PHENIX experiment, the completion of this dissertation would not have been possible. I would like to express my gratitude particularly to Ali Hanks and Megan Connors, who provided help and guidance based on their experience of working on similar analysis. I would also like to express my acknowledgement to all my classmates, and the Indonesian community in Athens; this experience would have been different without their friendship and togetherness. And lastly, my gratitudes goes to my family back home in Indonesia; their constant long distance support has been priceless.

Funding from the US NSF supported most of the research in this thesis.

## Table of Contents

	Page
Abstract . . . . .	3
Dedication . . . . .	5
Acknowledgements . . . . .	6
List of Tables . . . . .	9
List of Figures . . . . .	10
 1 Introduction . . . . .	17
1.1 Quarks and Gluons . . . . .	18
1.2 Relativistic Heavy Ion Collision . . . . .	21
1.3 QGP Signatures in Heavy Ion Collisions . . . . .	25
1.3.1 Harmonic flow . . . . .	25
1.3.2 Single particle suppression . . . . .	27
1.3.3 Jet suppression . . . . .	28
1.4 Fragmentation Function Measurement Through $\gamma_{\text{dir}} - h$ Pair Correlations	31
1.5 Mechanism of Energy Loss . . . . .	35
1.6 Purpose of the Dissertation . . . . .	37
 2 Experiment Details . . . . .	39
2.1 RHIC Accelerator . . . . .	39
2.2 PHENIX Detector . . . . .	40
2.2.1 Event Characterization . . . . .	41
2.2.2 Central Arm Spectrometer . . . . .	47
2.3 Summary of PHENIX DATA . . . . .	53
 3 Analysis Methods . . . . .	56
3.1 Two-particle correlations . . . . .	56
3.1.1 Acceptance correction . . . . .	57
3.1.2 Combinatorial Background . . . . .	59
3.1.3 Per-trigger yield . . . . .	65

3.2	$\gamma_{\text{dir}} - h$ pair correlations . . . . .	66
3.2.1	Direct Photon Measurement: The Statistical Subtraction Method	66
3.2.2	Decay Photon Measurement . . . . .	67
3.2.3	$\pi^0$ Measurement . . . . .	72
3.2.4	Charged hadron efficiency . . . . .	75
4	Additional Cuts and Data Selections . . . . .	80
4.1	Isolation cut . . . . .	80
4.1.1	Optimization . . . . .	82
4.1.2	Modification of the decay mapping . . . . .	85
4.1.3	Modification of the $R_\gamma$ . . . . .	87
4.1.4	Modification of $v_2$ . . . . .	88
4.2	Data selection . . . . .	89
4.2.1	Event selection . . . . .	89
4.2.2	Photon Selection . . . . .	90
4.2.3	Hadron Selection . . . . .	91
4.3	Energy Re-Calibration of the EMCAL Detector . . . . .	93
5	Simulation Study . . . . .	96
5.1	Statistical method . . . . .	97
5.2	Isolation cut method . . . . .	101
5.3	Conclusions of the Simulation Study . . . . .	104
6	Studies of the modification of the fragmentation function . . . . .	107
6.1	p+p measurement . . . . .	107
6.2	Au+Au measurement . . . . .	109
7	Results And Discussions . . . . .	114
7.1	$\Delta\phi$ distribution . . . . .	115
7.2	The integrated yields . . . . .	117
7.3	Systematic uncertainties . . . . .	119
7.3.1	Sources of the systematic uncertainties . . . . .	120
7.3.2	Propagation of the systematic uncertainties . . . . .	123
7.4	Physics Discussions . . . . .	124
7.4.1	High $z_T$ suppression . . . . .	124
7.4.2	Low $z_T$ enhancement . . . . .	127
8	Summary . . . . .	134
	References . . . . .	138
	Appendix: Plots . . . . .	141

## List of Tables

Table	Page
1.1 Quark flavors. . . . .	19
2.1 Summary of the data sets collected by PHENIX. Information collected from [21, 30]. . . . .	55
4.1 The parameters of isolation cut used in this analysis. . . . .	85

## List of Figures

Figure	Page
1.1 Measurement and theoretical calculation of $\alpha_s$ as function of energy scale $Q$ [4]. . . . .	20
1.2 Qualitative prediction of phases of QCD matter. Adapted from [5] . . . . .	22
1.3 A cartoon of evolution of the stages in heavy ion collisions. Parts adapted from various publically available sources. . . . .	23
1.4 Diagramatic depiction of the definition of centrality (a) and the reaction plane (b). Parts adapted from various publically available plots including [5] . . . . .	25
1.5 $v_2$ measurements of different particles at RHIC [7]. . . . .	26
1.6 $v_2$ measurements of different particles at RHIC scaled by number of valence quark [7]. . . . .	27
1.7 The $R_{AA}$ measured in PHENIX for $\pi^0$ and $\eta$ [8, 9] and 'direct' photons [10]. Figure is grabbed from [11]. . . . .	28
1.8 Dihadron azimuthal correlation with high $p_T$ trigger in three different collision systems [12]. . . . .	30
1.9 The $e + e-$ fragmentation function for all charged particles is shown (a) for different CM energies $\sqrt{s}$ versus $x (\equiv z)$ and (b) for various ranges of $x$ versus $\sqrt{s}$ . For the purpose of plotting (a), the distributions were scaled by $c(\sqrt{s}) = 10^i$ with $i$ ranging from $i = 0$ ( $\sqrt{S} = 12$ GeV) to $i = 13$ ( $\sqrt{s} = 202$ GeV). Most of these results are published more than 15 years ago. In modern common usage, the variable $z$ is always used for what is notated as $x$ in this plot. The compilation is obtained from the Particle Data Book Review [4]. . . . .	33
1.10 Production of hard direct photons through the processes of Compton scattering (a) and quark-antiquark annihilation (b). . . . .	34
1.11 Calculation of the ratio ( $I_{AA}$ ) of $\gamma_{\text{dir}} - h$ yields in 200 GeV Au+Au and in p+p, from the ASW and YaJEM model. Here $z_T = p_{T,h}/p_{T,\gamma}$ , is an approximate to the scaling variable $x$ . In YaJEM, the branching of the leading parton is tracked down, resulting in the prediction of the enhancement at low $z_T$ , in contrast to an overall suppression predicted from ASW result [14]. . . . .	37

2.1	Aerial view of the RHIC accelerator complex. This marked photograph is taken from publicly available sources. . . . .	39
2.2	Schematic view of the PHENIX detector as seen in the beam direction (top); showing the central arm configuration. And in the side view (bottom); showing the event characterization and the muon arm configurations. [21] . . . . .	42
2.3	A single BBC element consisting of quartz Cherenkov radiator and PMT (left) and a BBC arm with 64 elements (right). [21] . . . . .	43
2.4	Position of ZDCs, BBCs, DX magnets, and the two beam pipes. [21] . .	45
2.5	Two methods of determining centrality classes; The clock division (left) and the BBC only division (right). [21] . . . . .	46
2.6	One arm of the RXPN detector [21]. . . . .	48
2.7	The schematic layout of a DC arm (left) and a DC keynote configuration (right). [26] . . . . .	50
2.8	Principle of the pad geometry [27]. . . . .	51
2.9	A schematic view of one arm of the RICH detector [28]. . . . .	52
2.10	Left: A module of a PbSc detector (1 module = 4 towers). Right: A module of PbGl detector (1 module = 1 tower) [21]. . . . .	54
3.1	Depiction of Acceptance Function of the PHENIX central arms. (a) Coverage region with respect to two azimuthal angles. (b) Coverage region with the horizontal axis being the difference of two azimuthal angle. (c) The Acceptance function that is obtained by projection of (b) to the horizontal axis. . . . .	58
3.2	Example of a correlation function and the combinatoric shapes. In grey is the correlation function. <b>Red</b> is the combinatoric shape in Au+Au following Eq. 3.2 up to the second harmonics. <b>Blue</b> is the combinatoric shape in p+p that follows a flat line. . . . .	60
3.3	The background level $b_0$ is determined from the minimum of the fit to the correlation functions. . . . .	62
3.4	The distribution of triggers (top) and partners (bottom) with respect to $N_{part}$ (left) and $N_{coll}$ (right), and two fit functions. . . . .	64
3.5	The probability function of $N_{part}$ and $N_{coll}$ from the calculation using GMC. .	65
3.6	Top: Three different probability functions; analytic (dashed black), Monte Carlo without merging effect (solid red) and Monte Carlo with merging effect (data point). Bottom: The correction function from the merging effect from full PISA simulation [33]. . . . .	71
3.7	Description of the mapping procedure from the reconstructed $\pi^0$ spectra to decay photon's spectra. . . . .	72
3.8	The signal-to-background ratio in the distribution of the $\pi^0$ invariant mass, in different centrality and $\pi^0 p_T$ . . . . .	75
3.9	The invariant yield of $\pi^0$ production measured in Au+Au collision with $\sqrt{s_{NN}} = 200$ GeV [34], and their power law fit. . . . .	76

3.10	$\pi^0$ trigger efficiency obtained for Run 10. . . . .	76
3.11	The fit function used as single charged hadron efficiency in this analysis. The function parameter on the original result of simulation is obtained from [35]. RICH veto for tracks of $p_T$ below 5 GeV causes the dip around $p_T = 4.7$ GeV. . . . .	78
4.1	Illustration of the working principle of isolation cut in selecting isolated photons. . . . .	81
4.2	Distribution of the cone energy around $\pi^0$ for different $\pi^0$ energies. . . . .	83
4.3	Value of $\sigma s$ . Green line is mean energy of the random cone. The isolation cut parameters are set based on or close to the locations of the minimum $\sigma$ . . . . .	84
4.4	The isolation probability function as function of $\pi^0$ energy for different ranges of decay photon energy. . . . .	87
4.5	The mix background of a bad run compared to the average, and their ratio. . . . .	90
4.6	Example of finding the dead and hot towers. On the left panel, few hot towers register number of hits far right end of the distribution. On the right panel, the dead towers are colored white and the hot towers are colored red. . . . .	92
4.7	The ratio of the charge particle spectra of when $3\sigma$ cut is applied with when $2\sigma$ cut is applied. The left panel is for inclusive charge tracks, right panel is for the conditional charge tracks [33]. . . . .	94
4.8	The peak position of the $\pi^0$ mass measured in the range of $1.0 < p_T^{\pi^0} < 2.0$ , on two different sector, on for each Run number of the Au+Au Run 10 data, before recalibration. . . . .	95
5.1	The $\gamma_{\text{dec}} - h$ pair correlations function of the true and derived decay photons, for the combinations of two trigger $p_T$ bins and five associate $p_T$ bins. . . . .	98
5.2	The $\gamma_{\text{dec}} - h$ pair jet functions of the true and derived decay photons. . . . .	99
5.3	The % - error of the derived from the true $\gamma_{\text{dec}} - h$ pair correlation functions, background, and jet functions, in terms of $z_T$ , in all centralities. The yellow band indicates 2% ranges. . . . .	99
5.4	The $\gamma_{\text{dir}} - h$ pair jet functions of true and derived direct photons. . . . .	100
5.5	The percent difference of the derived with the true $\gamma_{\text{dir}} - h$ pair jet functions, in terms of $z_T$ and in all centralities. The yellow band indicates a 20% ranges. . . . .	101
5.6	The isolated $\gamma_{\text{dec}} - h$ pair correlations function of true and derived decay photons. . . . .	102
5.7	The isolated $\gamma_{\text{dec}} - h$ pair jet functions of true and derived decay photons. . . . .	103
5.8	The % - error of the derived from the true $\gamma_{\text{dec}} - h$ pair correlation functions, background, and jet functions, in terms of $z_T$ , in all centralities. Isolation cut is applied. The yellow band indicates 2% ranges. . . . .	103

5.9	The $\rho$ factor obtained from true and derived decay photons. The 'true' value is shown in red and the 'derived' is shown in black. . . . .	104
5.10	The isolated $\gamma_{\text{dir}} - h$ pair jet functions of true and derived direct photons. . . . .	106
5.11	The percent difference of the derived with the true isolated $\gamma_{\text{dir}} - h$ pair jet functions, in terms of $z_T$ and in all centralities. . . . .	106
6.1	$x_E$ distribution of the away-side yield of $\pi^0 - h$ (left) and $\gamma_{\text{dir}} - h$ (right) correlations measured in p+p [16]. The dashed line is a fit to an exponential function and the solid line is a fit to the Hagedorn function. . . . .	109
6.2	$\xi$ distribution for isolated direct photon data in $p + p$ for all $p_T$ ranges combined compared to TASSO measurement in $e^+e^-$ collisions at $\sqrt{s} = 14$ and 44 GeV [16]. . . . .	110
6.3	$\xi$ distribution of the away-side yield of $\gamma_{\text{dir}} - h$ correlations measured in p+p and in Au+Au (top), and the ratio of the two (bottom) [17]. The corresponding $z_T$ scale is also shown on the top axis. . . . .	111
6.4	The averaged $I_{AA}$ as function of centrality [40]. The same measurement with improvement is obtained and will be discussed in the next Chapter. . . . .	113
7.1	The jet functions of $\gamma_{\text{inc}} - h$ , $\gamma_{\text{dec}} - h$ and $\gamma_{\text{dir}} - h$ pairs 0 – 20% Au+Au. . . . .	115
7.2	The jet functions of $\gamma_{\text{inc}} - h$ , $\gamma_{\text{dec}} - h$ and $\gamma_{\text{dir}} - h$ pairs 0 – 20% Au+Au with isolation cut applied. . . . .	116
7.3	The integrated away-side yields of the full region ( $ \Delta\phi - \pi  < \pi/2$ ) in p+p and in Au+Au for all centralities. The Au+Au yields on the left panel are obtain without the isolation cut, and on the right panel are obtained with the isolation cut applied. The solid lines are (exponential $\times$ power law) function, used to fit the data plots for illustration. . . . .	119
7.4	The $I_{AA}$ from each centrality obtained from the integration of the full away-side region ( $ \Delta\phi - \pi  < \pi/2$ ), without isolation cut. Different colors represent different trigger $p_T$ bins. The solid brown line is a constant function fitted the the $I_{AA}$ , the solid yellow lines are constant functions fitted to the upper and lower systematic values of the $I_{AA}$ . A solid grey curve is also shown, it is obtained from the ratio of the fit function used in the away-side yield (Fig.7.3). . . . .	120

7.5	The $I_{AA}$ from each centrality obtained from the integration of the full away-side region ( $ \Delta\phi - \pi  < \pi/3$ ), with the isolation cut applied. Different colors represent different trigger $p_T$ bins. The solid brown line is a constant function fitted to the $I_{AA}$ , the solid yellow lines are constant function fitted to the upper and lower systematic values of the $I_{AA}$ . A solid grey curve is also shown, it is obtained from the ratio of the fit function used in the away-side yield (Fig. 7.3 right). The results are qualitatively similar to those in Fig. 7.4, but with smaller integration region. When compared to the published data [17], the results shown in this figure differ in that they only include $p_{T,\text{assoc}} > 1$ GeV, not $p_{T,\text{assoc}} > 0.5$ GeV. The enhancement at low $z_T$ is not as pronounced (as in Fig. 7.4), which is consistent with the published result [17]. . . . .	121
7.6	The $I_{AA}$ averaged over the high $z_T$ regions as function of $N_{part}$ from the measurement over Run 4 data [40], compared with the $\pi^0 R_{AA}$ [34]. . . . .	126
7.7	The $I_{AA}$ averaged over the high $z_T$ regions as function of $N_{part}$ from the combined Run 7 and Run 10 data without isolation cut applied. . . . .	126
7.8	The $I_{AA}$ averaged over the high $z_T$ regions as function of $N_{part}$ from the combined Run 7 and Run 10 data with isolation cut applied. . . . .	127
7.9	The $I_{AA}$ recently published in [17] to which the analysis in this dissertation made contributions to as well, established a statistically significant enhancement of the fragmentation yield in the low $z_T$ region. . . . .	128
7.10	(a) The averaged $I_{AA}$ on the low $z_T$ regions (blue). The averaged $I_{AA}$ over the high $z_T$ region (red) is shown again here for reference, (b) ratio of the low $z_T$ average to the high $z_T$ average. These results are obtained without isolation cut applied. . . . .	129
7.11	The $I_{AA}$ as function of $\xi$ , on the central 0 – 40% centrality bins of the combined Run 7 and Run 10, evaluated at different sizes of integration range [17]. The transformation to the $z_T$ axis is also shown. . . . .	131
7.12	(a) The averaged $I_{AA}$ on the low $z_T$ regions (blue) and on the high $z_T$ region (red) is shown again here for reference, (b) ratio of the low $z_T$ average to the high $z_T$ average. These results are obtained with the isolation cut applied. . . . .	132
7.13	The $I_{AA}$ averaged over low $z_T$ region as function of $N_{part}$ , obtained with the isolation cut applied and using the three different values of $v_2$ for the isolated inclusive and decay photons. . . . .	133
A.1	Correlations function and combinatoric background of $\gamma_{\text{inc}} - h$ pairs in 0 – 20% Au+Au with statistical method. The $x$ -axis is the $\Delta\phi$ . . . . .	141
A.2	Correlations function and combinatoric background of $\pi^0 - h$ pairs in 0 – 20% Au+Au with statistical method. The $x$ -axis is $\Delta\phi$ . . . . .	142
A.3	Correlations function and combinatoric background of $\gamma_{\text{dec}} - h$ pairs in 0 – 20% Au+Au with statistical method. The $x$ -axis is $\Delta\phi$ . . . . .	142

A.4 Correlations function and combinatoric background of $\gamma_{\text{inc}} - h$ pairs in 20 – 40% Au+Au with statistical method. The $x$ -axis is $\Delta\phi$ . . . . .	143
A.5 Correlations function and combinatoric background of $\pi^0 - h$ pairs in 20 – 40% Au+Au with statistical method. The $x$ -axis is $\Delta\phi$ . . . . .	143
A.6 Correlations function and combinatoric background of $\gamma_{\text{dec}} - h$ pairs in 20 – 40% Au+Au with statistical method. The $x$ -axis is $\Delta\phi$ . . . . .	144
A.7 Correlations function and combinatoric background of $\gamma_{\text{inc}} - h$ pairs in 40 – 60% Au+Au with statistical method. The $x$ -axis is $\Delta\phi$ . . . . .	144
A.8 Correlations function and combinatoric background of $\pi^0 - h$ pairs in 40 – 60% Au+Au with statistical method. The $x$ -axis is $\Delta\phi$ . . . . .	145
A.9 Correlations function and combinatoric background of $\gamma_{\text{dec}} - h$ pairs in 40 – 60% Au+Au with statistical method. The $x$ -axis is $\Delta\phi$ . . . . .	145
A.10 Correlations function and combinatoric background of $\gamma_{\text{inc}} - h$ pairs in 60 – 92% Au+Au with statistical method. The $x$ -axis is $\Delta\phi$ . . . . .	146
A.11 Correlations function and combinatoric background of $\pi^0 - h$ pairs in 60 – 92% Au+Au with statistical method. The $x$ -axis is $\Delta\phi$ . . . . .	146
A.12 Correlations function and combinatoric background of $\gamma_{\text{dec}} - h$ pairs in 60 – 92% Au+Au with statistical method. The $x$ -axis is $\Delta\phi$ . . . . .	147
A.13 Correlations function and combinatoric background of $\gamma_{\text{inc}} - h$ pairs in 0 – 20% Au+Au with isolation cut method. The $x$ -axis is $\Delta\phi$ . . . . .	148
A.14 Correlations function and combinatoric background of $\pi^0 - h$ pairs in 0 – 20% Au+Au with isolation cut method. The $x$ -axis is $\Delta\phi$ . . . . .	149
A.15 Correlations function and combinatoric background of $\gamma_{\text{dec}} - h$ pairs in 0 – 20% Au+Au with isolation cut method. The $x$ -axis is $\Delta\phi$ . . . . .	149
A.16 Correlations function and combinatoric background of $\gamma_{\text{inc}} - h$ pairs in 20 – 40% Au+Au with isolation cut method. The $x$ -axis is $\Delta\phi$ . . . . .	150
A.17 Correlations function and combinatoric background of $\pi^0 - h$ pairs in 20 – 40% Au+Au with isolation cut method. The $x$ -axis is $\Delta\phi$ . . . . .	150
A.18 Correlations function and combinatoric background of $\gamma_{\text{dec}} - h$ pairs in 20 – 40% Au+Au with isolation cut method. The $x$ -axis is $\Delta\phi$ . . . . .	151
A.19 Correlations function and combinatoric background of $\gamma_{\text{inc}} - h$ pairs in 40 – 60% Au+Au with isolation cut method. The $x$ -axis is $\Delta\phi$ . . . . .	151
A.20 Correlations function and combinatoric background of $\pi^0 - h$ pairs in 40 – 60% Au+Au with isolation cut method. The $x$ -axis is $\Delta\phi$ . . . . .	152
A.21 Correlations function and combinatoric background of $\gamma_{\text{dec}} - h$ pairs in 40 – 60% Au+Au with isolation cut method. The $x$ -axis is $\Delta\phi$ . . . . .	152
A.22 Correlations function and combinatoric background of $\gamma_{\text{inc}} - h$ pairs in 60 – 92% Au+Au with isolation cut method. The $x$ -axis is $\Delta\phi$ . . . . .	153
A.23 Correlations function and combinatoric background of $\pi^0 - h$ pairs in 60 – 92% Au+Au with isolation cut method. The $x$ -axis is $\Delta\phi$ . . . . .	153
A.24 Correlations function and combinatoric background of $\gamma_{\text{dec}} - h$ pairs in 60 – 92% Au+Au with isolation cut method. The $x$ -axis is $\Delta\phi$ . . . . .	154

A.25 Jet function of $\gamma_{\text{inc}} - h$ , $\gamma_{\text{dec}} - h$ and $\gamma_{\text{dir}} - h$ pairs in 0 – 20% Au+Au with statistical method. The $x$ -axis is $\Delta\phi$ .	155
A.26 Jet function of $\gamma_{\text{inc}} - h$ , $\gamma_{\text{dec}} - h$ and $\gamma_{\text{dir}} - h$ pairs in 20 – 40% Au+Au with statistical method. The $x$ -axis is $\Delta\phi$ .	156
A.27 Jet function of $\gamma_{\text{inc}} - h$ , $\gamma_{\text{dec}} - h$ and $\gamma_{\text{dir}} - h$ pairs in 40 – 60% Au+Au with statistical method. The $x$ -axis is $\Delta\phi$ .	156
A.28 Jet function of $\gamma_{\text{inc}} - h$ , $\gamma_{\text{dec}} - h$ and $\gamma_{\text{dir}} - h$ pairs in 60 – 92% Au+Au with statistical method. The $x$ -axis is $\Delta\phi$ .	157
A.29 Jet function of $\gamma_{\text{inc}} - h$ , $\gamma_{\text{dec}} - h$ and $\gamma_{\text{dir}} - h$ pairs in 0 – 20% Au+Au with isolation cut method. The $x$ -axis is $\Delta\phi$ .	158
A.30 Jet function of $\gamma_{\text{inc}} - h$ , $\gamma_{\text{dec}} - h$ and $\gamma_{\text{dir}} - h$ pairs in 20 – 40% Au+Au with isolation cut method. The $x$ -axis is $\Delta\phi$ .	159
A.31 Jet function of $\gamma_{\text{inc}} - h$ , $\gamma_{\text{dec}} - h$ and $\gamma_{\text{dir}} - h$ pairs in 40 – 60% Au+Au with isolation cut method. The $x$ -axis is $\Delta\phi$ .	159
A.32 Jet function of $\gamma_{\text{inc}} - h$ , $\gamma_{\text{dec}} - h$ and $\gamma_{\text{dir}} - h$ pairs in 60 – 92% Au+Au with statistical method. The $x$ -axis is $\Delta\phi$ .	160

# 1 Introduction

Quarks and gluons are the building blocks of all visible matter in the universe, but yet, they do not exist as independent particles, except in a few extreme conditions. This is due to the property of confinement [1], which says that quarks can only be in a neutral color charge state. Individual quarks have color charge, therefore they will always look for, or sometimes create, companions to form neutral color composite particles. The composite particles that are formed by the quarks are collectively called hadrons, and the process of forming them is often called hadronization.

It is predicted that the confinement property is broken ("deconfined") if the quarks and gluons are packed together in an environment of very high density and very high temperature. Such conditions were believed to be present at the very early age of the universe, and the world then consisted of free quarks and gluons. The deconfinement of quarks and gluons is of special interest, because it helps us understand the nature of interaction between elementary color charged particles. The force between the color charges is called the strong force. The theory that governs their interaction is known as Quantum Chromodynamics (QCD). One of the open questions within this theory is the process of confinement itself. Studying a system of deconfined quarks and gluons might actually help provide some understanding.

Experimentally, the environment of very high temperature, high enough to free the quarks, is achievable by colliding heavy nuclei with ultra-relativistic energies.

On Earth at the moment, there are two places where such activity is conducted. One is at the Brookhaven National Lab, New York, through a collider called the Relativistic Heavy Ion Collider (RHIC), and second is at CERN, Switzerland, through a larger collider called the Large Hadron Collider (LHC). As of today, there are two experiment collaborations that are actively working at RHIC; PHENIX and STAR. This thesis analyzes data collected by the PHENIX collaboration. RHIC started running from the year 2000, and since then, PHENIX has collected collision data of multiple species and energy ranges; gold+gold, copper+copper, copper+gold, uranium+uranium, deuteron+gold, and proton+proton, at energy per nucleon of 39, 62, 200 and 500 GeV, and even more.

It is predicted that at the center of the heavy ion collision, the density and temperature are high enough that the nucleons melt and quarks are freed. Furthermore, the free quarks and gluons are thought to form a fluid-like medium with collective behaviors. The hot and dense medium was given the name the Quark Gluon Plasma (QGP) [3]. The goal of the RHIC experiments has been to verify the creation of QGP, and to further define its properties. It has been established quite firmly, through several indirect observations, that QGP was indeed created at the heavy ion collision [2]. The interest of this dissertation is to study the properties of the QGP, by using the 'hard scattering' interaction between the quarks and gluons in the middle of the QGP formation. In the following section, we would like to elaborate more on our study goal. But first, we will start with brief discussions on QCD and on the physics of heavy ion collisions.

## 1.1 Quarks and Gluons

Quarks are spin 1/2 particles that carry one out of three color charges. The charges were named red, green and blue. The antiquarks carry anti-colors. Gluons

are bosons that act as the strong force carrier, and they themselves carry a mixture of color and anti-color charge, with eight linearly independent combinations allowed. Interaction between color charges is described by the QCD lagrangian [4]:

$$\mathcal{L}_{QCD} = \sum_{a,q} \bar{\psi}_{q,a} (i\gamma^\mu \delta_\mu \delta_{ab} - 4\pi\alpha_s \gamma^\mu t_{ab}^C \mathcal{A}_\mu^C - m_q \delta_{ab}) \psi_{q,b} - \frac{1}{4} F_{\mu\nu}^A F^{A\mu\nu} \quad (1.1)$$

$a$  is the index for the color charge, and  $q$  is the index for the quark flavors. So far 6 flavors of quark are known, and they are summarized in Table 1.1.

Table 1.1: Quark flavors.

Flavor	Electric charge	Mass (GeV/c <sup>2</sup> )
Up (u)	2/3	0.003
Down (d)	-1/3	0.006
Charm (c)	2/3	1.3
Strange (s)	-1/3	0.1
Top (t)	2/3	175
Bottom (b)	-1/3	4.3

Any hadron can be formed through three possible schemes that produce a net zero color charge. First is by combination of a color and it's anticolor. This type of quark bound state involves two quarks and it is called as the meson. Second is by combination of three different colors or anticolors. This type of hadrons involves three quarks (or antiquarks) and is called the baryon (or antibaryon). The last scheme involves five quarks; a color-anticolor pair, and three different color quarks. This type of composite is called the pentaquark particle but so far there's no conclusive evidence of its existence.

The factor  $\alpha_s$  in Eq. 1.1 represents the strength of the interaction. Its value is on the order of 1, much larger than the coupling constant of three other forces (electromagnetic, weak and gravity), therefore the name the strong force. The value of  $\alpha_s$  actually evolves as function of distance or the energy scale of the interaction. The dependence of the coupling constant to the energy scale is measured in many experiments and is shown in Fig. 1.1. The energy of a process determines the inverse of the distance over which the process occurs, therefore the plot shows that interaction is weak at small distance, and increases as the distance grows. This peculiar property is called asymptotic freedom [6].

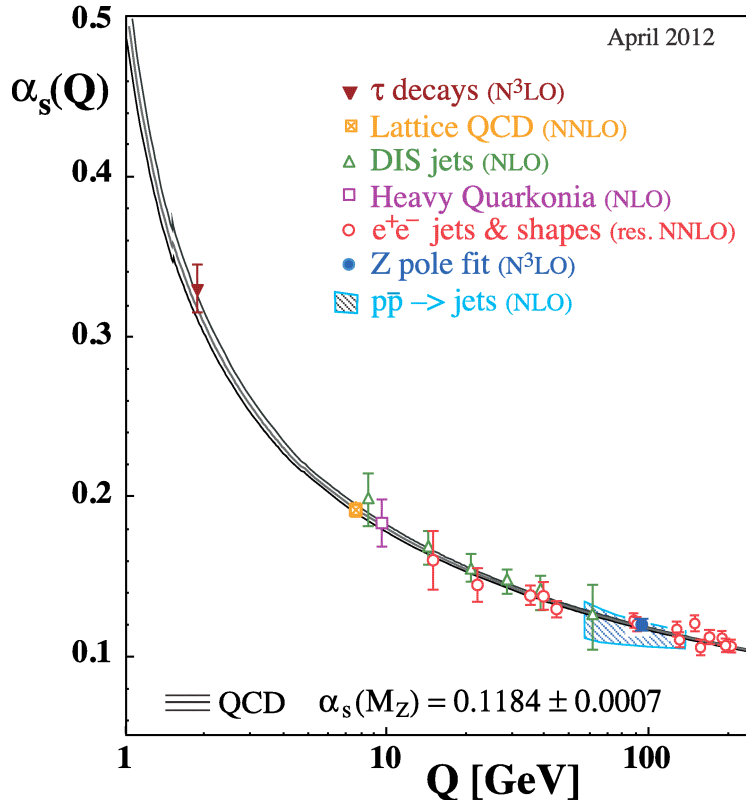


Figure 1.1: Measurement and theoretical calculation of  $\alpha_s$  as function of energy scale  $Q$  [4].

In an environment of high temperature, the quarks become more energetic. Based on the asymptotic freedom behavior, that would cause the interaction to be weaker. When the temperature is high enough, the coupling constant becomes very small such that the quarks are effectively free and not affected by their neighbors. The weakening of the coupling constant can also occur in the system of very high density. Because the charges are so densely packed, the potential between two charges at some distance can be screened. This is a more common phenomena and could also appear in a dense electrostatic system.

One can imagine that a phase diagram might exist to describe the different possible states of QCD matters. Unfortunately, unlike phase diagram of water for example, the QCD phase diagram is not precisely defined yet. A 'prototype' or prediction for QCD phase diagram can be seen in Fig. 1.2. According to theoretical calculations there is a line that separates the confined (hadronic matter) and the deconfined phase (QGP), that stops at a critical point, where beyond that the crossover phenomena would takeover. As is seen in the same figure, relativistic heavy ion collider try to reach the point of where the temperature is higher than the border of phase transition.

## 1.2 Relativistic Heavy Ion Collision

When accelerated to ultra-relativistic energy, the two nuclei are Lorentz contracted in the beam direction, therefore they arrive at the collision center in a pancake-like form, enhancing the particle density. As they collide, the partons (the quarks and gluons) inside the nucleons within the overlap region are freed. They then thermalize and form the hot and dense medium, noneother than the quark gluon plasma.

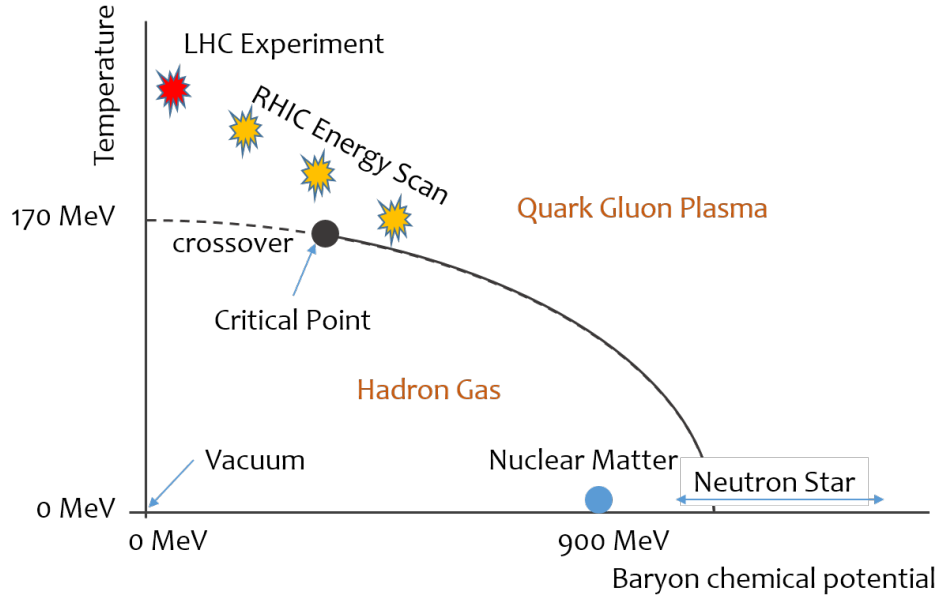


Figure 1.2: Qualitative prediction of phases of QCD matter. Adapted from [5]

Occasionally, or rather rarely, at the initial stage of the QGP formation, some partons undergo a hard scattering process. The hard scattered partons are knocked-out from the system with large transverse momenta, traversing the hot and dense medium, and therefore could serve as a probe to QGP.

At the later stage of the collision, the QGP expands and cools. The partons hadronize into hadrons, and the quark gluon plasma evolves into hadron gas. At the final state, hadrons (and photons) fly out and away from the collision center towards the detectors. Along the way, heavier hadrons might decay before they reach the detectors, therefore more particles are produced. As we will discuss later, the collection of the detected final particles shows a somewhat collective behavior, an evidence that they originated from a thermalized medium. A cartoon that depicts the evolution of the stages in a heavy ion collisions is shown in Fig. 1.3

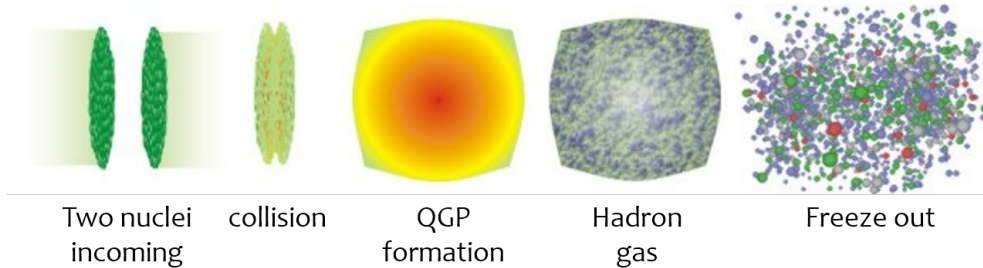


Figure 1.3: A cartoon of evolution of the stages in heavy ion collisions. Parts adapted from various publically available sources.

The hard scattered partons also evolve into hadrons, but they produce a more unique final product. Specifically, the initial parton would undergo fragmentation process, producing a stream of daughter partons, where each of them in turns hadronize or recombined to produce hadrons. Along the way some of the hadrons might also decays. This stream of particles carries a total energy that is equal to the energy of the initial parton, and collectively they are referred to using the term *jet*.

A jet would manifest in unique signature on the detectors, where several hadrons seem to be concentrated on a finite region of space, and spread around a common axis. Such jet signal is seen clearly in a p+p collision system, where there is no QGP created. On the other hand, in heavy ion collisions, jet signal will be submerged in high multiplicity of particles coming from the remnants of the dense medium (also called as the underlying event). The jets and also the collective behavior of the underlying event that we mention earlier are used as indication of the creation of QGP. This will be discussed in the next section, but before that we will first continue with discussion regarding the geometry of heavy ion collisions.

## Characterizing an event by the collision geometry

An event of heavy ion collision can be characterized by the geometry of the overlap region between the two nuclei. The area of the overlap region will determine number of participating nuclei ( $N_{part}$ ) and number of individual collisions ( $N_{coll}$ ), which in turns determine the size of the QGP, and the multiplicity of the underlying event. The orientation of the overlap region with respect to the laboratory frame of reference is also important because it will govern the angular distribution of the underlying event particles.

The area of the overlap region is represented by a quantity called as the *centrality*. It is defined in percentage (%), where 0% (most central) means a head-on collision and 100% (most peripheral) means no collision. In principle there are equal probabilities that a collision event happens at any centrality. There is probably a maximum limit of an allowed centrality, which depends on the setup of the collider. Nevertheless, most of the time the overlap region would form an almond-like shape, rather than a good circle, which happens only in the most central event (see Fig. 1.4 (a)).

The orientation of the almond shape in the laboratory frame of reference also varied depending on the relative position between the incoming nuclei. The orientation of the almond shape can be determined through the reaction plane, which is defined by the cross-section of the beam axis and the axis that connects the centers of the colliding nuclei (the impact parameter  $b$ ). The depiction of the reaction plane is shown in Fig. 1.4 (b).

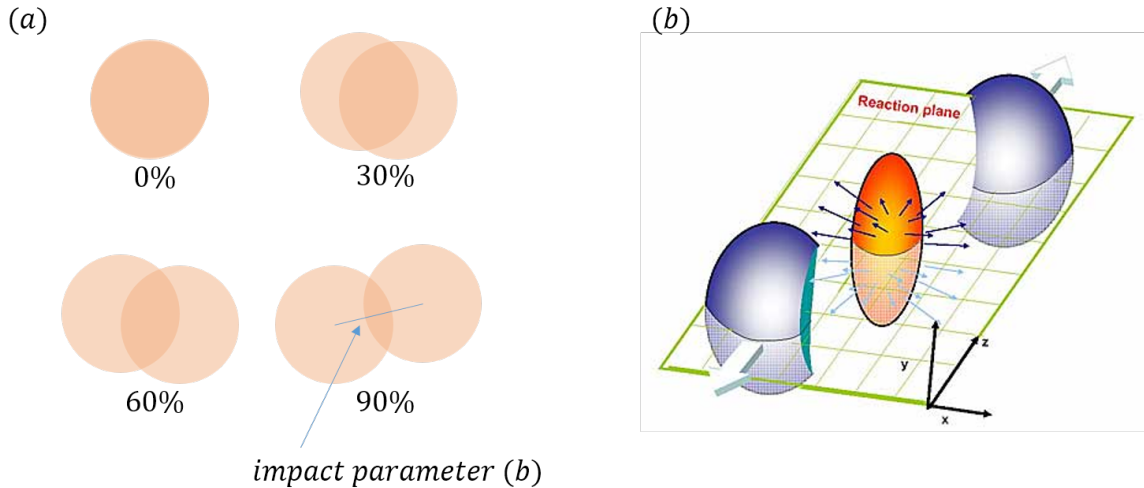


Figure 1.4: Diagrammatic depiction of the definition of centrality (a) and the reaction plane (b). Parts adapted from various publically available plots including [5]

### 1.3 QGP Signatures in Heavy Ion Collisions

#### 1.3.1 Harmonic flow

The anisotropic shape of the collision region would affect the distribution of the underlying event particles as they freeze out and spread over the detectors. In the direction perpendicular to the reaction plane, particle density is smaller, thus produces less pressure gradient, and therefore the outgoing particles have less energies, when compared to those in the direction parallel to the reaction plane.

As a consequence, the distribution of the bulk particles should exhibit an anisotropy, where more particles are observed in the direction parallel to and less in the direction perpendicular to the reaction plane. The anisotropy of the particle distribution is quantified in a harmonic expansion form:

$$\frac{dN}{d\phi} \propto 1 + 2v_2 \cos 2(\phi - \Phi_{RP}^2) + 2v_3 \cos 3(\phi - \Phi_{RP}^3) + \dots \quad (1.2)$$

The constants  $v_n$  are called the harmonic flow coefficients, where every  $n$ -th order represents contributions coming from  $n$ -pole moment of the geometric shape.  $v_2$  is the contribution from the dipole and it is called the elliptic flow.

The quantity  $v_2$  has been measured in RHIC experiment for several particle species [7]. In Fig. 1.5, the  $v_2$  values of different particles are plotted as function of the transverse momenta ( $p_T$ ) and kinetic energy ( $KE_T$ ). One can see that there are two major groups, where one is formed by mesons only and second is formed by baryons only, i.e, the group seems to separate different number of valence quark ( $n_q$ ).

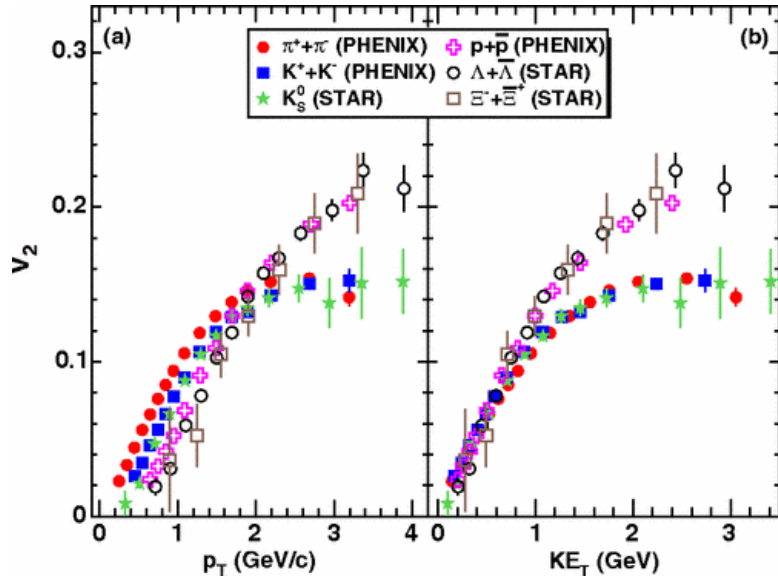


Figure 1.5:  $v_2$  measurements of different particles at RHIC [7].

When  $v_2$  is scaled by the number of the valence quarks (Fig. 1.6), the two groups are no longer separated, and all different species collapse into an universal trend. This shows that the degrees of freedom that actually flows are the quarks, not the hadrons. The fact that  $v_2$  of the particles is measured to be non-zero shows that the bulk particle does undergo thermalization at the early stage after the

collision, forming a collective medium, and, assumes the shape of the initial overlap region. The fact that the values of  $v_2$  are uniform when scaled according to number of valence quark, shows that the thermalized medium is made, to a large degree, out of independently-acting quarks.

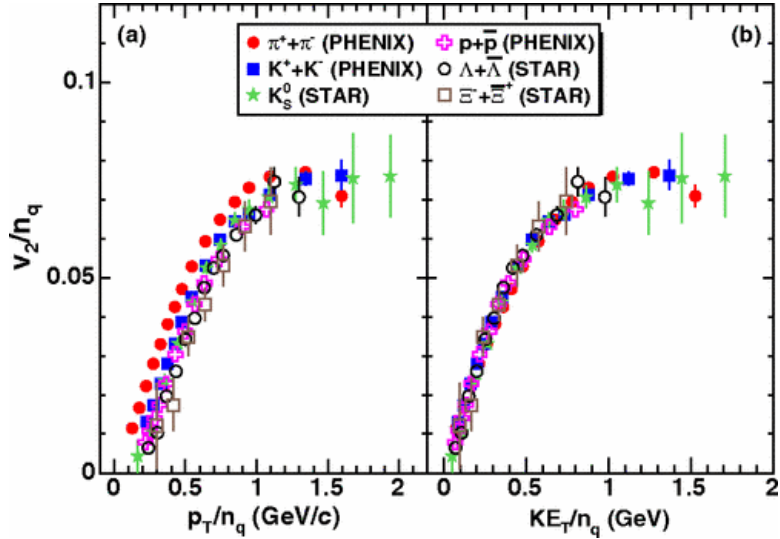


Figure 1.6:  $v_2$  measurements of different particles at RHIC scaled by number of valence quark [7].

### 1.3.2 Single particle suppression

A heavy ion collision system can be seen as a collection of multiple nucleon-nucleon ( $nn$ ) collisions, where the total number of single  $nn$  collisions depends on the sizes of the colliding nuclei. Based on that, one expects that the particle production in a heavy ion collision is the production in a p+p system scaled by the number of collisions in the heavy ion. It is then predicted that QGP that is created from the collision will modify the naive expectation.

Experimentally, the medium modification is tested by measuring the quantity  $R_{AA}$ , where if measured from Au+Au collisions is defined as

$$R_{AA} = \frac{1}{N_{coll}} \times \frac{d^2 N^{AA}/dp_T}{d^2 N^{pp}/dp_T} \quad (1.3)$$

The  $R_{AA}$  values measured in PHENIX from the most central Au+Au events with energy 200 GeV, of several species, are shown in Fig. 1.7. A suppression of a factor of 5 is found for the  $\pi^0$  and  $\eta$  mesons.

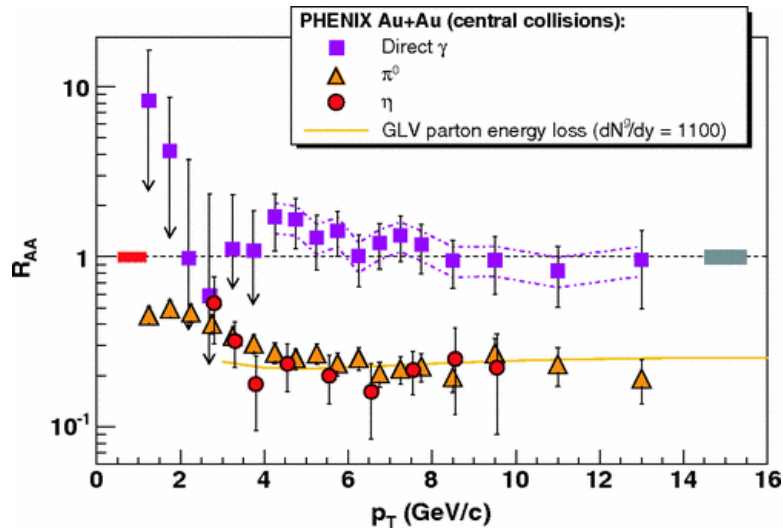


Figure 1.7: The  $R_{AA}$  measured in PHENIX for  $\pi^0$  and  $\eta$  [8, 9] and 'direct' photons [10]. Figure is grabbed from [11].

### 1.3.3 Jet suppression

A third signature of the QGP is obtained from jet measurements. The hard processes that produce the jets are the same in a heavy ion collision and a in p+p collision, except that the heavy ion jets would travel past the hot and dense QGP while the p+p jets do not. Then, any deviation of the heavy ion jets from p+p jets may be able to provide indications of QGP existence.

There are mainly two methods in measuring jets; the direct and the indirect way. The direct way is through the jet reconstruction algorithm. In this method, individual particles are collected, and by some predefined algorithm, are given the status whether it is part of a jet or not. Essentially, with this method we are attempting to reconstruct real jets with all of their constituents.

The indirect way is done by simply looking for correlations between two particles as function of their angular differences, or known as the two-particle correlations. In a back-to-back hard scattering process, jet particles would show maximum correlation at zero angular difference (near-side peak) and at  $\pi$  rad angular difference (away-side peak). The near-side peak represents correlations between particles of the same jet, and away-side peak represents correlations between particles of opposite jets.

The jet algorithm is quite effective when performed in p+p, but not in the heavy ion system. This is because the multitude number of underlying event particles increases the probability of picking up false jet constituents. For that reason, comparison of jets have historically mostly been done by taking the two-particle correlations measurement on both systems.

In Fig. 1.8 is shown the two-particle correlations between pairs of high- $p_T$  charged hadrons ( $h - h$ ), measured by STAR, in three different collision systems, p+p, d+Au and central Au+Au [12]. The near- and away-side peaks are apparent, except for the away-side peak of the central Au+Au, which seems to be consistent with zero, up to some degree of uncertainties. This indicates that in the Au+Au system the away-side jet loses its energy and does not make it out through the medium.

One should be careful that the types of jets that are sampled by the two-particle correlations are dependent on the selection of the  $p_T$  of the first particle

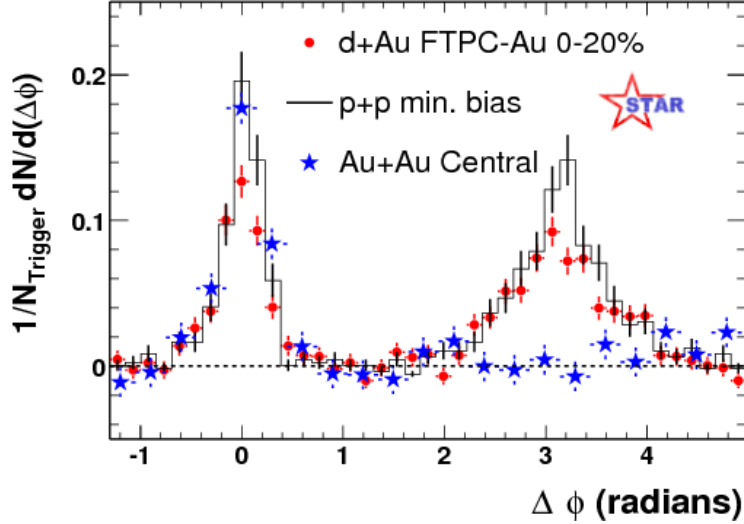


Figure 1.8: Dihadron azimuthal correlation with high  $p_T$  trigger in three different collision systems [12].

that make up the pair (the trigger particles). If the triggers consist of only high  $p_T$  hadrons, most likely we are collecting particles that do not or only very slightly suffer energy loss. That is possible if the trigger particles originate close to the surface of the medium. If that is the case, the opposite jet components (the associated particles) would have to travel the maximum length in the medium and thus experience the most severe energy loss, possibly losing all of their energy. This tendency, that selecting only the high  $p_T$  triggers will only pickup the particles near the surface, is called the surface bias.

Nevertheless, such results shown in Fig. 1.8 are sufficient in showing two things. One is that we are able to measure back-to-back jets, and second is that the away-side jets suffer energy loss as they travel the QGP created in the heavy ion collision.

## 1.4 Fragmentation Function Measurement Through $\gamma_{\text{dir}} - h$ Pair Correlations

Suppression of the jet particles in heavy ion collisions is an indication of energy loss of the hard scattered partons. Another avenue in studying the partonic energy loss is by examining the fragmentation functions. In the same fashion with observation of jet energy loss in Fig. 1.8, one can also compare the fragmentation functions measured in heavy ion collisions with those measured in p+p; the partonic energy loss would manifest in a modified fragmentation function.

Basically the fragmentation function can be regarded as the probability of a parton with momentum  $p^q$  to produce a hadron with momentum  $p^h$ . Usually the fragmentation is defined as function of the momentum fraction  $z = p^h \cdot p^q / (p^q)^2$ , and it is written as  $D_q^h(z, \mu)$ , where  $\mu$  describes the scale of the interaction. The fragmentation function can be derived from measurements of hadronic production cross-sections from any processes. For a hadron production in leptonic collisions, for example  $e^+ + e^- \rightarrow h + X$ , the cross-section can be written as

$$\frac{d\sigma^h}{dz} = \sum_i \int_z^1 \frac{dx}{x} C_i(x, \alpha_s \mu, Q, \mu) D_i^h(z/x, \mu) \quad (1.4)$$

The coefficient  $C_i$  is a function of the cross-sections of the partonic processes ( $\sigma^{q_i + q_j \rightarrow q_k + q_l}$ ).  $C_i$  in Eq. 1.4 can be calculated perturbatively and its value is dependent on the exact process of the  $h$  production.  $D_i$  on the other hand is universal and its value does not depend on the specific process. Eq. 1.4 does not apply in processes where the initial state contains color charge ( $e + p \rightarrow h + X$ , for example). In that case, an additional Parton Distribution Function (PDF) has to be added. PDFs describe the momentum distribution functions of the partons inside a hadron, and they represent the probability to find a parton carrying a fractional momentum  $x$ . Just like the fragmentation function, the PDF is also universal.

Fragmentation functions from  $e^+e^-$  from several experiments and in several beam energies are shown in Fig. 1.9. A property of the fragmentation function, albeit only approximate, is the  $z$  scaling. The approximate  $z$  scaling is seen in Fig. 1.9 (b) (note in the plot the variable  $z$  notated as  $x$ —in modern usage,  $z$  is always used), where the fragmentation seems to be independent of the collision energy. In terms of the collisional energy, the scaling starts to break down at low energy region, while in terms of the  $x$  ( $\equiv z$ ) values, it seems the scaling is best observed at mid to high  $x$  values.

In relation to jet measurements, it is assumed that the fragmentation function can be measured from the momentum fraction distribution of its constituents. The momentum fraction is now defined as  $z \cong x_E = p^i \cdot p^{jet} / (p^{jet})^2$ , (a hold-over to the older  $x$  notation in Figure 1.9) where  $p^i$  is the momentum of the constituent  $i$ , and  $p^{jet}$  is the total momentum of the jet, which is equal to the momentum of the origin parton.

In measuring jet fragmentation function in a heavy ion collision, the  $h - h$  pair correlations is not a good observable. The first problem is that there is no straightforward way in getting the jet total momentum; it has to be approximated through jet reconstruction algorithm. The second problem is the surface bias that could cause the loss of many of the jet pairs. And as the last problem, even if we could obtain the jet energy and avoid the surface bias, we still do not have the true energies of both jets since they are altered by the medium.

A more preferable observable is the correlations between direct photon and hadron ( $\gamma_{\text{dir}} - h$ ) pairs. Direct photons are photons that are produced in hard scattering processes. Leading order direct photons are produced either by an annihilation process ( $q\bar{q} \rightarrow g\gamma$ ) or, the more dominant one (since anti-quarks are

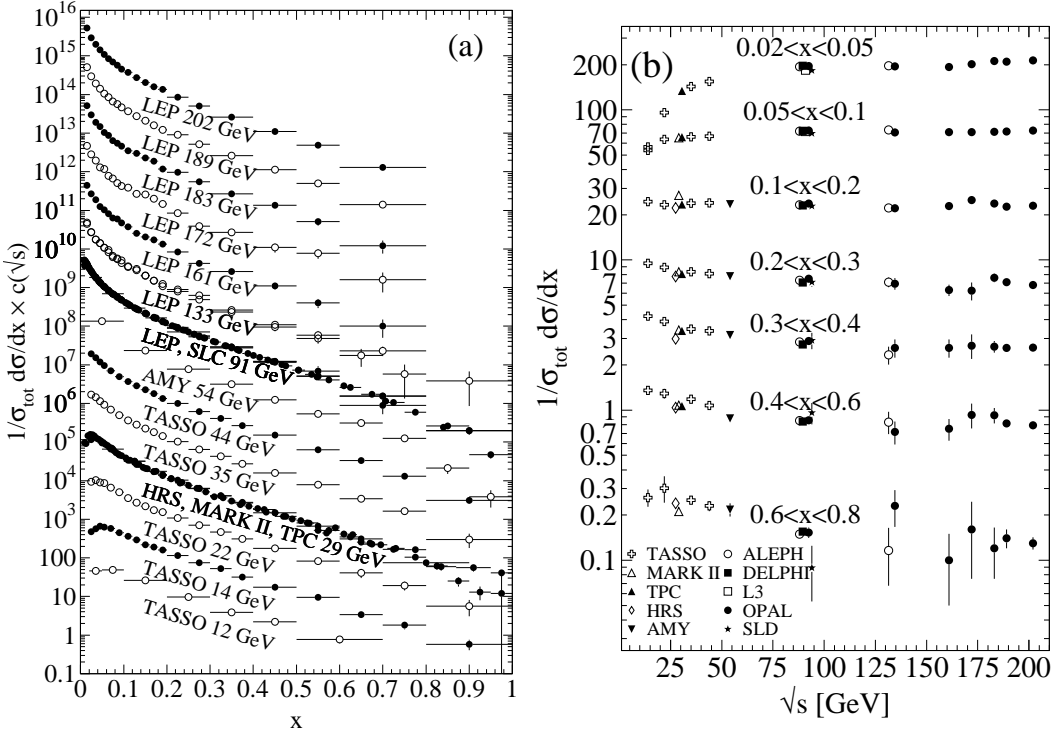


Figure 1.9: The  $e + e-$  fragmentation function for all charged particles is shown (a) for different CM energies  $\sqrt{s}$  versus  $x$  ( $\equiv z$ ) and (b) for various ranges of  $x$  versus  $\sqrt{s}$ . For the purpose of plotting (a), the distributions were scaled by  $c(\sqrt{s}) = 10^i$  with  $i$  ranging from  $i = 0$  ( $\sqrt{S} = 12$  GeV) to  $i = 13$  ( $\sqrt{s} = 202$  GeV). Most of these results are published more than 15 years ago. In modern common usage, the variable  $z$  is always used for what is notated as  $x$  in this plot. The compilation is obtained from the Particle Data Book Review [4].

much less present in colliding nucleons for A+A) the analog of Compton scattering ( $qg \rightarrow q\gamma$ ), see Fig. 1.10.

Direct photons do not get modified by the medium since they do not carry color charge (as shown in Fig. 1.7). Because of this, most of the problems mentioned in the  $h - h$  pairs measurement no longer exist. The momenta of the photon and the

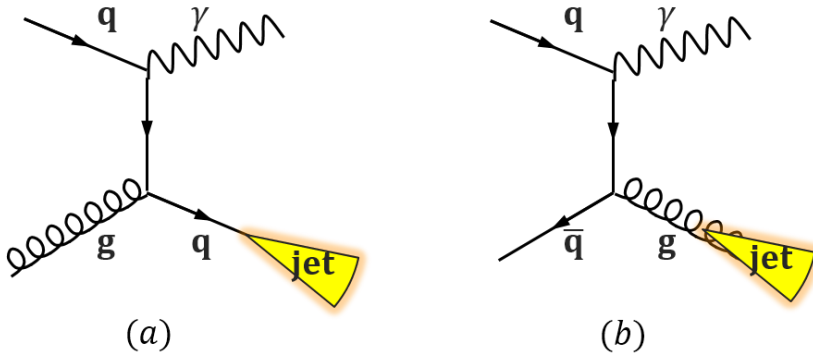


Figure 1.10: Production of hard direct photons through the processes of Compton scattering (a) and quark-antiquark annihilation (b).

parton balance each other to leading order, therefore the photon's momentum can be used to replace the unknown total momentum of the jet. It is also the exact true jet momentum, without any loss. Photons also do not suffer from surface bias, because high energy photon triggers don't necessarily only originate near the surface of the medium. The modification of the fragmentation function in the medium is quantified as the ratio of the per-trigger yield of direct photon - hadron correlation in the heavy ion system (such as Au+Au), with that in p+p:

$$I_{AA} = \frac{Y^{Au+Au}}{Y^{p+p}} \quad (1.5)$$

In the measurements of  $\gamma_{\text{dir}} - h$  pair correlations, there is a complication that different types of photons exist, and direct photons are among the rare ones, therefore their identification is not trivial. Mainly, we can categorize all photons as decay and non-decay products. The decay photons can come from underlying event hadrons and also jet constituent hadrons. Out of all the detected photons, most of them are decay products, and out of all the decay photons, most of them come from neutral pions. The non-decay photons might come from a hard scattering process,

or from a thermal radiation (bremsstrahlung, for example). Furthermore, the hard-scattered photons might come from the two LO processes that we mentioned earlier (annihilation and Compton scattering), which we call as the 'direct photons', or from higher order processes, which we call as the 'fragmentation photons'.

The most readily identifiable photons are those that come from pion decays; by measuring the invariant mass of the photon pairs. As a general method in measuring direct photons, usually one will start with finding decay photons, then subtracting them from the overall (inclusive) photons. The subtraction is usually done after collecting all photon sample from the available events, therefore it is called the statistical subtraction method.

Direct photons also have a feature that decay photons do not; they are generally isolated. Since a decay photon is usually a member of a jet or part of the underlying event, it would have several particles accompanying on its surroundings. In case of the direct photon, since it is produced in the initial hard scattering and does not form a jet, it will not have many particles on its surroundings. This feature is used as a selection rule in sampling the photons, and it is called the isolation cut method. One would fix a cone region around a photon and measure the total energy of particles within the cone. Photons with cone energy larger than a certain threshold are tagged as non-isolated, and assumed to be decay photons, and are removed from the sample. This technique results in a cleaner sample that eventually reduce the uncertainties, and it is called the isolation cut method.

## 1.5 Mechanism of Energy Loss

A parton that travels through the QGP loses its energy via two main mechanism; through elastic scattering with the constituent of the medium (collisional) and through inelastic scattering where gluon bremsstrahlung are

emitted (radiational), with the radiational energy loss being the dominant. There are several models of radiational energy loss that gives prediction of the gluon spectra, usually as function of the density of the medium. The amount of the energy loss can then be related to the amount of hadron suppression, and in turn give information about the density of the medium. A general review of various energy loss models can be found in [13].

There are two schemes that are used by models in evaluating the hadron suppression; energy loss of the leading hadron and modification of parton shower. In the first scheme, an approximation is made that most of the energy and momentum in the event is carried by a parton, and one would evaluate the total energy loss of such leading parton. In the second picture, one follows the branching of the a parton into subleading partons and examines the evolution equation in the medium.

Both approximations can describe single particle suppression (the  $R_{AA}$ , see Eq. 1.3) quite well, but they start to differ when describing jet-related measurement (the  $I_{AA}$ , see Eq. 1.5). With the leading parton scheme, the model does not describe exactly what happens to the radiated gluons, albeit clearly they should hadronize and become sources of soft hadrons. Some models consider that the loss energy is 'absorbed' by the medium as a shock wave. This generated a difference between the two picture of energy loss, especially in the distribution of low  $p_T$  jet components. Particularly, in the shower picture the energy loss is predicted to be redistributed as the enhancement of low  $p_T$  partons.

A calculation on  $\gamma_{\text{dir}} - h$  calculation is used to separate the two approximations [14]. To test the leading hadron approximation, the ASW model [15] is implemented, while the modified parton shower is represented by the YaJEM model [14], the differences of the results are shown in Fig. 1.11. PHENIX has published a result that gives indication to enhancement of  $I_{AA}$  at low  $x$ , with agreement to the

energy loss redistribution picture. This particular published PHENIX result will be discussed as part of Chapter 6. More specifically, it was the measurement in Au+Au 200 GeV, in events of 0 – 40% in centralities.

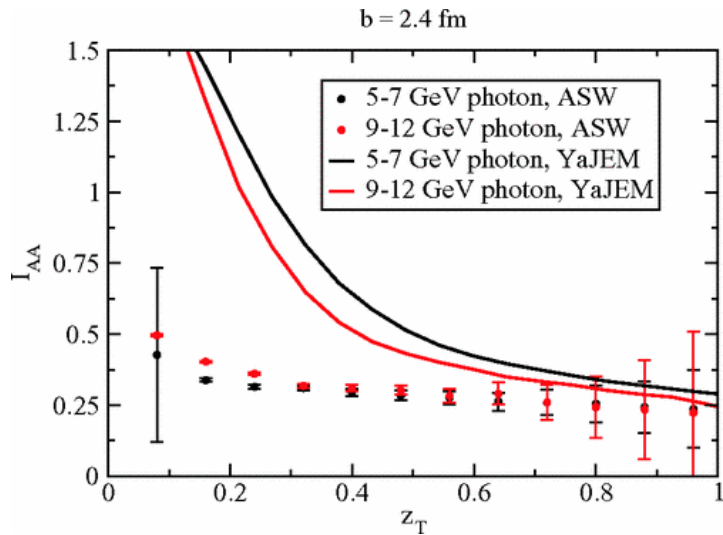


Figure 1.11: Calculation of the ratio ( $I_{AA}$ ) of  $\gamma_{\text{dir}} - h$  yields in 200 GeV Au+Au and in p+p, from the ASW and YaJEM model. Here  $z_T = p_{T,h}/p_{T\gamma}$ , is an approximate to the scaling variable  $x$ . In YaJEM, the branching of the leading parton is tracked down, resulting in the prediction of the enhancement at low  $z_T$ , in contrast to an overall suppression predicted from ASW result [14].

## 1.6 Purpose of the Dissertation

In this dissertation, we would like to expand PHENIX measurements of the Au+Au fragmentation function from the mid-central to include the peripheral events as well as look in more detail at the centrality dependence overall. From the knowledge of the fragmentation function from all centralities, we hope to be able to

understand the dependence of the modification of the fragmentation function on the medium size and density.

To be able to obtain the peripheral  $\gamma_{\text{dir}} - h$  correlations, an additional isolation cut is applied to gain a high signal-to-background ratio of photons. To make sure that the isolation cut in Au+Au is effective, a pre-study is conducted to determine the best isolation cut parameters. To summarize, in this project we would like to perform the measurement of the fragmentation functions in Au+Au events of all centralities, through the  $\gamma_{\text{dir}} - h$  pair correlations, and applying the isolation cut.

The remainder of this document will be arranged as follows. Chapter 2 will describe the PHENIX detector system used in collecting the photons and charged hadrons. Chapter 3 will discuss the analysis procedures. Chapter 4 is dedicated to elaborate more on the isolation cut, also on data selection prior to the analysis. For all the methods in the measurement, we have also performed Monte Carlo simulations to test them. This study is discussed in Chapter 5. The remaining chapters 6, 7 and 8 contain discussions on results, sources of systematic uncertainties, and conclusions.

## 2 Experiment Details

### 2.1 RHIC Accelerator

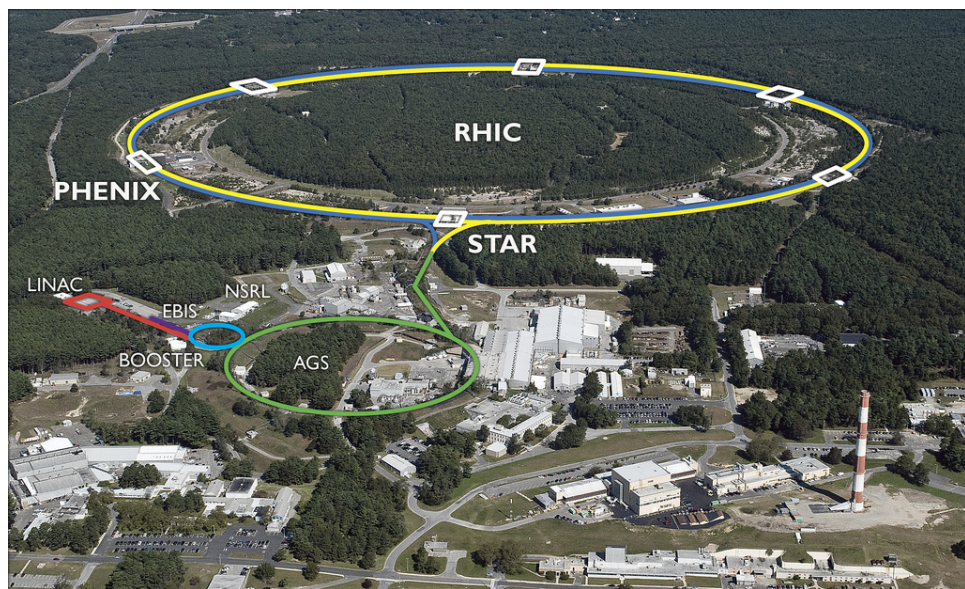


Figure 2.1: Aerial view of the RHIC accelerator complex. This marked photograph is taken from publicly available sources.

The Relativistic Heavy Ion Collider (RHIC) [19] complex is located at the Brookhaven National Laboratory (BNL) in Upton, New York, USA. The collider was constructed in the beginning of 1991 and was completed around 2000, which was also the year when it started its first operation. RHIC is capable to accelerate heavy ions up to the energy of 200 GeV and protons up to 500 GeV. Additional capability of RHIC is that it can accelerate polarized protons, which is essential for proton spin study. Two independent beam lines (blue and yellow) that are available

at the accelerator make it possible to collide heavy ions of different species. Up to today (2014), RHIC has conducted several collision systems both symmetric and asymmetric that includes Au+Au, p+p, d+Au, Cu+Cu, U+U and Cu+Au.

The particles are transported from the source through the Tandem Van-de-Graaf to the booster and the Alternating Gradient Synchroton (AGS) where the ions are accelerated to a speed of 99.7% of the speed of light, after which the particles enter the RHIC ring (see Fig. 2.1). Currently, there are two experiment collaborations that are still collecting data of the collisions; STAR and PHENIX. Both have started taking data since the beginning of RHIC operation in 2000, at that time with two, now halted, experiments BRAHMS and PHOBOS. The data used in this thesis work are collected by the PHENIX (Pioneering High Energy Nuclear Interaction eXperiment) detector system.

## 2.2 PHENIX Detector

PHENIX [20] comprises a collection of detector subsystem, each of which could have different or overlapping function and are optimized to perform their specific task in the crowded environment produced by the heavy ion collision. In describing the list of PHENIX subsystems, we will categorize them into three main groups; the event characterization (or the global) detectors, the central arm spectrometer, and the muon arm detectors. The central detectors consist of two arms oriented radially from the beam axis (the East and West arms). Most but not all subsystem have a symmetric configuration on both arms. The global and muon detectors are oriented in parallel with the beam axis and almost all subsystems have symmetric pair on both (North and South) arm. The PHENIX setup during 2010 is shown in Fig. 2.2.

The function of the event characterization detectors is to determine the global properties of a collision event. They include the impact parameter (quantified as the

centrality), vertex position, and orientation of the reaction plane. Those global information are not only necessary for any analysis of the saved events, but are also used to veto events that will not be important for physics purpose. Such event selection based on online global property measurement is called Level 1 triggering.

The main functions of the central arm spectrometer are to detect photons and charged particles. The muon arms are initially specialized for muon measurement, but later also have the capability as a spectrometer for particles on large rapidity region. In the following sections, we will only describe the detectors that are essentials for the analysis conducted in this thesis.

### 2.2.1 Event Characterization

#### Beam Beam Counter

BBC [23] measures the total charge and the timing of particles coming in the forward direction. Two sets of BBC (North and South) are positioned surrounding the beam pipe at a distance of about 1.5 m from the center of PHENIX system. They have the rapidity coverage of  $3.1 < |\eta| < 3.9$  and a full ( $2\pi$ ) azimuthal coverage. Each arm consists of 64 elements of quartz Cherenkov radiator and Photomultiplier tubes (PMTs) that collect the Cherenkov lights and transform them into electronic signals. The measurement of number of particles and their timing on both forward arms is utilized to determine three things; the vertex location, the centrality, and the *time zero* of the collision, which is used as reference in determining time flight of a particle.

The collision vertex along the beam pipe (the  $z$ -vertex) is measured from the difference of the average timing of leading charged particles that are captured in the North and South BBC, as

$$z = \frac{(T_S - T_N) c}{2} \quad (2.1)$$

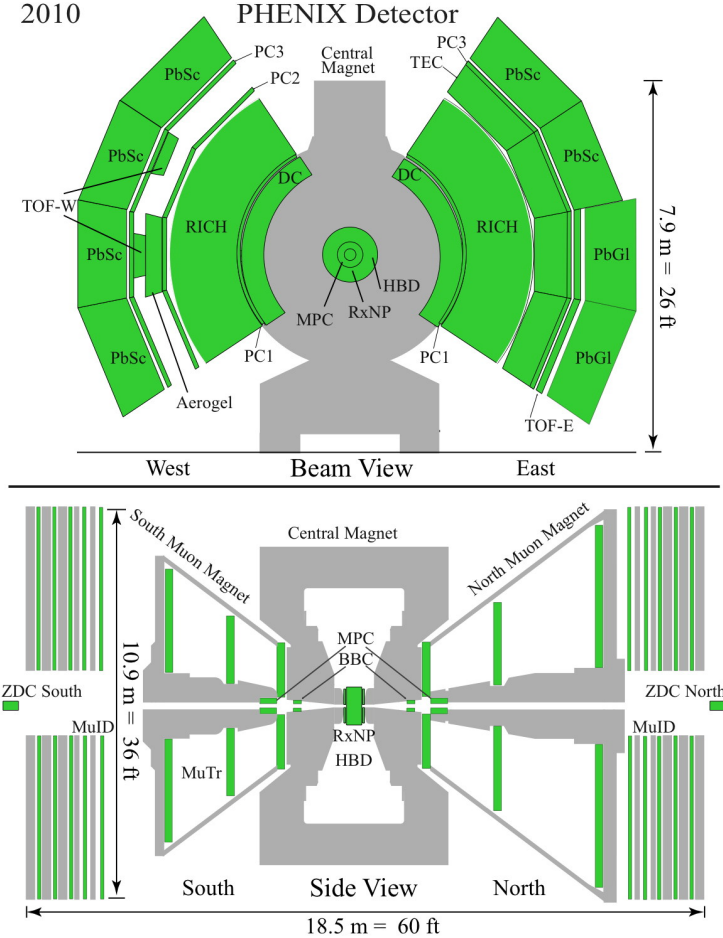


Figure 2.2: Schematic view of the PHENIX detector as seen in the beam direction (top); showing the central arm configuration. And in the side view (bottom); showing the event characterization and the muon arm configurations. [21]

$T_{(S,N)}$  is the average timing of particles in (South,North) BBC and  $c$  is light velocity. The accuracy in  $z$ -vertex determination varies according to conditions of the collision. The accuracy gets worse for the small impact parameter (peripheral collision), small beam size, and low energy. The accuracy in the central collision of 200 GeV beam is about 1 cm. Value of the  $z$ -vertex is used as a Level-1 trigger, that

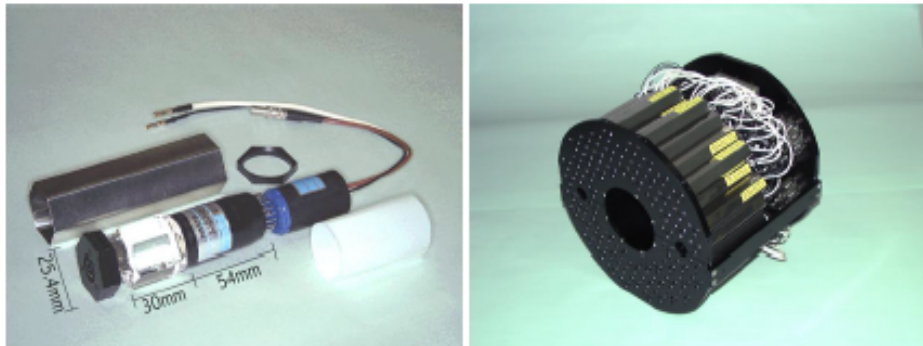


Figure 2.3: A single BBC element consisting of quartz Cherenkov radiator and PMT (left) and a BBC arm with 64 elements (right). [21]

requires that an event is kept only if the  $z$ - vertex is within the range of -30 to 30 cm. Such requirement is applied to optimize the function of central arm detectors; farther  $z$ -vertex position will produce less signals for the central arm detectors.

The time zero is measured according to:

$$t_0 = \frac{T_S + T_N - 2L/c}{2} \quad (2.2)$$

where  $L$  is the distance from the center to the BBC ( $= 144.33$  cm). This time zero is used as a reference for other detectors, especially by the Time-Of-Flight (TOF) detector, which will not be discussed in this thesis.

The centrality of the collision can be inferred from the number of total charge deposited in the BBC arms. In peripheral collisions, most proton charge keep going straight in the beam pipe because they do not undergo any interaction. This results that in peripheral events only small number of charged particles are detected in the BBC, and as it goes to more central collisions more charged particles will be registered. Such feature is usually sufficient to determine the centrality of a collision, but one can also include the information from the spectator neutrons and use the correlation between the neutrons and the BBC's protons. The spectator

neutrons are detected in another detector called the ZDC, therefore we will discuss the determination of centrality afterwards.

By looking at the flight direction of the charges collected in BBC and the vertex position, one can also determine the orientation of the reaction plane. In this analysis, the reaction plane angle is determined using a newer detector with better resolution called the Reaction Plane (RXNP) detector. We will discuss the measurement of the reaction plane using RXNP but the BBC method is similar.

### **Zero Degree Calorimeter (ZDC)**

The ZDCs [23] main function is to measure neutrons that do not participate in the collision, e.g. the spectator neutrons. ZDC is a hadronic calorimeter made of tungsten interfilled with fiber optics and connected to PMTs. Two ZDCs are positioned at the distance of 18 m from the PHENIX center point, between the two beam pipes, such that it is aligned with the beam direction when both pipes are intersecting (Fig.2.4). Such configuration gives the detection coverage at zero degree, corresponds to  $|\eta| > 6.0$ . In front of each ZDC, dipole magnets are installed and they deflect protons, leaving only the neutrons to deposit energy in the calorimeter. Each ZDC has the longitudinal dimension of 50 times it's radiation length ( $X_0$ ) to make sure all neutrons energy are contained.

The readout of the energy deposited by the neutrons in ZDC serves for two purposes. One is as a control of the beam luminosity, and second is to determine the collision centrality together with BBC measurement. Correlation between the total charges measured by the BBC and the total energy deposited in the ZDC is shown in Fig. 2.5. In central collision, there are only small number of spectator protons and neutrons, this produces large BBC charges and low ZDC energy. In peripheral collision, there are large number of spectator protons and neutrons.

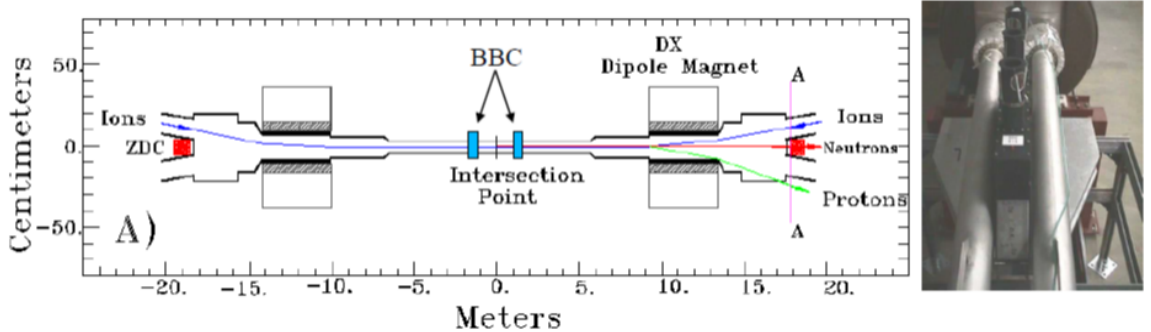


Figure 2.4: Position of ZDCs, BBCs, DX magnets, and the two beam pipes. [21]

Those spectators nuclei are still strongly bounded, and that causes the neutrons to follow the protons as they are deflected by the magnets in front of the ZDCs. This produces small detection both of the BBC charge and ZDC energy.

Centrality classes are determined by dividing the distribution of BBC charge and ZDC energy with equal number of events in each division. Based on the non-linear correlation described in the previous paragraph, one would group ZDC vs BBC distribution with a clock method; that is to take some pivot point and perform the division radially based on the pivot point. A more traditional method is when one only uses the BBC charge distribution, omitting the ZDC energy of the event. In that case the division is performed linearly with respect to the BBC axis (Fig. 2.5).

Determination of the centrality is used in the Minimum Bias trigger of the Au+Au collisions. Based on HIJING [22] calculation, the efficiency of Au+Au collision at 200 GeV is  $92 \pm 2\%$ , and it goes lower as collision energy decreased. This introduces the Minimum Bias (MB) triggering where only events with centrality of  $0 - 92\%$  are collected in the Au+Au collisions of 200 GeV energy.

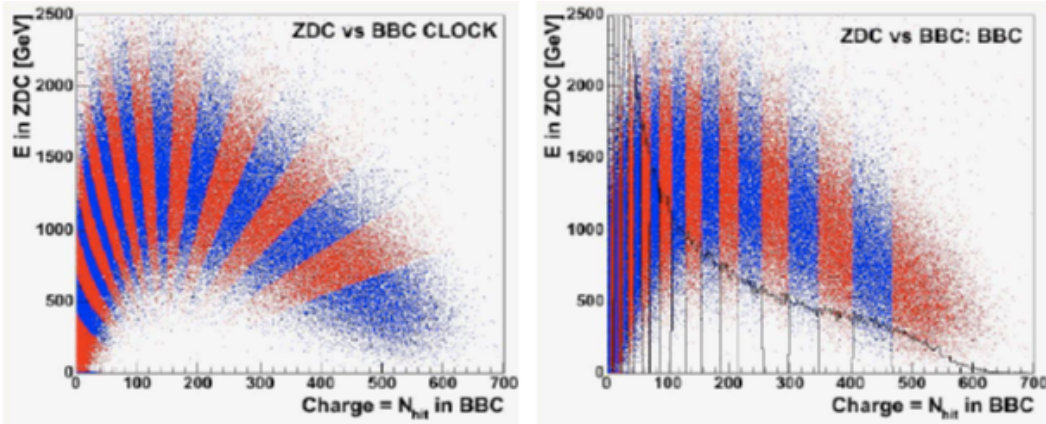


Figure 2.5: Two methods of determining centrality classes; The clock division (left) and the BBC only division (right). [21]

### Reaction Plane Detector

The reaction plane detector (RXPN) [24] is a type of hodoscope; it measures energy of photons and charged particles that pass through the detector. RXPN consists of plastic scintillator behind lead layers, surrounding the beam axis both at the north and south side, and are connected to fiber optics and PMTs that transfer the signals to the electronics. RXNP are located close to the center of the detector system ( $38 < |z| < 40\text{cm}$ ). It has the detection coverage of  $2\pi$  in azimuth, and a forward  $1.0 < |\eta| < 2.8$  in rapidity. On each arm the RXNP consists of 12 segments in  $\phi$  and 2 segments in  $\eta$  of scintillators.

As discussed in Chapter 1, we noted that incomplete overlap between nucleus results in almond shaped collision region. The reaction plane is defined by the vector between centers of the two nuclei and the beam direction. Pressure gradient is larger in the in-plane direction compared to the out-plane direction. In RXPN, this results in large energy deposition in the segments that are aligned with the

reaction plane, and less in the segments aligned with the out-plane direction. This feature allows the RXPN to measure the reaction plane in an event-by-event basis.

The reaction plane angle ( $\Phi_R$ ) is determined with respect to a fixed angle in PHENIX coordinate system. An alternative to that is a quantity called the *event plane angle*. The event plane is determined based on each harmonic of the Fourier expansion of particle azimuthal distribution. It is given the symbol  $\Phi_n$  where  $n$  is the order of the harmonic expansion. The event plane is defined as

$$\Phi_n = \frac{1}{n} \tan^{-1} \left( \frac{Y_n}{X_n} \right) \quad (2.3)$$

with

$$Y_n = \sum_i \sin(n\phi_i), \quad X_n = \sum_i \cos(n\phi_i). \quad (2.4)$$

Before installation of the RXPN, the event plane was determined using the distribution of particles recorded at the BBC. The RXPN was commissioned and used to determine the event plane starting from 2007. It is shown that to the second harmonic order, RXPN provided twice the resolution compared to the BBC. However, it is found that the large segmentation of RXPN may cause unreliable measurement for higher harmonics of the event plane, which is realized to be important [25]. The RXPN was decommissioned after 2010 to make room for new detectors. In this analysis, the Au+Au data are taken in the year 2007 and 2010 and therefore the RXPN is still playing a role.

### 2.2.2 Central Arm Spectrometer

The PHENIX central arm spectrometer detects the particles that are produced in the mid-rapidity region. The east and west arms of the spectrometer have the coverage of  $|\eta| < 0.35$  in rapidity, each with  $90^0$  in azimuth. A different opening angle at the top ( $67.5^0$ ) and at the bottom ( $112.5^0$ ) allows for a full  $2\pi$  acceptance in the measurement of azimuthal difference of particle pairs, which is of important

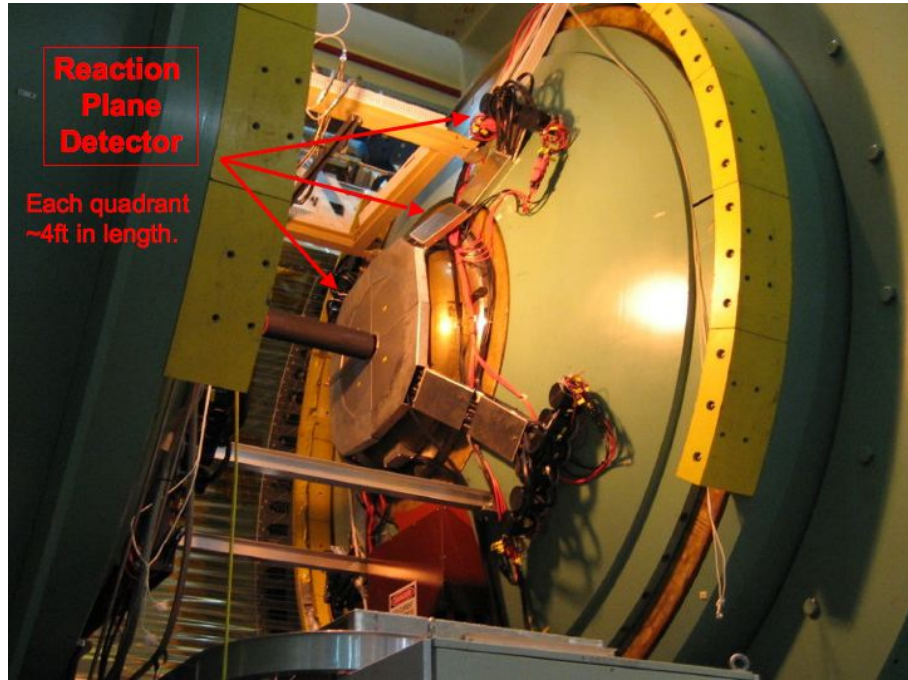


Figure 2.6: One arm of the RXPN detector [21].

interest in this thesis. The spectrometer is expected to identify a wide range of particles (photons, electrons, hadrons) and to resolve their position and energy in an environment of high occupancy.

In the coming section, we will discuss the subsystems that are closely related to the measurement of photon-hadron correlations. The photons are detected at the outer end of the spectrometer, by the Electromagnetic Calorimeter (EMCal). The charged hadrons are detected by tracking detectors that include the Drift Chambers (DC) and the Pad Chambers (PC). The electrons need to be identified to remove their contamination to the hadron signals, and it is done by the Ring Imaging Cherenkov (RICH) detector. Hadrons can be identified measuring their masses based on the flight time. The flight time is measured in the Time-Of-Flight (TOF)

detector using time zero determined by the BBC. Since we are working with the unidentified hadrons we will not discuss the time of flight.

## Drift Chamber

The PHENIX drift chamber (DC) [26] detects particles and reconstructs their path as they pass through the detector. A DC module consists of anode and cathode wires inside a cavity filled with gas of 50% Argon and 50% Ethane, with electric field applied between the wires. A passing charged particle will ionize the gas and produce some amount of electrons that then drifted to the anode wire, and ions that drifted to the cathode wire. The drift motion of the electrons and ions generated the signals that are later captured by the electronics. The anode wire is accompanied by three types of focusing wire: the Gate, Pot., and Back wires. These wires focuses the drift electrons to the anode and identify the position of the passing particles with respect to the anode wire.

Each module is placed across the north-south direction with 6 different types of alignment. The X1 and X2 modules are parallel to the beam axis and they locate the  $\phi$  coordinate. The U1, V1, U2 and V2 are shifted at about  $6^0$  from the parallel and they measure the  $z$  coordinate. Those 6 modules form a keystone, and 80 keystones form each of the DC arms. A total of 12800 wires are installed on the detector. Each arm has the length of 2.5 m and thickness of 450 mm, and they are located 2 m away from the beam pipe.

Charged particle paths are bended by the central magnet prior to entering the DC. The strength of the magnetic field and the tracks reconstructed in the DC are used to determine the charge and momentum of the passing particle. A charge track is defined by multiple hits of the X and UV wires. The PHENIX DC has single wire hit efficiency of 95% and the position resolution of  $165 \mu\text{m}$ .

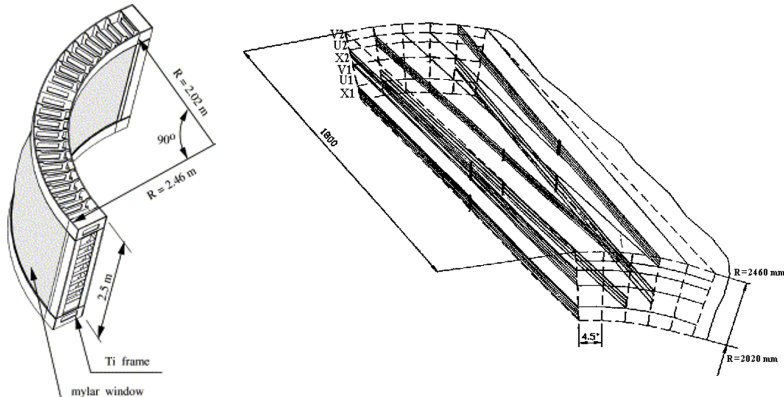


Figure 2.7: The schematic layout of a DC arm (left) and a DC keynote configuration (right). [26]

## Pad Chamber

The PC [26, 27] is another charge particle detector in the central arm, it's main task is to follow the charge track throughout the spectrometer; from the DC exit up to EMCAL entrance. For that purpose, 3 detectors (PC1, PC2 and PC3) are installed on the westarm, and 2 (PC1 and PC3) on the east. The PC deploys different principle and design in detecting a charge compared to DC. Each PC consists of a single anode wire planes sandwiched by two copper plane that acts as the cathodes.

The cathode plane is actually composed of three layers of copper plates and each are segmented by small pads. A cell is an area where three pads are intersecting. The plates are arranged such that *honeycomb* structure is achieved on the pad layers (see Fig. 2.8). A charge hit is defined by signals coming from three pads that form a cell. Readouts are placed on each pad, the honeycomb structure results in a factor of 3 less channels compared to if the readouts are placed on every cell, although they are equivalent.

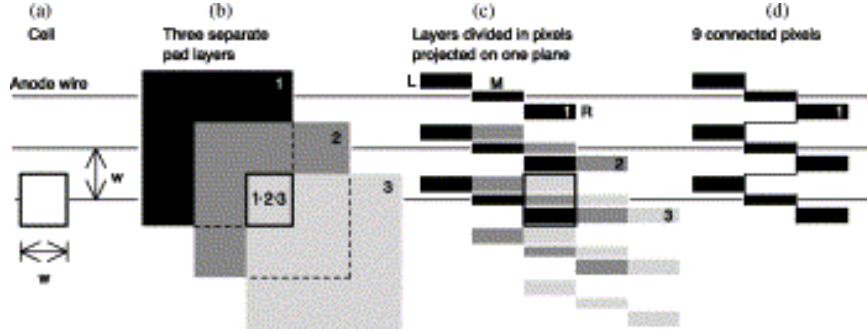


Figure 2.8: Principle of the pad geometry [27].

Each PC is located at the distance from the beam pipe of 2.5 m, 4.2 m and 5.0 m for PC1, PC2 and PC3 respectively. In the PC1, each pad has the dimension of  $0.84 \times 0.84$  mm. PC3 has pad size 4 times larger. Since it is located farther, a larger pad size could reach the same occupancy efficiency as in the PC1. The PCs have a position resolution of 1.7 mm and a hit efficiency of 99%.

Momentum of a track is determined using the combined information from DC and PC1, as well as the vertex position determined by the BBC. Such momentum determination results in a resolution as a function of the track's momentum:

$$\frac{\delta p}{p} \approx 0.7\% \oplus 0.1\% p \quad (2.5)$$

A high  $p_T$  track tends to travel in a more straight line, causing a large uncertainty in the azimuth position, this then is translated as a lower resolution.

## RICH

The RICH (Ring Imaging Cherenkov) detectors [28] identify electron through the creation of Cherenkov radiation. Cherenkov radiation happens when the speed of a particle is faster than the speed of light in a medium. Two RICH detectors are available in both arm of the spectrometer, each arm is filled with CO<sub>2</sub> gas of 40 meter cubic volume. On average, an electron that travels the distance of 1.2 m in

the gas with  $\beta = 1$  will produce 12 Cherenkov photons in a ring with radius of 5.9 cm. Spherical mirrors are used to reflect the photon rings to an array of PMT's that will further send the signals to the electronic read out.

In this analysis, the use of RICH measurement is to veto electron tracks from the hadronic ones. The minimum energy threshold where electron will start producing the Cherenkov light is 20 MeV, while in the case of pions it is 4.7 GeV. Therefore, electron veto using RICH signal is only good in the low energy region. Likewise, identification of electron is also reliable only in the range of 20 MeV - 5 GeV.

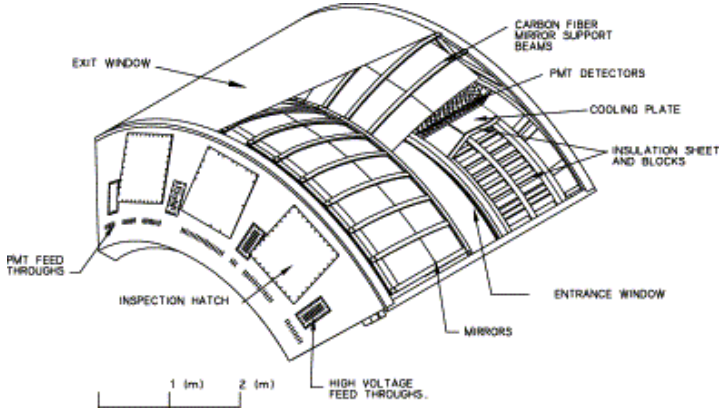


Figure 2.9: A schematic view of one arm of the RICH detector [28].

## EMCal

The EMCal [29] measures the energy and position of photons and electrons, through the mechanism of electromagnetic showering in the detector material. The EMCal is composed of individual towers made of lead-scintillator (PbSc) and lead-glass (PbGl). A PbSc is made of alternating layers of lead absorber and plastic scintillator. Each PbSc tower has the length of  $18 X_0$ . The PbGl is a composition of Pb-oxide and glass material. The contiguous volume of this material acts as both

the absorber and Cherenkov light collector. Each PbGl tower has the length of 14.4  $X_0$  and Moliere radius of 3.68 cm.

The west spectrometer consists of four PbSc sectors. Each PbSc sector consists of  $36 \times 72$  towers. The east arm consists of two PbSc sectors and two PbGl sectors. Each PbGl sector consists of  $48 \times 96$  towers. PbGl has better resolution in the energy measurement, while PbSc has better resolution in the time measurement. The energy measurement resolution in the EMCAL depends on the energy of the particles, it is written as

$$\begin{aligned}\frac{\delta E}{E} &= \frac{5.9\%}{\sqrt{E}} \oplus 0.8\% \quad \text{in PbGl} \\ \frac{\delta E}{E} &= \frac{8.1\%}{\sqrt{E}} \oplus 2.1\% \quad \text{in PbSc}\end{aligned}\tag{2.6}$$

The time resolution in PbGl is 300 ps and in PbSc it is 100 ps. The use of two different type calorimeters, each with its own superiority, allows a better understanding of the systematic of the measurements.

Hadrons do not deposit all of their energy in the EMCAL therefore the EMCAL can't be used to fully detect hadronic particles. Nevertheless, especially for PbSc, it does have the capability to measure the time of flight of protons and low energy pions.

### 2.3 Summary of PHENIX DATA

The summary of the data sets collected by PHENIX is given in Table 2.1. The highlighted rows indicate the specific data sets that are analyzed in this thesis, which include the Au+Au collision data of 2007 (Run 7) and 2010 (Run 10). The  $\gamma_{\text{dir}} - h$  correlations in p+p collision that are used as a reference in this dissertation are obtained from the analysis of the data collected from 2005 (Run 5) and 2006 (Run 6) combined.

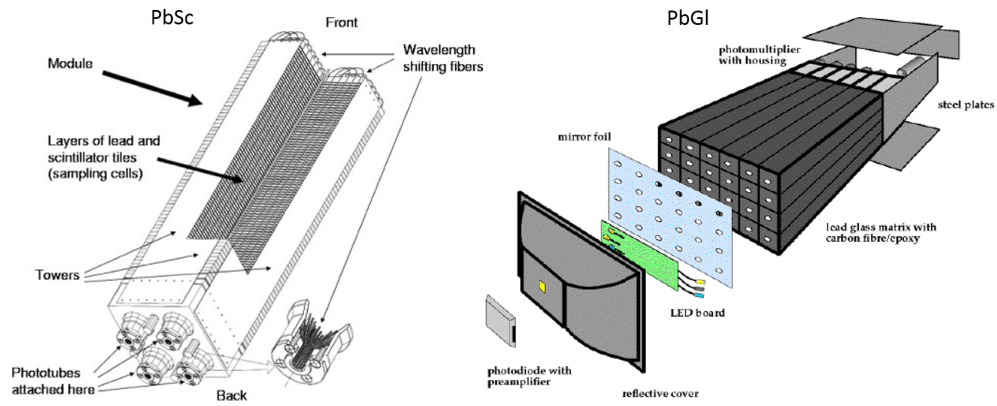


Figure 2.10: Left: A module of a PbSc detector (1 module = 4 towers). Right: A module of PbGl detector (1 module = 1 tower) [21].

Table 2.1: Summary of the data sets collected by PHENIX. Information collected from [21, 30].

Run (Year)	species	beam energy (GeV)	Luminosity	sampled events
1 (2000)	Au+Au	130	$1 \mu b^{-1}$	10 M
2 (2001-2)	Au+Au	200	$24 \mu b^{-1}$	170 M
	p+p	200	$0.15 pb^{-1}$	3.7 B
3 (2002-3)	d+Au	200	$2.74 nb^{-1}$	5.5 B
	p+p	200	$0.35 pb^{-1}$	6.6 B
4 (2003-4)	Au+Au	200	$241 \mu b^{-1}$	1.5 B
	Au+Au	62.4	$9 \mu b^{-1}$	58 B
5 (2005)	Cu+Cu	200	$3 nb^{-1}$	8.6 B
	Cu+Cu	62.4	$0.19 nb^{-1}$	400 M
	Cu+Cu	22.4	$2.7 \mu b^{-1}$	9 M
	p+p	200	$3.8 pb^{-1}$	85 B
6 (2006)	p+p	200	$10.7 pb^{-1}$	233 B
	p+p	62.4	$0.1 pb^{-1}$	28 B
7 (2007)	Au+Au	200	$813 \mu b^{-1}$	5.1 B
8 (2008)	d+Au	200	$80 nb^{-1}$	160 B
	p+p	200	$5.2 pb^{-1}$	115 B
9 (2009)	p+p	500	$14 pb^{-1}$	308 B
	p+p	200	$16 pb^{-1}$	936 B
10 (2010)	Au+Au	200	$1.3 nb^{-1}$	7.7 B
	Au+Au	62.4	$0.11 nb^{-1}$	700 M
	Au+Au	39	$40 \mu b^{-1}$	250 M
	Au+Au	7.7	$0.26 \mu b^{-1}$	1.6 M

### 3 Analysis Methods

In this chapter, we will discuss the analysis procedures that are applied in the measurement of the  $\gamma_{\text{dir}} - h$  pair correlations. The description will be divided into two parts; first is the discussion on measurements of two-particle correlations in general, and second is about the measurement of  $\gamma_{\text{dir}} - h$  pairs specifically.

#### 3.1 Two-particle correlations

We have seen an example of two-particle correlations in Fig. 1.8 (Chapter 1) . In that plot, the peak at near-side and away-side are interpreted as correlations coming from jet particles. A naive count would also include pairs from underlying event particles, which are physically not correlated. For our purpose, we categorize such kind of non-jet pairs as the background, and should be removed from the overall pairs.

The correlations shown in Fig. 1.8 are already background subtracted, therefore it represents a pure jet physics. STAR detectors that produce such results have a full  $2\pi$  coverage in azimuth and a pretty long rapidity coverage. That is not the case in PHENIX (Chapter 2), and that introduces the need of an acceptance correction in the measurement. In the following, we will describe the corrections that come from detector limitation, and continue with identifying the background from the overall pairs.

### 3.1.1 Acceptance correction

The correction that comes from the limited coverage of PHENIX central arm is encapsulated in the *Acceptance Function* ( $\text{Acc}(\Delta\phi)$ ). The coverage of azimuth difference between two particles can be derived using the known azimuthal coverage of single particle, in two steps. The first step is to transform one axis of the two-dimensional coverage picture ( $\phi_1$  vs  $\phi_2$ ) into an azimuth different ( $\phi_1$  vs  $\Delta\phi$ ). Second step is to project the transformation into one dimensional function of  $\Delta\phi$ . The procedure is depicted in Fig. 3.1. We can see that the maximum Acceptance Function is located at zero separation angle, while the minimum, with value of almost zero, happen at perpendicular separation.

In reality, the azimuthal acceptance does not perfectly cover the boxes in the top panel of Fig. 3.1, due to dead zones on the detector that keeps appearing, because of various reasons. Furthermore, the dead zone locations might change with time as the usage and maintenance are kept undergoing. This causes the Acceptance Function to vary in different events, rather than being fixed at all time. In PHENIX analysis, the Acceptance Function is obtained by taking pairs where the partner particles come from different events, or the *mixed pair*. There should be no physics correlations between them, therefore the apparent correlations are regarded as an acceptance effect.

We define the Acceptance Function as

$$\text{Acc}(\Delta\phi) = \frac{2\pi}{\int \frac{dN_{mix}^{ab}}{d\Delta\phi} d\Delta\phi} \frac{dN_{mix}^{ab}}{d\Delta\phi} \quad (3.1)$$

Where  $N^{ab}$  means number of  $a$  and  $b$  particle pairs. The numerator on the first term is an integration constant such that the Acceptance Function is normalized to the total azimuth space of  $2\pi$ . In most cases, it is convenient to use only half region of the azimuthal ( $0$  to  $\pi$ ) because of symmetry, and for those cases the integration

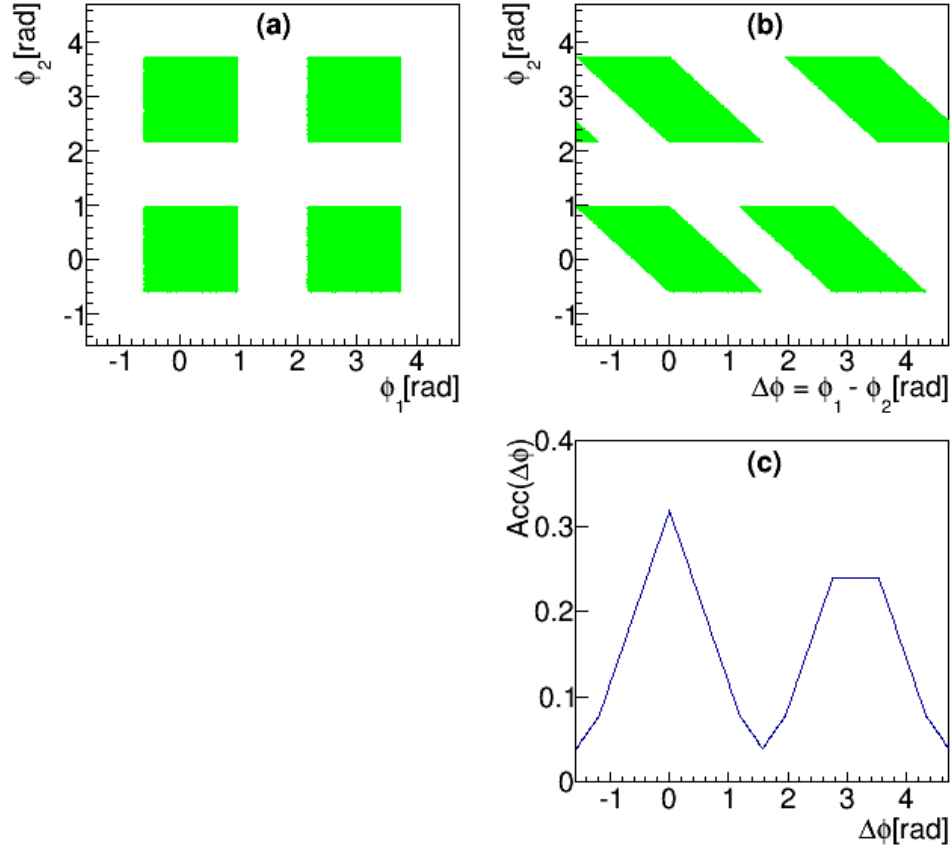


Figure 3.1: Depiction of Acceptance Function of the PHENIX central arms. (a) Coverage region with respect to two azimuthal angles. (b) Coverage region with the horizontal axis being the difference of two azimuthal angle. (c) The Acceptance function that is obtained by projection of (b) to the horizontal axis.

constant will be  $\pi$ . Number of different events to be mixed could go up to few hundreds, but we must make sure that those events are close to each other in time. The number of real pairs (coming from the same event) is corrected according to  $dN^{ab}/d\Delta\phi = 1/\text{Acc}(\Delta\phi) \times dN_{raw}^{ab}/d\Delta\phi$ .

### 3.1.2 Combinatoric Background

The background pairs are those that are composed by the underlying event. They will show a certain amount of correlations which are the remnant of the anisotropic QGP. They are also called as the combinatoric or random pairs. The background is determined by it's two characterizations, the scale and the shape. There are two methods in determining the scale, and one method in extracting the shape. These three methods will be discussed in this section.

#### Background shape: harmonic flow

In the case of heavy ion collision, as we discuss in Chapter 1, there is a flow effect that causes the single particle multiplicities to be distributed anisotropically in the azimuth direction. A random pairing of particles coming from two anisotropic distributions would inherently produce an anisotropic shape. The distribution of particle pairs can be mathematically calculated using the distribution of the single particles (Eq. 1.2); and it gives

$$\frac{dN_{comb}^{ab}}{d\Delta\phi} \propto 1 + 2v_2^a v_2^b \cos(2\Delta\phi) + 2v_3^a v_3^b \cos(3\Delta\phi) + \dots \quad (3.2)$$

In the case of p+p collision, no thermalized medium is created such that there is no flow effect. That is equivalent with saying that the  $v_n$  coefficients are zero, and it would results in a flat shape of the combinatoric background. The difference in combinatoric shape between heavy ion and p+p collision is shown in Fig. 3.2.

In previous PHENIX measurements of  $\gamma_{\text{dir}} - h$  pair correlations (as well as other pair species), we mostly include only the second order component of the flow ( $v_2$ ), which is called the elliptic flow. First reason for that is that the elliptic flow is the dominant factor in the initial geometry. We have seen in Fig. 1.4 that to the first order, the cross-sectional area of the collision does form the shape of an ellipse.

Correlation function and the combinatoric background

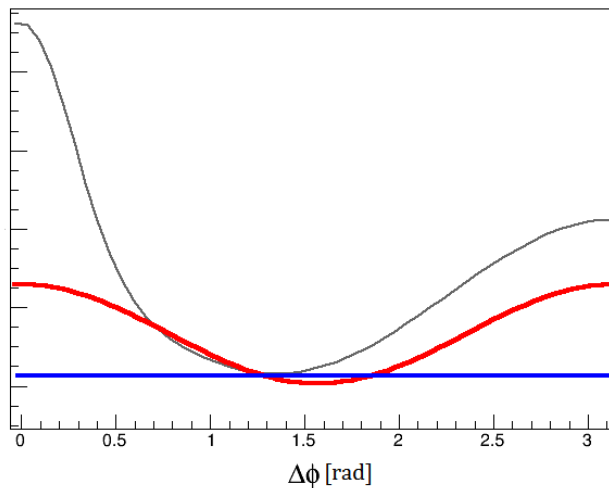


Figure 3.2: Example of a correlation function and the combinatoric shapes. In grey is the correlation function. Red is the combinatoric shape in Au+Au following Eq. 3.2 up to the second harmonics. Blue is the combinatoric shape in p+p that follows a flat line.

The higher order components arise due to fluctuations and can be thought of as perturbations to the perfect almond shape, therefore we can expect them to become smaller. Second is a more practical reason, where most of the time we do not have a complete data of harmonic flow measurement to the higher order.

Recently at an approximately the same time of the completion of this thesis, measurements of higher order harmonics are completed in a separate analysis by the collaboration. We still haven't included them in the background determination, but they are taken into account in the study of systematic uncertainties. Later we will have a dedicated section that will discuss systematic errors from all sources.

## Background level I: ZYAM

The first method in determining the background scale (which historically is the first to be used in PHENIX [31]) is called Zero Yield at Minimum (ZYAM). The level of combinatoric pairs is estimated using the assumption that there is a point on  $\Delta\phi$  where the yield of the jet correlations is zero. This is reasonable because jet particles in an event are localized at some limited spatial region, and therefore some regions in space are free from jet particles. In the case of an event with back-to-back jets, we can imagine that such region will fall around  $\Delta\phi = \pi/2$ .

One complication in finding the minimum point of the pair correlations comes from the finite binning of  $\Delta\phi$ . When statistical fluctuation is big enough, it can lead us to the wrong point of the minimum. Also, if we would change the size of the histogram bins, large fluctuation can also cause the position of the minimum to be shifted. In brief, the location of the minimum is sensitive to the way we bin the histogram, with increasing sensitivity as the statistical fluctuation is larger.

Another complication is that we are expecting the minimum point to lie around  $\Delta\phi = \pi/2$ , which coincides with the point where the acceptance is the worst (see Fig. 3.1). Due to large acceptance uncertainty, and sensitivity to histogram binning, the minimum point is determined using a fit function to the histogram. The ZYAM method is illustrated in Fig. 3.3. From here onward we will denote the level of combinatoric pairs as  $b_0$ .

As the fit function, we set it to be a gaussian around the near side and double gaussian around the away side, plus an overall elliptic flow, and a constant (see Eq. 3.3). But, it is not impossible that other combination of functions could fit the pair correlation just as well. It is the nature of applying function fitting that many uncertainties arises. Other than different kind of functions, we could also get different value of parameters from different methods in the fitting algorithm. We

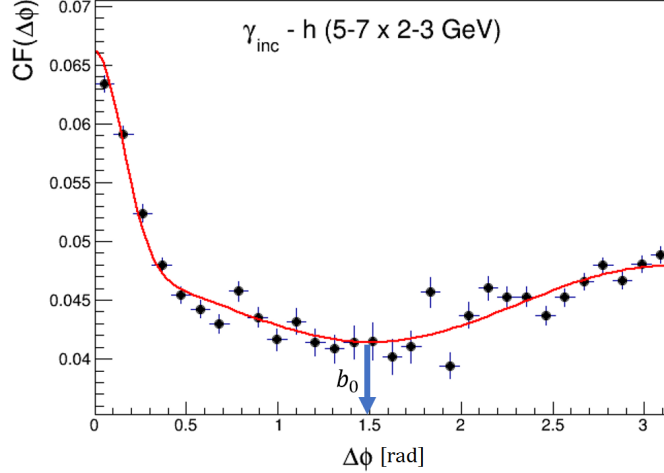


Figure 3.3: The background level  $b_0$  is determined from the minimum of the fit to the correlation functions.

concluded that the fitting method will not give an accurate estimate of the background level. Therefore, this method is not used.

$$\begin{aligned}
 f(\Delta\phi) = & a_0(1 + 2a_1 \cos(2\Delta\phi) + a_2 \frac{1}{a_3 \sqrt{2\pi}} \exp\left(-\frac{\Delta\phi^2}{2a_3^2}\right) \\
 & + a_4 \frac{1}{a_5 \sqrt{2\pi}} \left[ \exp\left(-\frac{(\Delta\phi - (\pi - a_6))^2}{2a_5^2}\right) + \exp\left(-\frac{(\Delta\phi - (\pi + a_6))^2}{2a_5^2}\right) \right. \\
 & \left. + \exp\left(-\frac{(\Delta\phi + (\pi - a_6))^2}{2a_5^2}\right) + \exp\left(-\frac{(\Delta\phi + (\pi + a_6))^2}{2a_5^2}\right) \right] \\
 & + a_7 \frac{1}{a_8 \sqrt{2\pi}} \exp\left(-\frac{\Delta\phi^2}{2a_8^2}\right)
 \end{aligned} \tag{3.3}$$

### Background level II: ABS

The other method in determining the background level is the Absolute Normalization (ABS). The basic premise in this method is that we can obtain the

per-trigger combinatoric pair by averaging the mixed pair per every trigger:

$$\bar{b}_0 = \frac{N_{mix}^{ab}}{N_{mix}^a} \quad (3.4)$$

Basically, Eq. 3.4 is a true measure of the background in the particular event where the trigger  $a$  is. In reality, we are doing a statistical measurement where the correlations function is measured over an integration of many events. The integration covered different events over a range of centrality values. Since in principle, the background rate should vary in different centralities, correction to Eq. 3.4 is needed.

We introduce a correction factor  $\xi$  to the principle background level  $\bar{b}_0$ . It is defined as the ratio of averaged of real pairs to the averaged mixed pairs:

$$\xi = \frac{\langle N^a N^b \rangle}{\langle N^a \rangle \langle N^b \rangle} \quad (3.5)$$

where the average is taken over different events in some range of centralities (or centrality classes).

In order to perform the averaging, several steps are involved. First is to obtain the distribution of trigger and partner numbers ( $n^{(a,b)}$ ) with respect to two variables:  $N_{part}$  and  $N_{coll}$ . The distribution is smoothed by applying function fitting. There are two functions (Fig. 3.4) that can be used equally well; the inverse tangent (Eq. 3.6) and the saturated exponential (Eq. 3.7).

$$n^{(a,b)} = \gamma \arctan(\beta N_{(part,coll)}) \quad (3.6)$$

$$n^{(a,b)} = \gamma(1 - e^{-\beta N_{(part,coll)}}) \quad (3.7)$$

Next, a calculation using Glauber Monte Carlo (GMC) method is performed to convert  $N_{part}$  and  $N_{coll}$  into a probability function, for each centrality classes (Fig. 3.5). Finally, the avarage is carried over different  $N_{(part,coll)}$  in a fix centrality class,

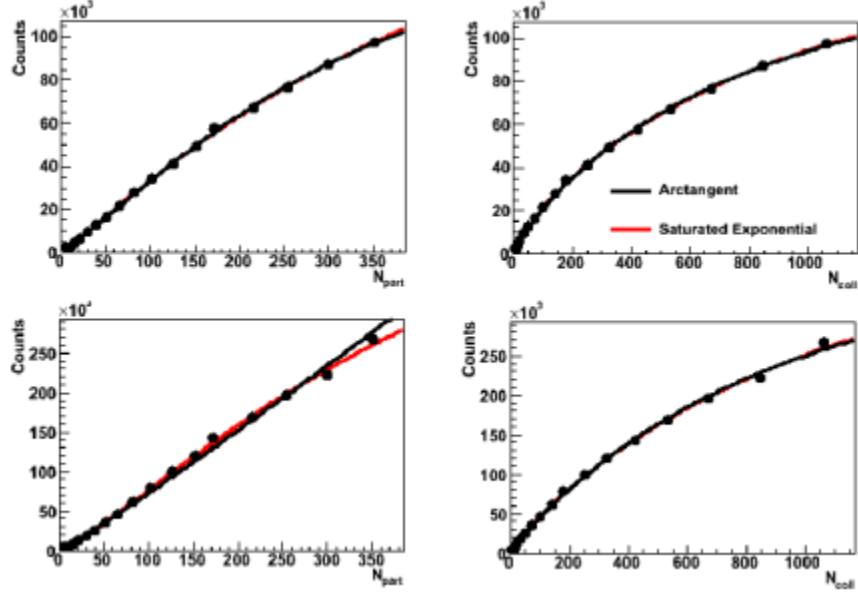


Figure 3.4: The distribution of triggers (top) and partners (bottom) with respect to  $N_{part}$  (left) and  $N_{coll}$  (right), and two fit functions.

thus can write

$$\xi = \frac{\sum_i P_i n_i^a n_i^b}{\sum_i P_i n_i^a \sum_i P_i n_i^b} \quad (3.8)$$

$P_i$  is the probability obtained from the GMC calculation.

Overall we have four different values of  $\xi$  that come from the uses of two fit functions and two variables ( $N_{part}$  and  $N_{coll}$ ). The average of the four is used as the final value, and the spread of the four is used as the systematic uncertainty. This method is also called *Mean Seed Mean Partner*(MSMP), from the part where we have use the mean partner and mean trigger (seed) in evaluating the  $\xi$  factor. The correction constant  $\xi$  is used to correct the principle background level according to

$$b_0 = \xi \frac{N_{mix}^{ab}}{N_{mix}^a} \quad (3.9)$$

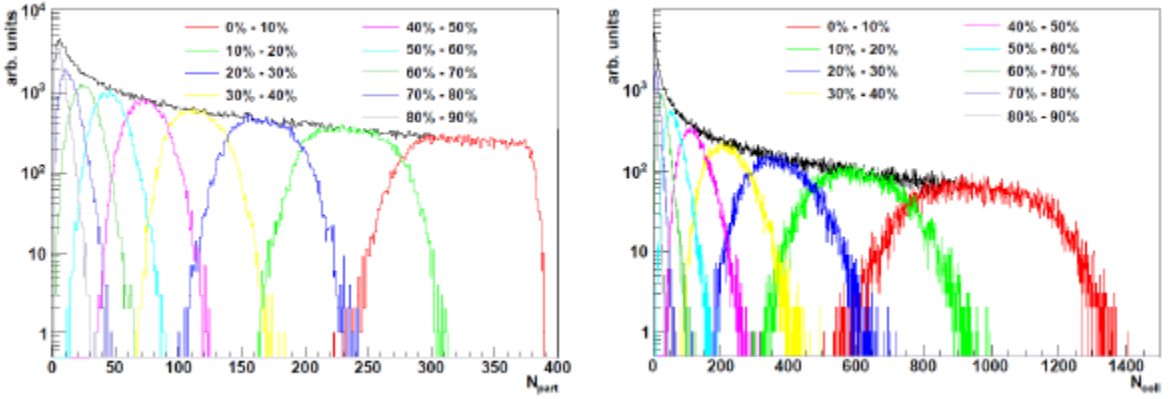


Figure 3.5: The probability function of  $N_{part}$  and  $N_{coll}$  from the calculation using GMC.

### 3.1.3 Per-trigger yield

In many cases of experimental measurements, when there is the option, the measured quantity is preferably defined in the form of a ratio. The reason is that there is a possibility that there are common factors that would cancel out, which otherwise have to be measured. Not only saving the human time and energy, this also results in the removal of additional uncertainty coming from that particular factor.

When measuring two-particle correlations, we need to take into account the efficiency correction of each of the pair constituents. The efficiency factor will correct the raw measurement to that of what we would expect if we have a perfect detector. Usually the efficiency is denoted by  $\epsilon^a$  and it is a function of  $p_T$  and centrality. In this analysis, we take the ratio of the pair correlations with number of the trigger. This removes the dependencies on the efficiency of the trigger particles, and left only the dependency on the efficiency of the associated particles ( $\epsilon^b$ ).

With the operation of the Acceptance Function, removal of combinatoric pairs, and the correction from the partner efficiency, we are left with the physical per-trigger yields of the two-particle correlations function. We write the final form of the per-trigger yield, also called as the jet function, as:

$$\frac{1}{N^a} \frac{dN^{ab}}{d\Delta\phi} = \frac{1}{N^a} \frac{dN_{real}^{ab}}{d\Delta\phi} \frac{\epsilon^b}{\text{Acc}(\Delta\phi)} - \xi \frac{N_{mix}^{ab}\epsilon^b}{N_{mix}^a} (1 + 2v_2^a v_2^b \cos(2\Delta\phi)). \quad (3.10)$$

### 3.2 $\gamma_{\text{dir}} - h$ pair correlations

The whole procedure that we describe in the previous section provides the framework in measurements of particle pairs in PHENIX. When it comes to the specific measurement of  $\gamma_{\text{dir}} - h$  pair correlations, one has to first of all deal with the problems of the direct photons and the hadrons. Measurement of direct photon is not trivial, because basically we can't straightforwardly identify the type of any photon in the detector. Measurement on the hadron part is less cumbersome, especially that we are not interested in specifying the hadron species. From Eq. 3.10, we see that we also need to obtain the efficiency of the charged hadrons, but not for the photons.

#### 3.2.1 Direct Photon Measurement: The Statistical Subtraction Method

The direct photons are extracted by subtracting the decay photons from the inclusive photons. This gives the estimated portion of direct photon signals in the overall photons sample, therefore this is called the statistical subtraction method. According to the definition, the subtraction method will actually give us all non-decay photons, not necessarily the direct photons only. Other component of the non-decay photons are from NLO hard scattering processes, called as the fragmentation photons.

By definition,

$$N^{\gamma_{\text{dir}}} = N^{\gamma_{\text{inc}}} - N^{\gamma_{\text{dec}}} \quad (3.11)$$

consequently, the relation also applies to the pairs

$$\frac{dN^{\gamma_{\text{dir}}-h}}{d\Delta\phi} = \frac{dN^{\gamma_{\text{inc}}-h}}{d\Delta\phi} - \frac{dN^{\gamma_{\text{dec}}-h}}{d\Delta\phi} \quad (3.12)$$

From those definitions, we can derive an expression for per-trigger yield of  $\gamma_{\text{dir}} - h$  correlations, written in a the simple form

$$Y^{\text{dir}} = \frac{R_\gamma Y^{\text{inc}} - Y^{\text{dec}}}{R_\gamma - 1} \quad (3.13)$$

where we have defined

$$Y^\gamma \equiv \frac{1}{N^\gamma} \frac{dN^{\gamma-h}}{d\Delta\phi} \quad (3.14)$$

and

$$R_\gamma \equiv \frac{N^{\gamma_{\text{inc}}}}{N^{\gamma_{\text{dec}}}}. \quad (3.15)$$

In short, we can not obtain the correlations of  $\gamma_{\text{dir}} - h$  pairs directly, but instead we apply the two-particle correlations procedure, as explained in the previous section, first to the inclusive photons and second to the decay photons. Measurement of the inclusive photon is done simply by sampling all the detected photons. On the other hand, the decay photons have to be estimated. Again, this is due to the inability of the detector to identify types of photons. We may say that the direct photons are measured in a doubly indirect manner.

### 3.2.2 Decay Photon Measurement

The amount of decay portion from the inclusive photon signals are estimated from the measured neutral pions ( $\pi^0$ ) in the sample. 99 percent of the time, the  $\pi^0$  would decay into photon pairs [4].  $\pi^0$ , being the lightest is also the most produced meson after the collision. Therefore, estimation based on  $\pi^0$  already constitute most

part of the decay photons. The second largest contribution would come from eta ( $\eta$ ) mesons. In this analysis, contribution from  $\eta$  meson is included in term of a correction factor, based on the known production ratio of  $\pi^0$  over  $\eta$ .

The amount of decay photons is estimated using a Green's function that is applied to the  $\pi^0$  spectrum. The Green's function, or the probability function, can be derived analytically based on the kinematics of  $\pi^0 \rightarrow \gamma\gamma$  decay process. In the experiment, there are real detector effects that would modify the analytic probability. They include the limited coverage and finite resolution in detecting the photons. An alternative to the analytic method is to derive the probability function with a Monte Carlo simulation, that have the ability to incorporate real detector effects.

### Analytic probability function

In the lab frame, the photons that are produced by the decay of relativistically moving  $\pi^0$ , will have a uniform probability to have any energy in the range of  $0 < E^\gamma < p^{\pi^0}$ . We can normalize such constant probability density, and obtain that the probability to find a decay photon with any energy less than  $p^{\pi^0}$ , is equal to  $2/p^{\pi^0}$ , the factor 2 came from the fact that there are two decay photons.

The probability to find a decay photon of energy  $E_1 < E^\gamma < E_2$  is then given by

$$\mathcal{P}_{\pi^0 \rightarrow \gamma\gamma}(E_1, E_2, E^{\pi^0}) = \int_{E_1}^{E_2} \frac{2}{E^{\pi^0}} dE^\gamma \quad (3.16)$$

It is dependent on the boundaries of the photon energy and the energy of the  $\pi^0$  itself. We have switched from writing the probability in terms of momentum to the energy of  $\pi^0$ . In ultra-relativistic limit both quantities are equivalent. Furthermore, because the maximum photon's energy is limited to that of it's parent, there are

three scenarios where the integral can be solved, and they are

$$\mathcal{P}_{\pi^0 \rightarrow \gamma\gamma}(E^{\pi^0}) = \begin{cases} 0 & \text{if } E^{\pi^0} < E_1 \\ \frac{2(E^{\pi^0} - E_1)}{E^{\pi^0}} & \text{if } E_1 < E^{\pi^0} < E_2 \\ \frac{2(E_2 - E_1)}{E^{\pi^0}} & \text{if } E_2 < E^{\pi^0} \end{cases} \quad (3.17)$$

As we are working with ultra-relativistic photon particles, added with the fact that they lie at mid-rapidity region, the most convenient variable to use is the transverse momentum ( $p_T$ ). In this analysis, we have used several binning sizes of the decay photon's  $p_T$ , with the overall range of 5-20 GeV, the same of that for inclusive photons. For each  $p_T$  bin, the amount of decay photons is estimated from the integrated product of  $\pi^0$  spectra and the Green's function in Eq. 3.17.

Mathematically we write that as

$$N^{\gamma_{dec}} = \int \mathcal{P}_{\pi^0 \rightarrow \gamma\gamma}(p_T^{\pi^0}) \times \frac{dN^{\pi^0}}{dp_T^{\pi^0}}(p_T^{\pi^0}) dp_T^{\pi^0} \quad (3.18)$$

The same principle is applied to the number of pairs, where we can replace  $dN^{\pi^0}$  with  $dN^{\pi^0-h}$  and  $N^{\gamma_{dec}}$  with  $N^{\gamma_{dec}-h}$ .

### Simulation generated probability function

The simulation can be described as having two steps, first is generation of the  $\pi^0$ s and their decay process to two photons, and second is encoding the detector effects in the simulation that will affect the readings of decay photons. A Monte Carlo code is used to generate  $\pi^0$ s, with weights according to a published spectrum, and to let them decay to two photons. The decay photons are then read out, taking into account the effects coming from the acceptance, energy resolution and the dead/hot tower map of the EMCAL detector.

The limited acceptance could potentially introduce different behaviour of the probability function at different region of the EMCAL. There are cases where one or

two decay photons are lost because they fly outside the detector. The probability for that to happen is larger when the  $\pi^0$  is located near the edge of the detector. This is taken into account by generating separate probability functions based on the longitudinal ( $z$ ) location of  $\pi^0$ . In total we made 33  $z$  segmentation of the EMCal.

One correction is not included in the FastMC code but instead is calculated separately, and that is what we call as the merging effect. As the energy of  $\pi^0$  is getting larger, the opening angle between two decay photons tend to become smaller. This causes both photon to produce EMCal clusters that largely overlap. The EMCal can not differentiate whether it is a cluster of high energy photons or a cluster made of two photon sisters. In that case the signal is thrown away, and thus a fraction of decay photons are lost.

Signal loss due to the merging effect is determined from a full detector simulation based on the GEANT software [32]. PHENIX has developed a GEANT based framework that simulates all subsystem detectors response, and it is called PISA (PHENIX Integrated Simulation Application). The Monte Carlo generated and decaying  $\pi^0$ s are passed through PISA, and that will give detector hits, the same way as the real particle produces. The PISA hits are then reconstructed by PHENIX reconstruction software, called PISAtodST, the same way real detector hits are reconstructed. By comparing the reconstructed photons with the known generated signal, the merging loss effect can be extracted.

The shape of the probability function, obtained from analytic method or from simulation, both resembles that of a fin of a shark. Therefore the nickname *sharkfin* is often used to refer to the probability function. In Fig. 3.6 we show three different sharkfins, each is obtained from analytic, Monte Carlo simulation with detector resolution effect, and simulation with additional effect from merging loss. We can see that the Monte Carlo method produces smearing at the otherwise sharp point of

the minimum and maximum of the analytic function, and that the merging effect is mostly significant at high  $\pi^0$  energy.

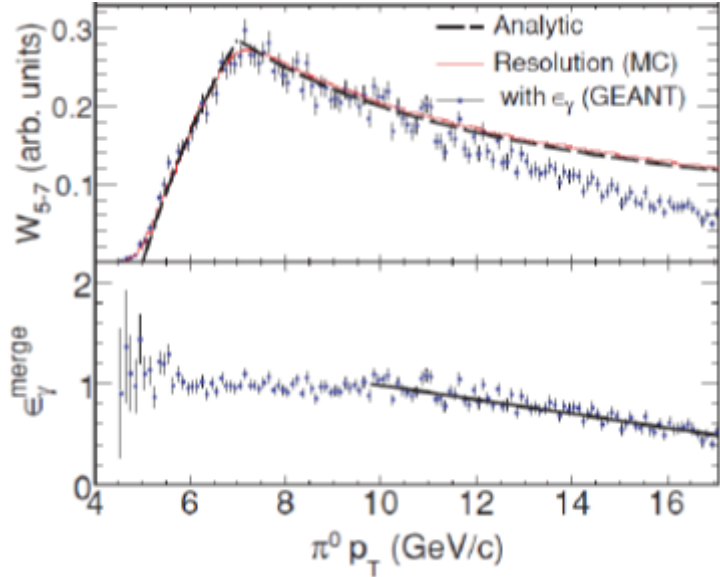


Figure 3.6: Top: Three different probability functions; analytic (dashed black), Monte Carlo without merging effect (solid red) and Monte Carlo with merging effect (data point). Bottom: The correction function from the merging effect from full PISA simulation [33].

The sharkfins that we have generated, to put it simply, will transform *true*  $\pi^0$  spectra to the *detected* decay photons. In this analysis, the  $\pi^0$ s are measured by calculating the invariant mass of two photons in the sample. Before we can apply the sharkfin, the measured  $\pi^0$  should first of all be corrected according to the true spectra. This is done by the  $\pi^0$  efficiency correction that we will discuss in the next section.

The summary of mapping procedure from raw  $\pi^0$  to decay photons that we would measure is depicted in Fig. 3.7. In this method, we make sure that the final

decay photons that we obtain are within a portion of the inclusive photon samples, such that statistical subtraction formula can be used.

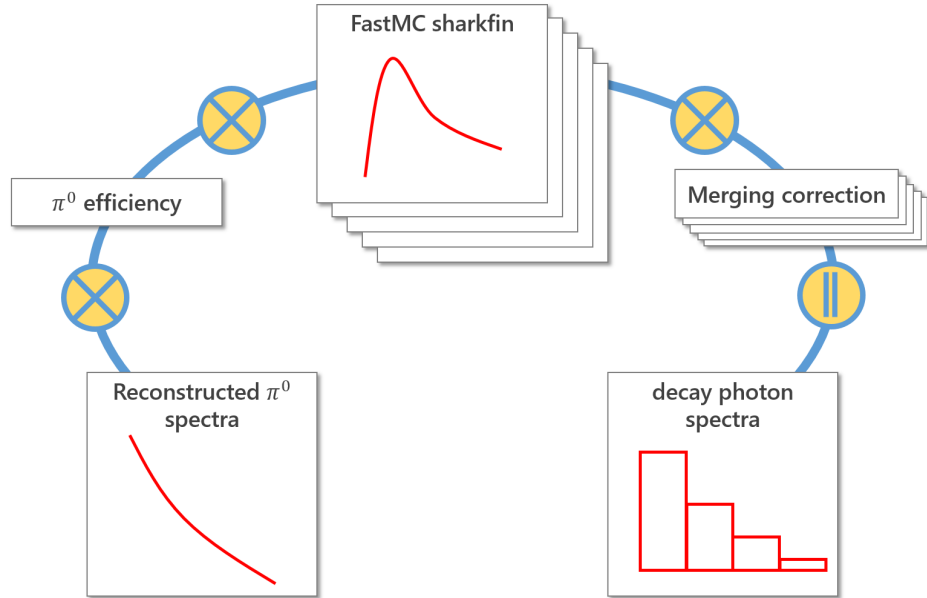


Figure 3.7: Description of the mapping procedure from the reconstructed  $\pi^0$  spectra to decay photon's spectra.

### 3.2.3 $\pi^0$ Measurement

Since we have set the range for the trigger  $p_T$  to be 5 to 15 GeV, we are only interested with  $\pi^0$  with  $p_T$  of 4 to 17 GeV. The lower limit is slightly less than the minimum trigger  $p_T$ , to take into account the effect from finite resolution of the detector. Such effect is seen in the simulated sharkfin (Fig. 3.6) as the smoothing at the minima and maxima. In principle, there is no upper limit for  $\pi^0$  momentum since they can always decay to low energy photons, the 17 GeV limit is set because we start losing  $\pi^0$  signal due to the merging effect.

$\pi^0$ s are measured by taking pairs of photons and examining their invariant mass. The invariant mass squared can be written in terms of the energy of each photon and their separation angle ( $\phi_{\gamma\gamma}$ ) as

$$m_{\gamma\gamma}^2 = 2E^{\gamma_1}E^{\gamma_2}(1 - \cos \phi_{\gamma\gamma}). \quad (3.19)$$

True decay photon pairs in an ideal detector will give an invariant mass that coincides with the mass of  $\pi^0$ , which is around 0.134 MeV. Because of finite detector resolution, the invariant mass distribution will form a gaussian spread around the  $\pi^0$  mass, with a width that reflects the precision of the detector.

Some random pairs can accidentally give invariant mass that fall in the gaussian region; they are considered as backgrounds. The background usually form a linear function, with the gaussian shape sitting on top of it. The linear function has a slightly increasing trend towards high invariant mass, the gaussian peak also appeared slightly tilted to the same direction. This is caused by the fact that the detector resolution is dependent on the photons energy (Eq. 2.6). Resolution is better for the high energy photon, therefore they spread less, and this results in smearing towards large invariant mass. In this analysis, the ratio of signal-to-background is minimized by several approaches that we describe below.

We use only photons with energy higher than 1 GeV, and the total of the two should be larger than 4 GeV. We also choose a narrow region of invariant mass around the mean, signal-to-background is getting larger as we go away from the mean. We have set the range of the invariant mass to be  $0.12 < m_{\gamma\gamma} < 0.16$  (GeV). Other cut that was applied to increase the signal-to-background ratio is the asymmetry cut. Because of the abundance of low energy soft photons, combinatoric pairs (of a certain invariant mass) are most likely to be formed by a low energy photon and its high energy counterpart. In other words, combinatoric pairs are

most likely coming from pairs with large asymmetry. This is especially true in the central collision, due to high multiplicity.

The asymmetry is defined as

$$a = \left| \frac{E^{\gamma_1} - E^{\gamma_2}}{E^{\gamma_1} + E^{\gamma_2}} \right| \quad (3.20)$$

We have applied the asymmetry cut only in the central to mid-central events (centrality < 40%), and in a lower  $\pi^0$  energy range of 4.00-5.25 GeV. In the higher  $p_T$  region, with invariant mass range that we used, low  $p_T$  photons are no longer contributing. The asymmetry is set to be a function of  $\pi^0$  energy:

$$a = 0.15 + 0.85(E_{\pi^0} - 4.0)^2/1.25^2.$$

In Fig. 3.8, we showed the resulting invariant mass distribution after those cuts are applied. We concluded that we have reached a high signal-to-background ratio. The ratio is only bad in the case of central events and low  $\pi^0 p_T$ . Since we have a finite amount of background, a correction still needed to be introduced. In this analysis, we take into account the background amount when we examine the systematic.

### $\pi^0$ trigger efficiency

$\pi^0$  efficiency is needed when we map the raw  $\pi^0$  to decay photons (Fig. 3.7).  $\pi^0$  efficiency is obtained by taking the ratio between a power law fit of a published  $\pi^0$  invariant yield, with the one that we obtain in our measurement. The published spectra in centrality binnings that we used is shown in Fig. 3.9. The efficiency is calculated with arbitrary normalization for each centrality bins. Dependency on the overall scale of the efficiency is gone when we are taking the per-trigger yield measurement. The efficiencies that we obtain for Run 10 data set are shown in Fig. 3.10. Large differences in low  $\pi^0 p_T$  in the central and mid-central events are caused by the asymmetry cut.

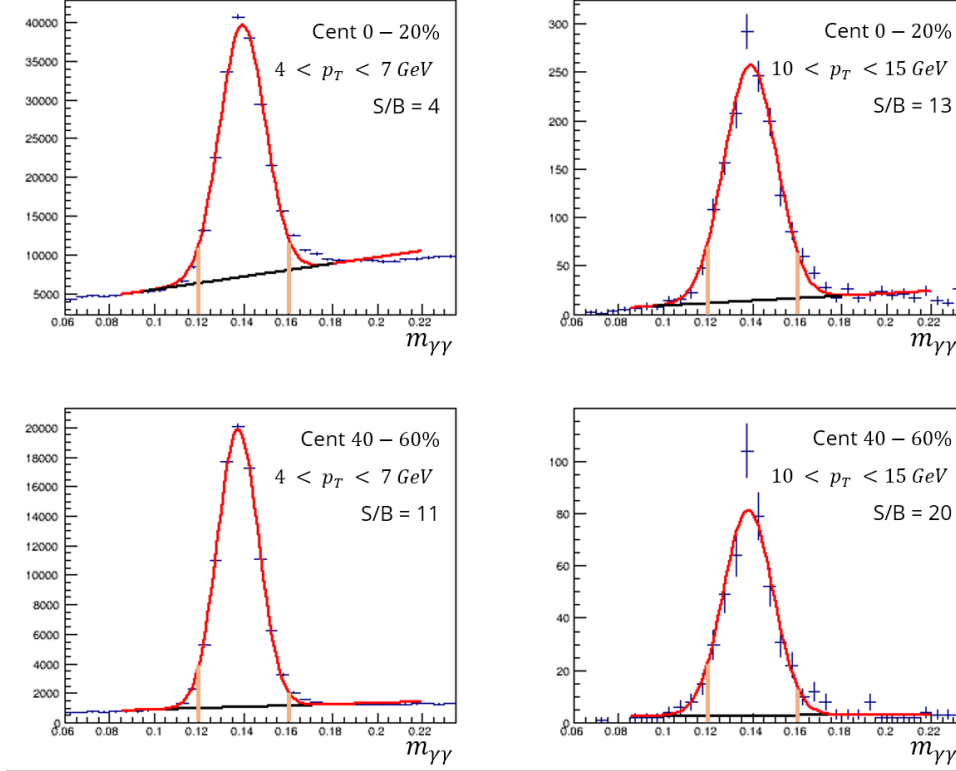


Figure 3.8: The signal-to-background ratio in the distribution of the  $\pi^0$  invariant mass, in different centrality and  $\pi^0 p_T$ .

### 3.2.4 Charged hadron efficiency

The charged hadron efficiency needs to be calculated and put in to Eq. 3.10 as  $\epsilon^b$ . The efficiency takes into account the loss or misreconstructed hadronic signals by the tracking detectors. There are two types of efficiencies, one is signal loss related to the measurement of a single track, and second is signal loss that is caused by the occurrence of multiple tracks. The first type of the efficiencies is referred to as the *single particle efficiency*, it encompasses the effect of limited acceptance and finite resolution of the tracking detector. The second type of the efficiency is called the

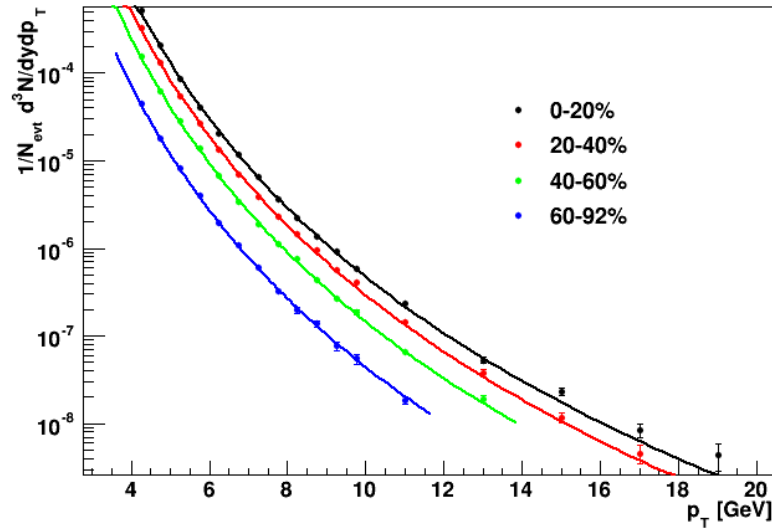


Figure 3.9: The invariant yield of  $\pi^0$  production measured in Au+Au collision with  $\sqrt{s_{NN}} = 200$  GeV [34], and their power law fit.

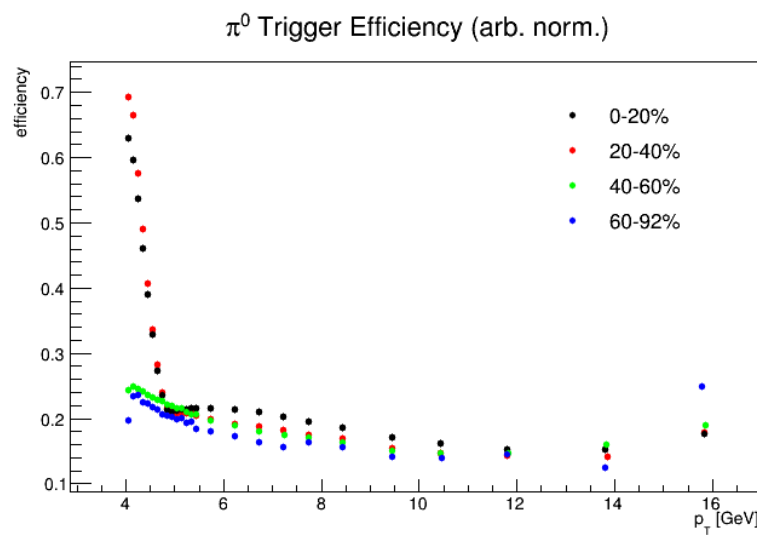


Figure 3.10:  $\pi^0$  trigger efficiency obtained for Run 10.

*occupancy correction*, it considers the fact that the detector have limited ability in separating multiple tracks that are close to each other.

In the early PHENIX analysis, the corrections are obtained from simulation that would mimic the detector response. For the analysis that comes later on, the correction can be obtained by taking the corrected measurement, usually a published spectra, and not doing any detector simulation. The later method is called bootstrap. In PHENIX, both the single efficiency and occupancy correction have been calculated with simulation using the configuration of Run 6 [36], and Run 7 [35, 36]. On those analysis, the results from the bootstrap methods are also obtained and shown to be consistent with the simulation results.

The simulation method works the same way as when we derive the PISA merging correction for  $\pi^0$  decay. In this case though, we are generating charged hadrons with the FastMC, then similarly we use PISA to produce the detector hits, and PISAtoDST to reconstruct the signals. The single particle efficiency is obtained by comparing the reconstructed signals with the originally generated signals. The results are then fitted with exponential function.

In this dissertation we are using the fit parameter values obtain from [35] for both data of Run 7 and Run 10, where we have made the assumption that the detector configuration does not change significantly between two runs. The single efficiency function is shown in Fig. 3.11 and the parameters of the exponential function is also quoted. Different fit parameters are used when  $p_T$  is higher than 5 GeV. The different is coming from the fact that below 5 GeV RICH veto is applied in charged hadron measurement, while above 5 GeV the veto is turn off (see Chapter 2 about RICH detector). The veto is applied up to  $p_T$  of 5 GeV, but in thruth the pions already start firing the RICH detector at 4.7 GeV, this causes an effect of the dip before  $p_T = 5$  GeV in the efficiency function.

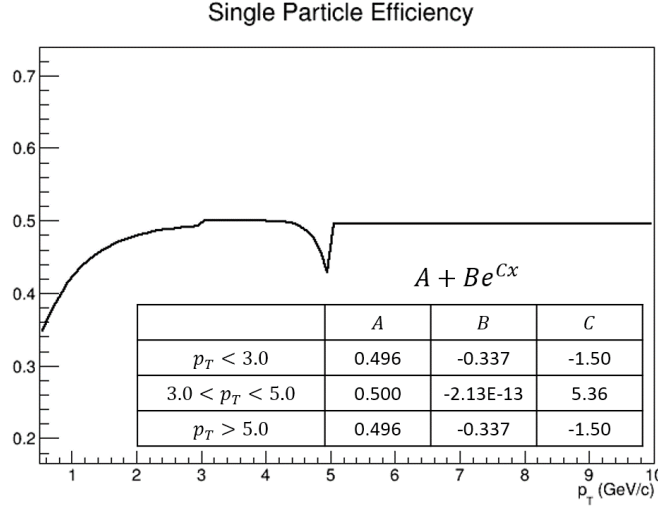


Figure 3.11: The fit function used as single charged hadron efficiency in this analysis. The function parameter on the original result of simulation is obtained from [35]. RICH veto for tracks of  $p_T$  below 5 GeV causes the dip around  $p_T = 4.7$  GeV.

The occupancy correction largely depends on the multiplicity of the event, therefore its values are obtained using embedding technique. In this method, the Monte Carlo hits are embedded real track hits before the reconstruction. The occupancy correction is obtained by comparing the reconstructed tracks with embedding (the un-merged MC tracks) and without embedding (no occupancy effect). The occupancy correction that is used in this analysis also uses the results from the studies that was reported in Andrew Adare and Megan Connors theses [35, 36].

In  $p_T > 5$  GeV region, results from [36] are used, while in  $p_T < 5$  results from [35] are used because the RICH veto wasn't applied in the former. The values of the correction naturally change with centrality. The values of the correction have small dependence on  $p_T$ , therefore they are quoted as a constant, except for the case of  $p_T > 5$  GeV at the most central 0 – 20% where an exponential fit was given. For the

range of  $p_T < 5$  GeV, the occupancy correction that were used are  $\{0.680, 0.835, 0.925, 0.975\}$  for the centrality classes  $\{0 - 20\%, 20 - 40\%, 40 - 60\%, 60 - 92\%\}$  respectively. For the region of  $p_T > 5$  GeV, the corrections are  $\{0.761 + 1.640 \exp -4.734 p_T, 0.913, 0.978, 0.992\}$ .

## 4 Additional Cuts and Data Selections

The theme of this chapter is about procedures that are making sure that the data that will be used in the analysis is clean. The first part of this chapter is regarding the isolation cut method which has the goal of reducing the decay photon background. The second part in this chapter is the more general methods of data selection that are performed prior to the analysis procedures.

### 4.1 Isolation cut

The large portion of the inclusive photons comprises of the decay photons which we consider as background in our  $\gamma_{\text{dir}} - h$  pair analysis. A rejection rule that reduces such proportion will lower the uncertainty of direct photon measurement. The ratio of the (Signal+Background)/Background  $((S + B)/B)$  is basically encoded in the value of  $R_\gamma$ . Larger  $R_\gamma$  value will result in less uncertainties. Therefore the effect of the rejection rule can also be seen as the increase of  $R_\gamma$ . One particular rejection rule that will be explored is the isolation cut.

The basis of the isolation cut is the fact that direct photons do not form a jet, nor comes from a jet, while on the other hand, high  $p_T$  decay photons are product of energetic hadrons that are very likely part of a jet. The sums of energies of particles surrounding a direct photon should be less compare to that of particles surrounding a decay photons. Therefore by selecting only *isolated* photons, it is expected that more decay photons are removed from the sample.

The isolation cut is implemented by measuring the total energy within a region (called as *cone*) in the  $\phi - \eta$  space centered around the photon location with a radius of  $R_c = \sqrt{(\Delta\phi)^2 + (\Delta\eta)^2}$  (see Fig. 4.1). A threshold energy is set, where if the cone energy is larger than that, the photon is tagged as non-isolated and removed from the sample, while if it is the otherwise, the photon is tagged as isolated and are kept for further measurement. Mathematically we can write that a photon is isolated when

$$E_{cone} < E_{TH} \quad (4.1)$$

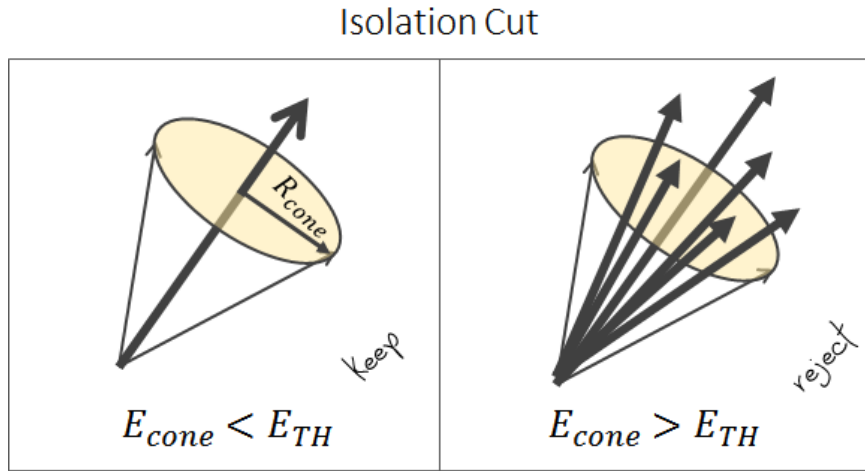


Figure 4.1: Illustration of the working principle of isolation cut in selecting isolated photons.

Such technique has been applied in many jet-related measurement in p+p collision system, including the PHENIX measurement of  $\gamma - h$  correlations in p+p [16], but not as many in a Au+Au system. The reason for that is that there is some concern that due to the high multiplicity, implementation of the isolation cut might not be so effective. To address the mentioned concern, prior to the application in

$\gamma_{\text{dir}} - h$  measurement, we perform a study to determine the most optimum way of defining the isolation cut, and to be sure that it can be effective.

#### 4.1.1 Optimization

The effectiveness of the isolation cut is judged by the reduction of the statistical uncertainties of the  $\gamma_{\text{dir}} - h$  correlations. Such statistical uncertainties can be derived based on the statistical subtraction formula, and it gives:

$$\Delta(Y^{\text{dir}}) = \frac{\sqrt{R_\gamma^2 \Delta^2(Y^{\text{inc}}) + \Delta^2(Y^{\text{dec}})}}{R_\gamma - 1} \quad (4.2)$$

From the equation above we see two aspects that govern the statistical errors. First is the value of  $R_\gamma$ , and, as mentioned earlier, the increase of  $R_\gamma$  will reduce the uncertainty. Second is the statistical error of each of the inclusive and decay photons. By applying the cut, we will increase  $R_\gamma$ , but at the same time we are cutting the statistics of each inclusive and decay photons. Therefore, an optimum isolation cut is the one that reaches the middle ground, where the  $R_\gamma$  is large enough and photon efficiency is small enough, such that Eq. 4.2 is at the minimum.

After isolation cut is applied, the effective values of  $R_\gamma$ , number of photons, and eventually the final uncertainty, will change. We define ratio factors of those values after and before the isolation cut:

$$\rho \equiv \frac{R'_\gamma}{R_\gamma} \quad (4.3)$$

$$\alpha \equiv \frac{\Delta Y^{\text{inc}'}}{\Delta Y^{\text{inc}}} \quad (4.4)$$

$$\beta \equiv \frac{\Delta Y^{\text{dec}'}}{\Delta Y^{\text{dec}}} \quad (4.5)$$

and finally

$$\sigma \equiv \frac{\Delta Y^{\text{dir}'}}{\Delta Y^{\text{dir}}} = \frac{\sqrt{\rho^2 \alpha^2 R_\gamma^2 \Delta^2(Y^{\text{inc}}) + \beta^2 \Delta^2(Y^{\text{dec}})}}{\sqrt{R_\gamma^2 \Delta^2(Y^{\text{inc}}) + \Delta^2(Y^{\text{dec}})}} \frac{R_\gamma - 1}{\rho R_\gamma - 1} \quad (4.6)$$

The optimum isolation cut is the one that produces minimum  $\sigma$ , and that is what we try to achieve, through an optimization study. We are using the distribution of cone energies to get the fraction of isolated photon, see Fig. 4.2. We define the efficiency factors based on the random and  $\pi^0$  cone distribution as follows:

$$\epsilon_i = \frac{N^{rand}(E_{cone} < E_{TH})}{N^{rand}}, \quad \epsilon_p = \frac{N^{\pi^0}(E_{cone} < E_{TH})}{N^{\pi^0}} \quad (4.7)$$

The random cone is used because we wish to capture the effect of the underlying event, while the  $\pi^0$  cone is used to approximately derive the effective  $R_\gamma$ , without a further mapping to decay photons.

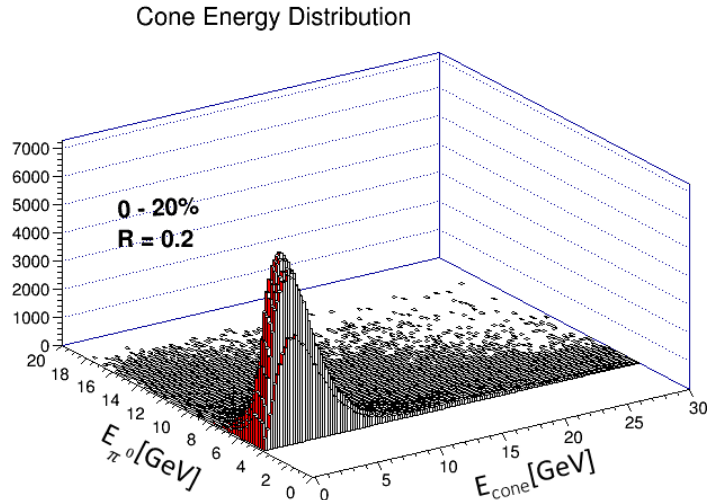


Figure 4.2: Distribution of the cone energy around  $\pi^0$  for different  $\pi^0$  energies.

The  $\rho$  factor is approximated simply by  $\rho = \epsilon_i/\epsilon_p$ . For  $\alpha$  and  $\beta$ , we use fit function from data analysis that relates the changes of direct photon uncertainties with the efficiencies of inclusive and decay photons. We are using  $\alpha = \epsilon_i^{-0.4}$ , and  $\beta = 0.8\epsilon_d^{-0.4}$ . With this definition, we can calculate  $\sigma$ , and we are looking for its minimum value in variation of  $E_{TH}$ , as well as the cone size. Plots of  $\sigma$  values from different  $R_{cone}$  and as function of threshold energy are shown in Fig. 4.3.

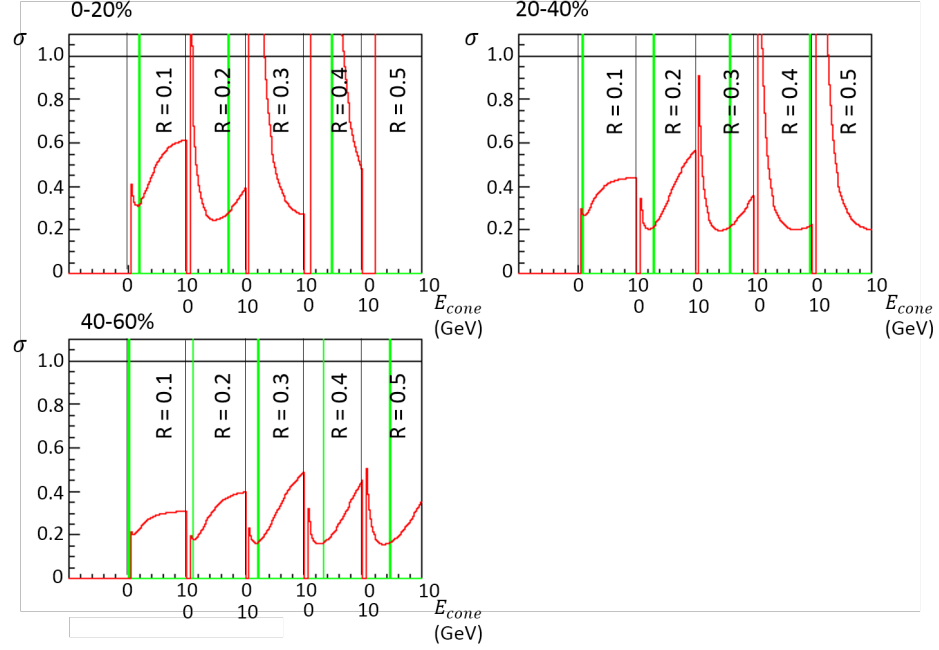


Figure 4.3: Value of  $\sigma$ s. Green line is mean energy of the random cone. The isolation cut parameters are set based on or close to the locations of the minimum  $\sigma$ .

The standard isolation cut in p+p uses the parameters of  $R_{cone} = 0.3$  and  $E_{TH} = 0.1 \times E_\gamma$ . Based on the sigma values, it's clear that we would actually like to use different values of  $R_{cone}$  on different centralities. That makes sense because essentially the density of particle multiplicities varies with centrality. We also argue that in Au+Au there is the bulk underlying event energy, that could be represented by the mean energy of the random cones (green lines in Fig. 4.3), that also changes in different centralities. That will be incorporated by introducing a constant factor to the threshold energy. Therefore, now the threshold is determined using three parameters, and it looks like:

$$E_{TH} = a \cdot E_\gamma + b \quad (4.8)$$

As a result of our optimization study, we come up with the following set of isolation parameters:

Table 4.1: The parameters of isolation cut used in this analysis.

Centrality	$R_{cone}$	$a$	$b$
0 - 20%	0.1	0.1	2.0
20 - 40%	0.2	0.1	4.0
40 - 60%	0.2	0.1	2.0
60 - 92%	0.3	0.1	1.0

#### 4.1.2 Modification of the decay mapping

In principle, the decay process is independent from energy density of the surrounding environment, therefore one can say that if a  $\pi^0$  is isolated than automatically the decay photons are isolated as well. On that basis, one can use the 'normal' probability function (section 3.2.2) in mapping isolated  $\pi^0$  to the isolated photons. However, that can only be applied in an ideal situation where we can exactly identify the pairing of the decay products.

In the method that is implemented in this analysis, we do not identify the decay pairs, therefore the decay sister now becomes part of the surrounding and add a contribution to the original  $\pi^0$  cone energy. On that basis, we can say that in general the cone energy around the decay photon is larger than that of the  $\pi^0$ . As consequences, a non-isolated pion will always produce non-isolated decay photons, while an isolated pion have the possibility to produce both isolated and non-isolated decay photons.

A modification to the 'normal' decay mapping method is therefore necessary when the isolation cut is applied to the  $\pi^0$  and the photons. In this analysis, such modification is performed by introducing an additional 'isolation probability function'. In principle, such function denotes the probability that the decay photon is isolated, given that the pion is. Such probability function is formed the same way as the decay mapping probability function does, which is as function of  $\pi^0$  energy, and defined in different energy bins of the decay photons.

In generating the isolation probability function, we start by looking at the changes of the cone energy around the  $\pi^0$  and the decay photons. The cone energy around the decay photon is simply

$$E_{cone}^\gamma = E_{cone}^{\pi^0} + (E_{\pi^0} - E_\gamma) \quad (4.9)$$

The photon is isolated when

$$E_{cone}^{\pi^0} + (E_{\pi^0} - E_\gamma) < aE_\gamma + b \quad (4.10)$$

or

$$E_{cone}^{\pi^0} < (a + 1)E_\gamma + b - E_{\pi^0} \quad (4.11)$$

Basically what we have now is a threshold for the pion cone energy that will determine whether the decay photon is isolated or not, given that the  $\pi^0$  is isolated. One can then generate the probability function using the distribution of cone energy around the  $\pi^0$ , like in Fig. 4.2, with Eq. 4.11 as the condition.

The  $\pi^0$  cone distribution in Fig. 4.2, together with the parameters in Table 4.1, gives the isolation probability function shown in Fig. 4.4. Finally, the mapping procedure from isolated  $\pi^0$  to the isolated photon can be written as

$$N_{iso}^{\gamma_{dec}} = \int \mathcal{P}_{iso}(p_T^{\pi^0}) \times \mathcal{P}_{\pi^0 \rightarrow \gamma\gamma}(p_T^{\pi^0}) \times \frac{dN_{iso}^{\pi^0}}{dp_T^{\pi^0}}(p_T^{\pi^0}) dp_T^{\pi^0} \quad (4.12)$$

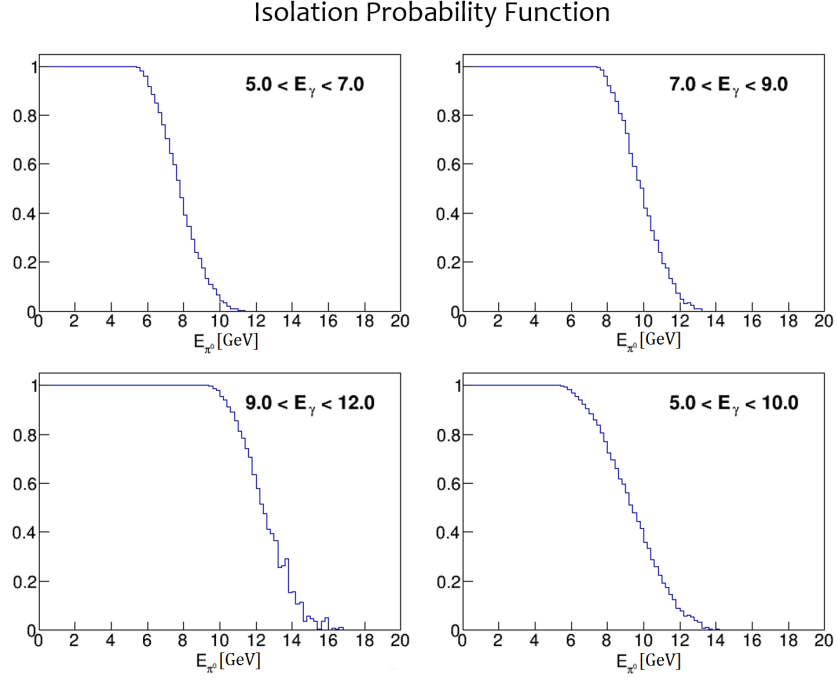


Figure 4.4: The isolation probability function as function of  $\pi^0$  energy for different ranges of decay photon energy.

#### 4.1.3 Modification of the $R_\gamma$

When performing the analysis without the isolation cut method we don't need to worry about the value of  $R_\gamma$  because it is already measured. Unfortunately, there is no such measurement where isolation cut was applied (measurement of  $R_\gamma^{eff}$ , as we say). If there is one, we also have to be sure that the isolation parameters are the same, for the result to be applicable in this analysis, which increases the probability that there is none of such result that can actually be used. Therefore a method in estimating  $R_\gamma^{eff}$  is necessary in this analysis.

More precisely the factor that we are estimating is the  $\rho$  factor in Eq. 4.3.

Based on the definition of  $R_\gamma$  and  $R_\gamma^{eff}$ , than the exact formula for  $\rho$  should be

$$\rho = \frac{N_{inc}^{iso}}{N_{inc}} \frac{N_{dec}}{N_{dec}^{iso}} \quad (4.13)$$

The estimate of  $\rho$  is calculated by taking the uncorrected or raw version of the exact formula, with the assumption of all measurement efficiency behaves the same when isolation cut is off or on. Therefore we write the  $\rho$  estimate as

$$\rho = \frac{M_{inc}^{iso}}{M_{inc}} \frac{M_{dec}}{M_{dec}^{iso}} \quad (4.14)$$

#### 4.1.4 Modification of $v_2$

It is expected that isolation cut will also modify the value of trigger photon's  $v_2$ . Isolation increases the probability of sampling Compton scattering photons, which in principle do not flow with the medium and therefore have zero  $v_2$ . Measurement of isolated photon's  $v_2$  have been started by the time of the writing of this dissertation, and initial results are obtained. There are indications that reduction of the  $v_2$  values indeed takes place. The isolated photon's  $v_2$  measurement have not been finalized such that no definite value is available to be used for our analysis.

To take into account the reduction of  $v_2$ , we perform a test study where three different values of  $v_2$  are used. The three scenari include an unmodified photon  $v_2$ , a zero  $v_2$ , which is the 'expected' value for isolated photons, and a negative  $v_2$ , which gives the conservative estimate of the reduction. These different choices are to be applied to the inclusive isolated photons. This study is going to be discussed in Chapter 7 where we present the results of our isolated  $\gamma_{dir} - h$  measurements. The test study will provide a rough estimate of the additional systematic uncertainties that is introduced by this changes of  $v_2$ . The discussion on the sources of systematic uncertainties in the  $\gamma_{dir} - h$  yields will also be given in Chapter 7.

## 4.2 Data selection

Quality assurance is applied to the data prior to the analysis procedure, to ensure that the final result is reliable. Bad quality data are those that have the potential of giving false information, and it can happen because of many reasons. In this section, we describe the selection rules for an event as well as for individual photon and charged hadron signals.

### 4.2.1 Event selection

The first general cut in event selection is that the vertex position should be within  $-30 < z < 30$  cm. Since the current PHENIX detector have a narrow rapidity acceptance, events with  $z$ -vertex too far from the center point would produce many tracks not recorded by the detectors. And second is that the centrality of the events should be within 0 – 92%. Events that are selected based on those two rules are called as the Minimum Bias events.

A single run of data taking is defined by the action of Start and Stop from the Data Acquisition software (the DAQ) and it will record multiple events into a single bundle. Further data selection are applied to each of such bundle. It is done by looking at the comparison of the Acceptance Function of each run (Eq. 3.1) to the averaged Acceptance Function of the overall runs. The shape of the Acceptance Function could represent the performance of the detector, if its shape is off when compared to the average, there are probably some issues when that particular run was recorded, and it will be removed.

An example of the mix background from a bad run is shown in Fig. 4.5. The deviation of the per-run mix background from the average can be represented by the  $\chi^2$  factor between the two shape. The bad runs are selected as those with  $\chi^2 > 3$ . But some good runs can also gives high  $\chi^2$  because of large statistic, therefore

further check is also performed by eye. About 7% out of the total available runs were removed. After all cuts applied, 3.9 and 6.6 billion events remains for the Run 7 and Run 10 respectively.

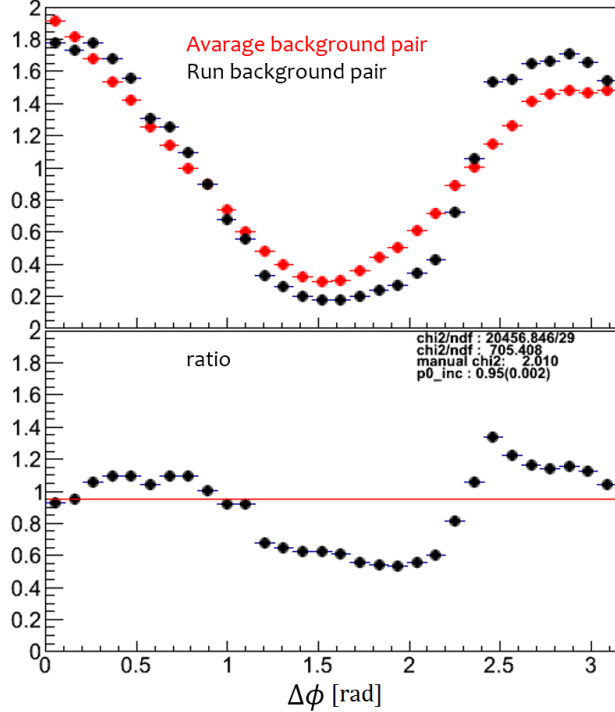


Figure 4.5: The mix background of a bad run compared to the average, and their ratio.

#### 4.2.2 Photon Selection

For the photons, we set a minimum  $p_T$  of 5 GeV to access the hard scattering physics that we are after. The photons are selected based the following:  $\chi^2$  cut, PC3/EMCal matching, hot/dead tower removal, and detector edge cluster removal.

In the EMCal, a particle signal is defined by hits on several towers, called as a cluster, with the strongest signal on the center. Signal of a photon is identified by

comparing its cluster with the known electromagnetic cluster shape. The comparison is quantified by  $\chi^2$  and the cut is set at  $\chi^2 < 3$ . This cut removes signals that might come from neutral hadron which will show a different cluster shape. Electron signals are already removed by RICH matching.

The PC3/EMCal matching veto a cluster when it's position is found to be close to that of a PC3 signal. In particular the distance of  $\phi > 0.01$  rad and  $z > 5$  cm are used as the cut. This cut removes the possibility that energy of a cluster is contaminated by a nearby passing charge particle.

Throughout the run of the experiment, some towers might lost their function. Either they are not responding (dead) or they are continuously responding (hot). The hot towers are identified by looking at the overall distribution of energy registered in every towers. The hot towers are defined to be the towers that register number of hits higher than  $5\sigma$  above the mean, see Fig. 4.6 for example. Clusters that includes hits from these towers are vetoed. Clusters that are located at the edge of the detector are also removed. This is due to the possibility of some photon's energy are gone outside the detector coverage.

#### 4.2.3 Hadron Selection

A charged track in the spectrometer is given a quality value based on the reading on DC and PC1. Tracks of the best qualities are when there are hits on all the X, UV and PC1 modules. When the hits on UV and PC1 are unique, the track is given the quality 63. When there are multiple hits on PC1, but the best track location can still be determined using UV hits, the track is given the quality 31. Only tracks that have either of these two qualities are selected.

Further cut is RICH track veto to remove electron signals. The RICH veto is effective in the  $p_T$  region below 5 GeV. The charged hadrons that we will be using

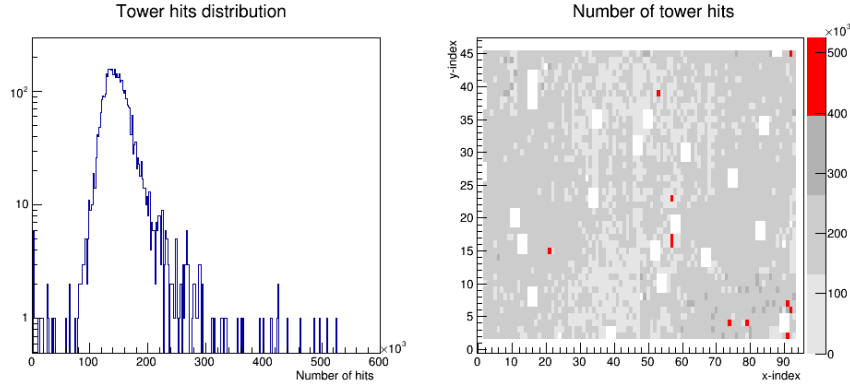


Figure 4.6: Example of finding the dead and hot towers. On the left panel, few hot towers register number of hits far right end of the distribution. On the right panel, the dead towers are colored white and the hot towers are colored red.

are ranged from 0.5 to 10 GeV. At the high  $p_T$  region, many contamination came from tracks that are produced at the edge of the detector, mostly by photon conversion or by hadronic decay. Because the DC algorithm always assume that tracks are originated from the collision vertex, those contaminating tracks are registered with higher momentum than what they should be.

The sources of this false high  $p_T$  tracks are low  $p_T$  particles that are essentially abundant, while the spectra of the true  $p_T$  charges themselves fall very rapidly. Even though only very small fraction of low  $p_T$  charges are falsely reconstructed, their contribution become significant when compared to the high  $p_T$  spectra. That gives the picture that the problem of high  $p_T$  charge background is a serious issue.

Track matching between DC+PC1 and PC3 is used to reduce the contribution of such false high momentum tracks. The matching is usually done by taking the signalized distance between the projected position of DC+PC1 track on the PC3,

with the nearest PC3 hit, in  $z$  and  $\phi$ . The signalized distance is defined as

$$\sigma\phi = \frac{d\phi - \langle d\phi \rangle}{\sigma_{d\phi}}, \quad \sigma z = \frac{dz - \langle dz \rangle}{\sigma_z} \quad (4.15)$$

$d\phi$  and  $dz$  are the distances between DC+PC1 and PC3 projection in  $\phi$  and  $z$ .  $\langle d\phi \rangle$  and  $\sigma_{d\phi}$  ( $\langle dz \rangle$  and  $\sigma_{dz}$ ) are the mean and sigma of the  $d\phi$  ( $dz$ ) distribution of all tracks, for certain  $z$ ,  $\phi$  and  $p_T$ . The matching is performed by applying  $\sqrt{\sigma\phi^2 + \sigma z^2} < 2.0$  as a cut.

Cutting on the signalized distance still left considerable amount of the background at high  $p_T$ . However, it was shown that the contamination for the case of conditional tracks (tracks that are triggered by a photon or  $\pi^0$ ) is smaller when compared to contamination in the case of non-triggered tracks. In Fig. 4.7, the ratio of charge spectra of signalized cut  $3\sigma$  and  $2\sigma$  is plotted for the inclusive and the ones that require photon/ $\pi^0$  trigger. In the case of the inclusive tracks, one can see the ratio is increasing at high  $p_T$ , showing large background contamination. For the conditional spectra, the increment is slower. This shows that in a photon - hadron pair correlations measurement the high  $p_T$  charge background is not as severe as in single particle measurements.

### 4.3 Energy Re-Calibration of the EMCAL Detector

The EMCAL towers are calibrated to take into account the fluctuation of the gain when responding to photon hits. The energy calibration is performed using a standard value of  $\pi^0$ . A global calibration has been performed such that the measurement of  $\pi^0$  from the peak position of photon pairs invariant mass produces the standard value. However, for Run 10 data set, the run by run evaluation of the  $\pi^0$  shows some level of fluctuation. We have performed a further recalibration where

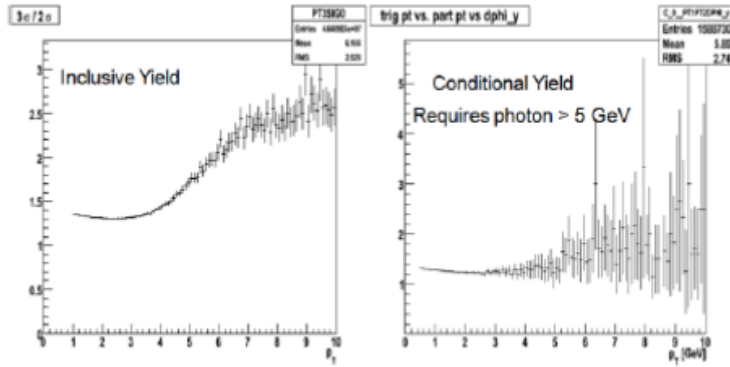


Figure 4.7: The ratio of the charge particle spectra of when  $3\sigma$  cut is applied with when  $2\sigma$  cut is applied. The left panel is for inclusive charge tracks, right panel is for the conditional charge tracks [33].

the correction constants are obtained separately for different runs, as well for different sectors.

In our recalibration procedure,  $\pi^0$  invariant mass is measured separately for each runs and for each sector. Low  $\pi^0 p_T$  is selected because that is where we see the most fluctuation. One example where the measurement is evaluated on sector 0 and 1 of the PbSc detector, with  $\pi^0 p_T$  ranges of 1.0 to 2.0 GeV, as function Run number, is shown in Fig. 4.8. One can see that there is some level of fluctuation of the  $\pi^0$  invariant mass peak position. Recalibration constants are obtained for each Run numbers and for each sectors that will make the the peak positions agrees to a standard value. The procedures are repeated for all the other sectors and different recalibration constants are obtained.

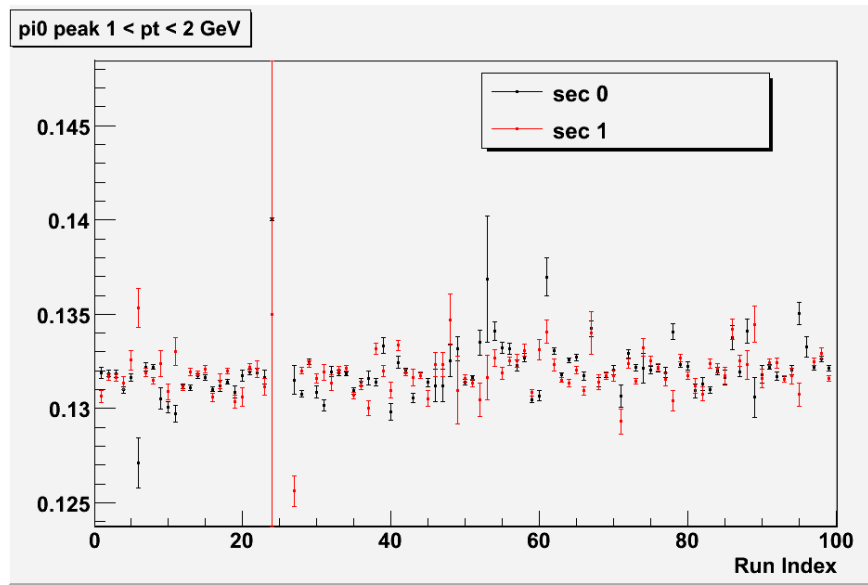


Figure 4.8: The peak position of the  $\pi^0$  mass measured in the range of  $1.0 < p_T^{\pi^0} < 2.0$ , on two different sector, on for each Run number of the Au+Au Run 10 data, before recalibration.

## 5 Simulation Study

We have performed Monte Carlo simulations with the goal of testing the subtraction method as described in Chapter 3. There are earlier simulation studies regarding the decay mapping method from  $\pi^0 - h$  to  $\gamma_{\text{dec}} - h$  pairs in a simulated p+p collision that was done in separate analysis [33]. In this dissertation we are doing further investigation upon simulated Au+Au events, also with the application of isolation cut. From the previous study, we have extracted some level of fluctuation that is produced by the decay mapping method. In this study we examine if the same measurement in Au+Au and with isolation cut would add additional uncertainties or not.

The Au+Au events are simulated using the Monte Carlo software HIJING [22], we converted the list of HIJING particles output into the similar type that we have for the real data. It is a manual conversion and does not involve PISA nor PISAnDST. Energy smearing is also applied manually based on the analytic form in Eq. 2.6 and Eq. 2.5. Therefore, we can use the same software module that is used in real data analysis.

In the simulation, we know exactly the identity of the photons. The fluctuation is examined by comparing the  $\gamma_{\text{dec}} - h$  and  $\gamma_{\text{dir}} - h$  correlations that are derived from the inclusive photons following the procedure in Chapter 3, (we refer to as  $Y^{der}$ ), with the correlations that are obtained directly using the known photon's identity (we refer to as  $Y^{true}$ ). The comparison is quantified as the percent error

$$\% - \text{error} = \frac{Y^{der} - Y^{true}}{Y^{true}} \quad (5.1)$$

The simulation study is concentrated on the photons with  $p_T$  of  $7 - 9$  GeV, we will also show results in the range  $9 - 12$  GeV but there might be large reduction on the statistics. Full study on the wider  $p_T$  range can't be done because of limitation on disk space, which was needed to store more statistics.

### 5.1 Statistical method

Fig. 5.1 shows the  $\gamma_{\text{dec}} - h$  pair correlation functions calculated both from the known real decay photons and derived through  $\pi^0$  reconstruction, in the simulated  $20 - 40\%$  events. The correlation functions are shown for ten combinations of two trigger  $p_T$  and five associate particle  $p_T$ . The combinatoric backgrounds are also shown, and they are flat because in HIJING the flow effect is not available. The background level is obtained from ZYAM method. The correlations function is a direct measurement in the experiment, because it basically is the counts of particle pairs (with the acceptance correction), without any assumption on the background. The jet functions, that are obtained by subtracting the flat background, are shown in Fig. 5.2.

The  $\% - \text{error}$  that represents the fluctuation derived from the true of the correlations function, the flat function and the jet function are shown in Fig. 5.3, as function of  $z_T = \langle p_{T,\text{assoc}} \rangle / \langle p_{T,\text{trig}} \rangle$ , for all  $p_{T,\text{trig}} \times p_{T,\text{assoc}}$  combinations. The yields that are included in the  $\% - \text{error}$  are the integrated  $\Delta\phi$  distribution over the region  $2\pi/3 < \Delta\phi < \pi$ .

One can see that in general the fluctuation of the derived correlation function as well as the flat background is very small, almost 0. The fluctuation of the jet functions however seems to be magnified. The reason for that is the error in the jet function is a product of propagation from the correlation function and the flat

background. Second reason is, that the value of the jet function is close to zero, therefore Eq. 5.1 can easily blow up.

Overall, the fluctuation of the  $\gamma_{\text{dec}} - h$  correlations function is taken to be  $\sim 1\%$ , and the jet function is  $\sim 2\%$ . The fluctuation is increasing in two kinds of cases. First is when the background level is high, which happens at the more central events and at lower  $p_T$  bins. Second is when there is less statistics, which happens at high  $p_T$  bins.

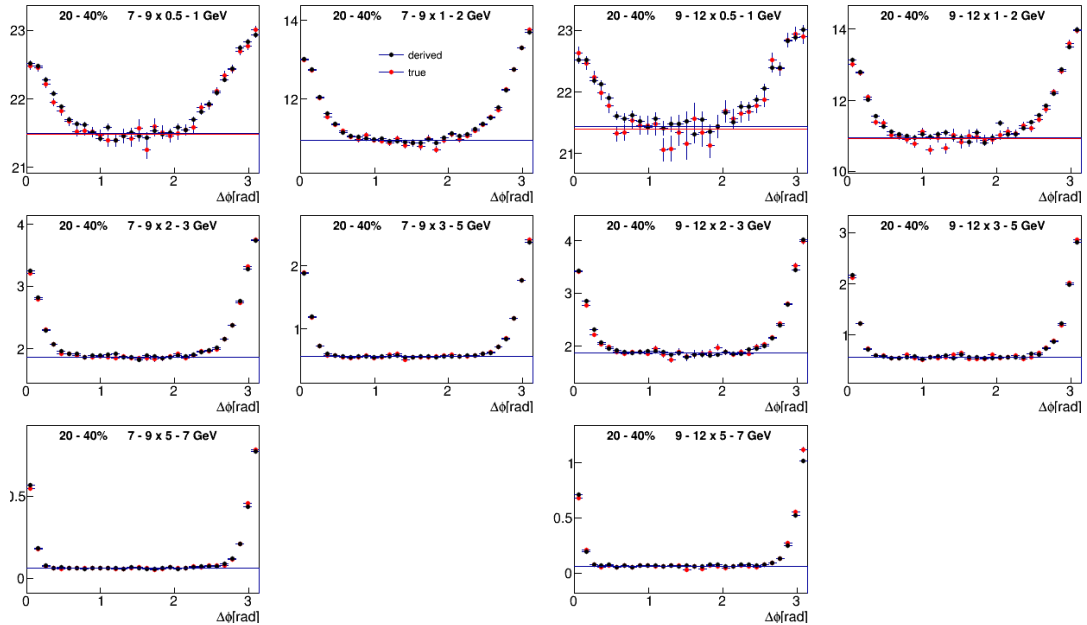


Figure 5.1: The  $\gamma_{\text{dec}} - h$  pair correlations function of the true and derived decay photons, for the combinations of two trigger  $p_T$  bins and five associate  $p_T$  bins.

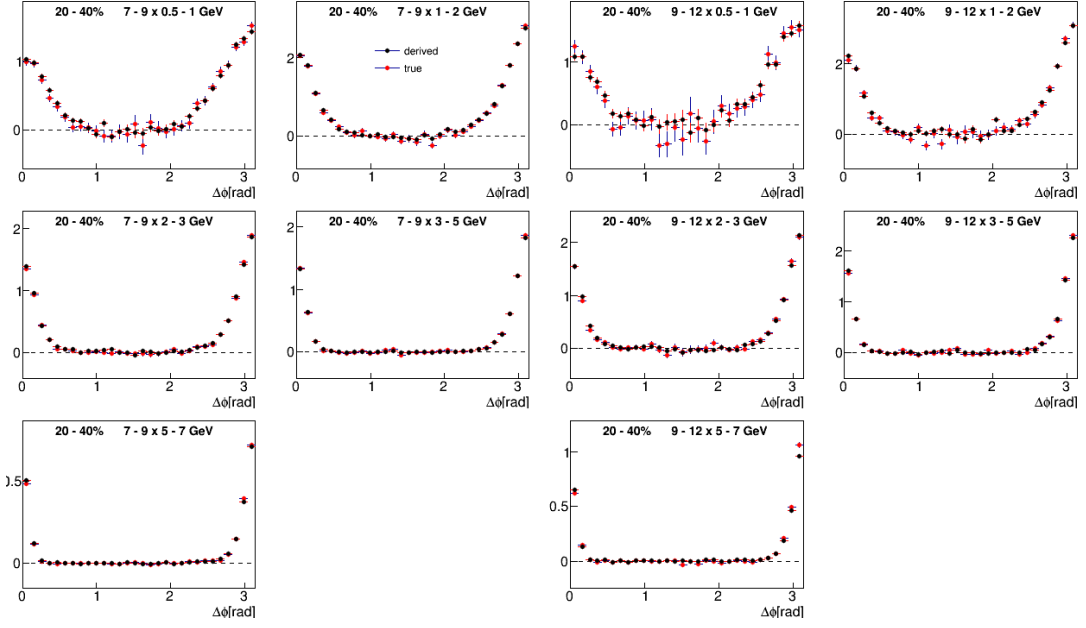


Figure 5.2: The  $\gamma_{\text{dec}} - h$  pair jet functions of the true and derived decay photons.

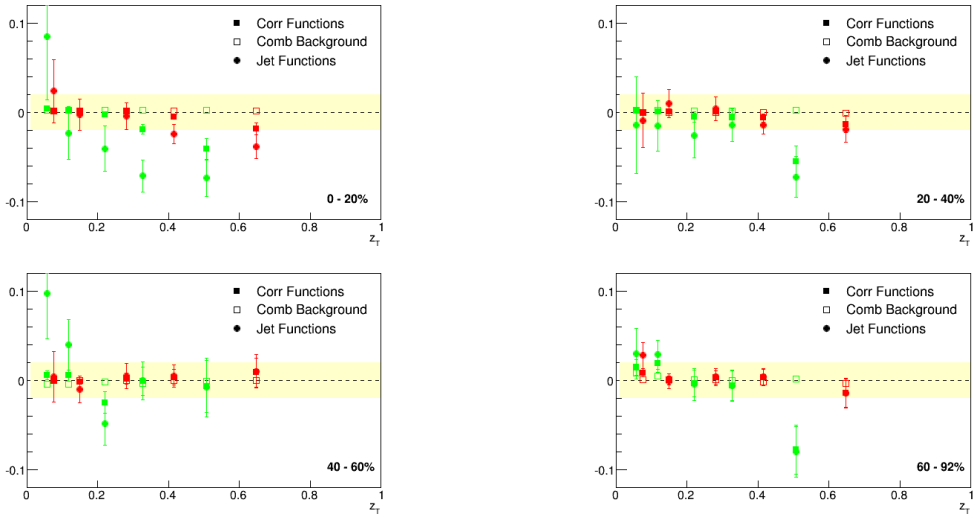


Figure 5.3: The  $\% - \text{error}$  of the derived from the true  $\gamma_{\text{dec}} - h$  pair correlation functions, background, and jet functions, in terms of  $z_T$ , in all centralities. The yellow band indicates  $2\%$  ranges.

Next, we would like to examine the fluctuation on the  $\gamma_{\text{dir}} - h$  jet functions.

The jet functions obtained from the statistical subtraction and from true HIJING direct photons, in the 20 – 40% events, are shown in Fig. 5.4. The % – error of the two are shown in Fig. 5.5 for all centralities. From the comparisons of the jet functions, we can see the general agreement in shape of the two.

From the % – error values, one can see that the fluctuation of the  $\gamma_{\text{dir}} - h$  jet functions are magnified to an order higher than of the  $\gamma_{\text{dec}} - h$  jet functions. The fluctuation is about 20% for the central events and half of it in the peripheral events, this shows that the background level error is propagated significantly to the final  $\gamma_{\text{dir}} - h$  pair calculation. In the real data analysis, the total systematic uncertainty of the  $\gamma_{\text{dir}} - h$  yields is on the order of 20%, comparable to the fluctuation in this simulation study.

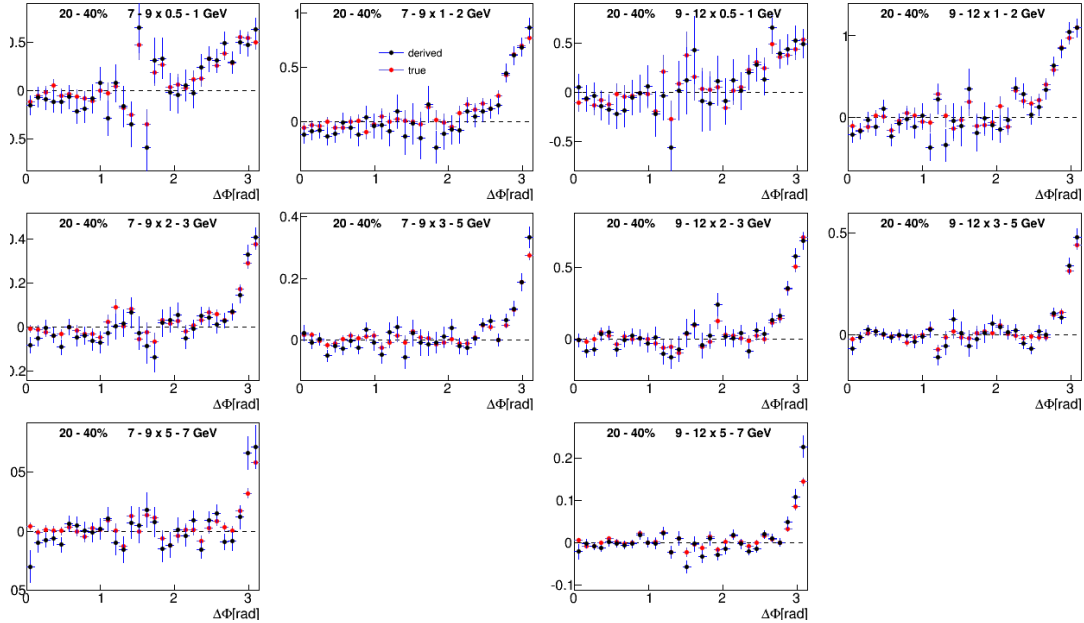


Figure 5.4: The  $\gamma_{\text{dir}} - h$  pair jet functions of true and derived direct photons.

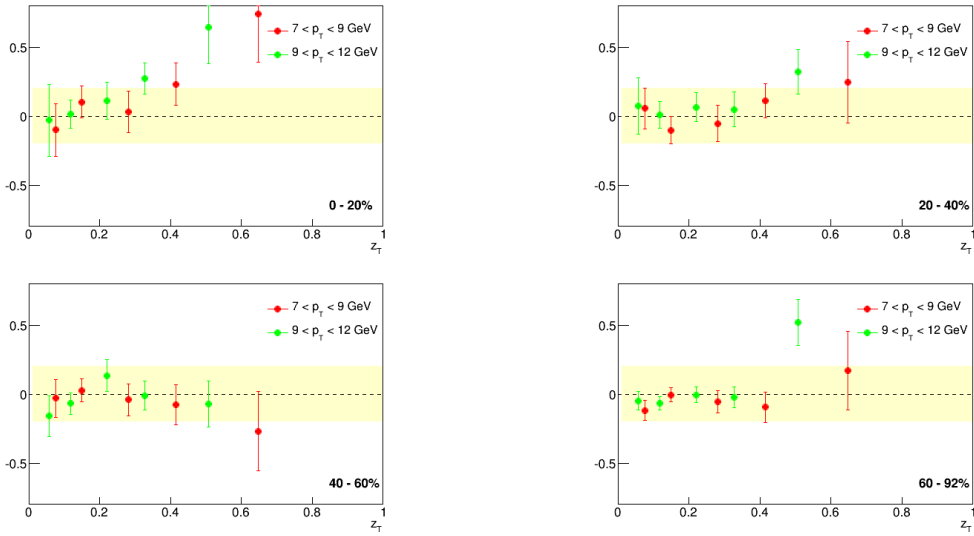


Figure 5.5: The percent difference of the derived with the true  $\gamma_{\text{dir}} - h$  pair jet functions, in terms of  $z_T$  and in all centralities. The yellow band indicates a 20% ranges.

## 5.2 Isolation cut method

Next, we examine the comparisons and  $\% - \text{error}$  when isolation cut is applied. As a note, the isolation cut parameters used in the simulation are kind of arbitrary, and would not optimize the final uncertainties. The derived and true comparisons of the correlation functions in the  $20 - 40\%$  events are shown in Fig. 5.6, and the comparisons of the jet functions in Fig. 5.7. The  $\% - \text{error}$  from all centralities are shown in Fig. 5.8.

When compared to the statistical method, in general the fluctuations when isolation is applied is a bit larger, although, in overall the fluctuations are within 2%. Main source of the fluctuation is most likely the statistics; the isolation cut approximately removes 50% of the photons. The fluctuation of the  $\gamma_{\text{dec}} - h$  jet functions are now generally exceed the 2% band.

As we understand from the previous section, the jet function fluctuation usually blows up with respect to the fluctuation of the correlation function. In this isolation method, one might expect a larger jet function fluctuation due to an already large correlation function fluctuation. That is not the case, and the explanation for that comes from the fluctuation of the background. For example, one can look at the bin of  $7 - 9 \times 1 - 2$  GeV in  $p_T$  in the  $20 - 40\%$  centrality bin. We can see that both the error for the correlations and background functions are large, but the error on the jet function is not considerably large. It turns out that it's not only the absolute error of the correlations and background that play role in the propagation, but the relative difference between them as well, such that, the fluctuation on the jet function is minimize when the difference of the fluctuation level of the correlations and the background is at the smallest. Just a reminder, everytime we mention 'fluctuation' or 'error' we basically mean the value of 5.1.

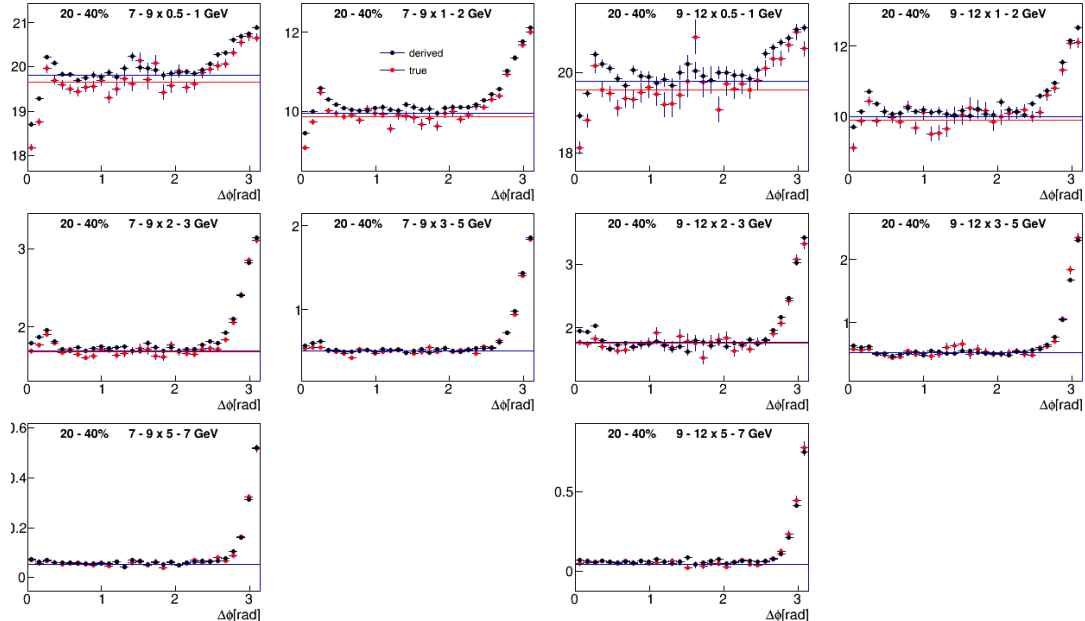


Figure 5.6: The isolated  $\gamma_{\text{dec}} - h$  pair correlations function of true and derived decay photons.

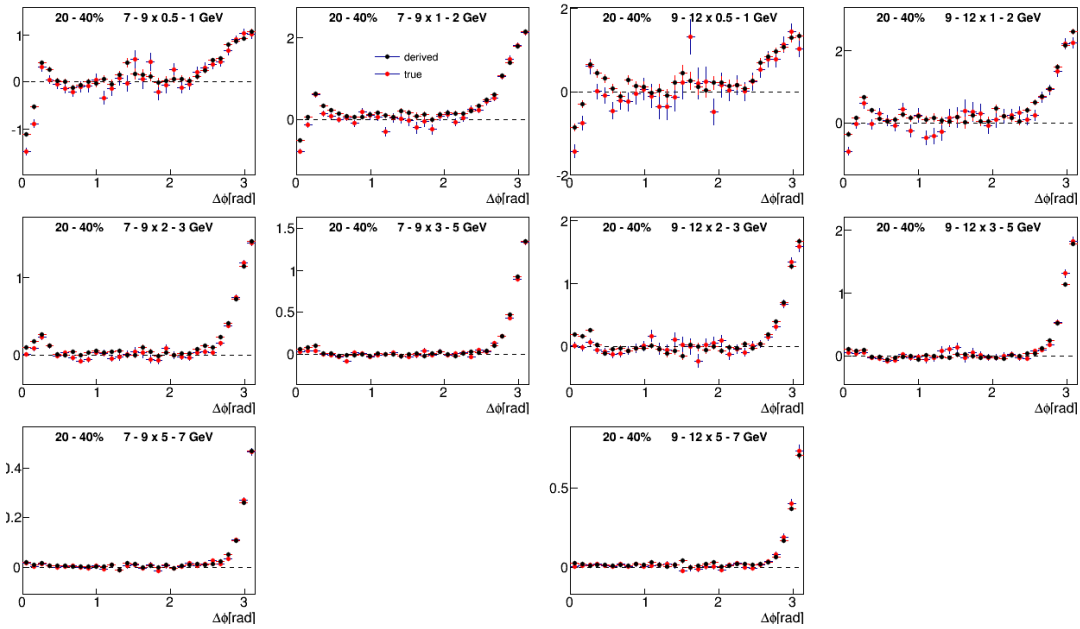


Figure 5.7: The isolated  $\gamma_{\text{dec}} - h$  pair jet functions of true and derived decay photons.

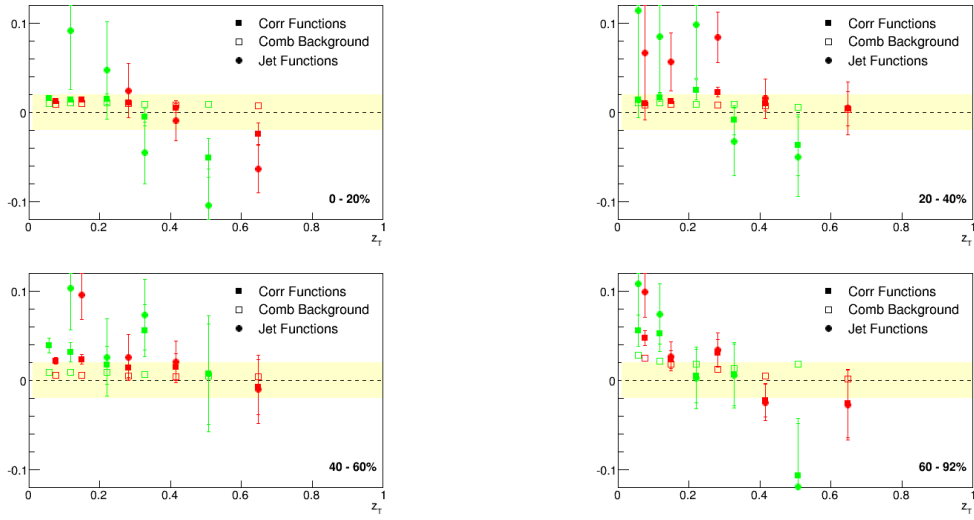


Figure 5.8: The  $\% - \text{error}$  of the derived from the true  $\gamma_{\text{dec}} - h$  pair correlation functions, background, and jet functions, in terms of  $z_T$ , in all centralities. Isolation cut is applied. The yellow band indicates 2% ranges.

The last part of this study is to examine the fluctuation in the isolated  $\gamma_{\text{dir}} - h$  jet function. For the derived isolated  $\gamma_{\text{dir}} - h$  pairs, we first of all need to get the  $R_{\gamma}^{\text{eff}}$ , which we obtain using the  $\rho$  factor defined in Eq. 4.14. We also look at the comparison between the  $\rho$  values obtained from the true and the derived decay photons, and it is shown in Fig. 5.9. They look very much in agreement, especially in the  $p_T$  bin of our interest. One thing to point out is that  $\rho$  are always larger than one, which means that  $R_{\gamma}^{\text{eff}} > R_{\gamma}$ , and according to our assumption, this should improve the measurement of direct photons.

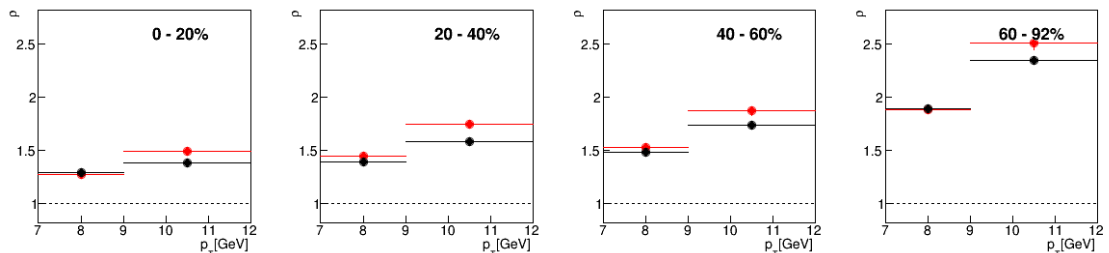


Figure 5.9: The  $\rho$  factor obtained from true and derived decay photons. The 'true' value is shown in red and the 'derived' is shown in black.

In Fig. 5.10 is shown the  $\gamma_{\text{dir}} - h$  pair jet functions with the isolation cut, and the percent differences in Fig. 5.11. The fluctuation on the final isolated  $\gamma_{\text{dir}} - h$  jet functions are comparable to those obtained in the statistical method. This shows that, with the fact that the fluctuation level on the  $\gamma_{\text{dec}} - h$  is large, the increase of  $R_{\gamma}$  contributes in the improvement of the fluctuation.

### 5.3 Conclusions of the Simulation Study

The fluctuations of the  $\gamma_{\text{dec}} - h$  correlation functions obtained from the  $\pi^0 - \gamma_{\text{dec}}$  mapping are within 1%. The fluctuations of the  $\gamma_{\text{dec}} - h$  jet functions are

always larger than the fluctuations of the correlation functions because of the additional uncertainty from the background estimation. We found that the fluctuations of the jet functions goes to 2%. In the case of  $\gamma_{\text{dir}} - h$  jet functions, the fluctuations propagate to the level of 20%.

When isolation cut is applied, we found that the fluctuations of the correlation functions and jet functions of  $\gamma_{\text{dec}} - h$  pairs are larger when isolation cut is not applied; they goes up to the level of 10%. That is caused by the additional uncertainty coming from the modification of the  $\pi^0 - \gamma_{\text{dec}}$  mapping, as well as reduction of the signals. Nevertheless, the fluctuations of the isolated  $\gamma_{\text{dir}} - h$  jet functions did not become larger than the fluctuations when isolation cut is not applied. The main reason for that is that with isolation cut we also increase the signal/background ratio, and that compensates the increase of fluctuations of the  $\gamma_{\text{dec}} - h$  jet functions.

The behaviors of the fluctuations of the  $\gamma_{\text{dec}} - h$  correlation and jet functions and  $\gamma_{\text{dir}} - h$  jet functions, with and without isolation cut, are found to be consistent across four centrality bins. We conclude that the fluctuations in the measurement of the  $\gamma_{\text{dir}} - h$  jet functions with the statistical method and with the application of isolation cut, in all centrality classes, produces a comparable fluctuations of 20%.

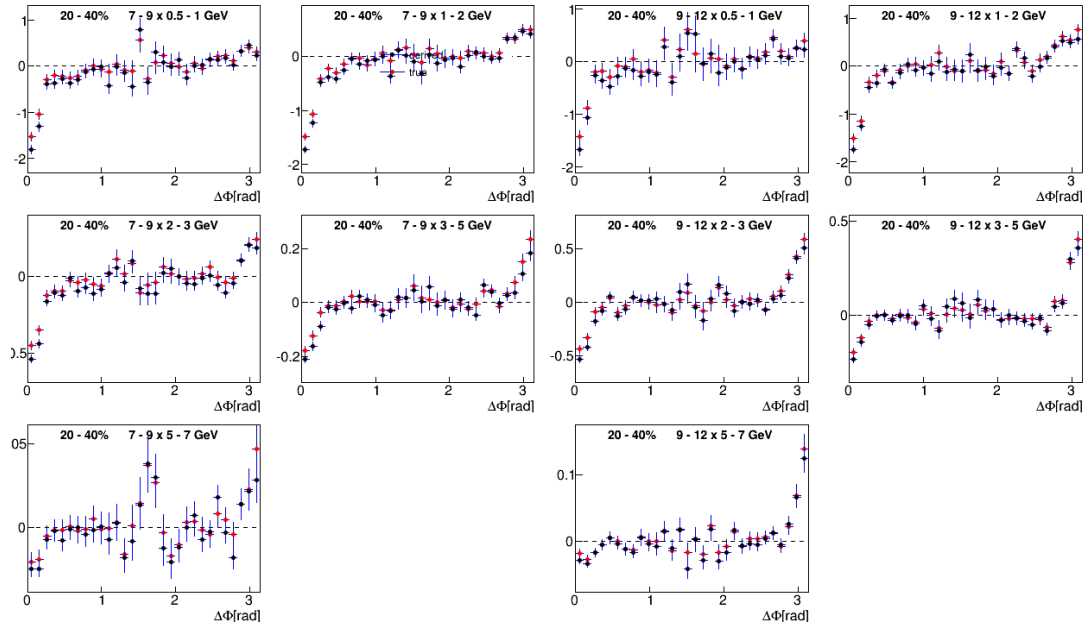


Figure 5.10: The isolated  $\gamma_{\text{dir}} - h$  pair jet functions of true and derived direct photons.

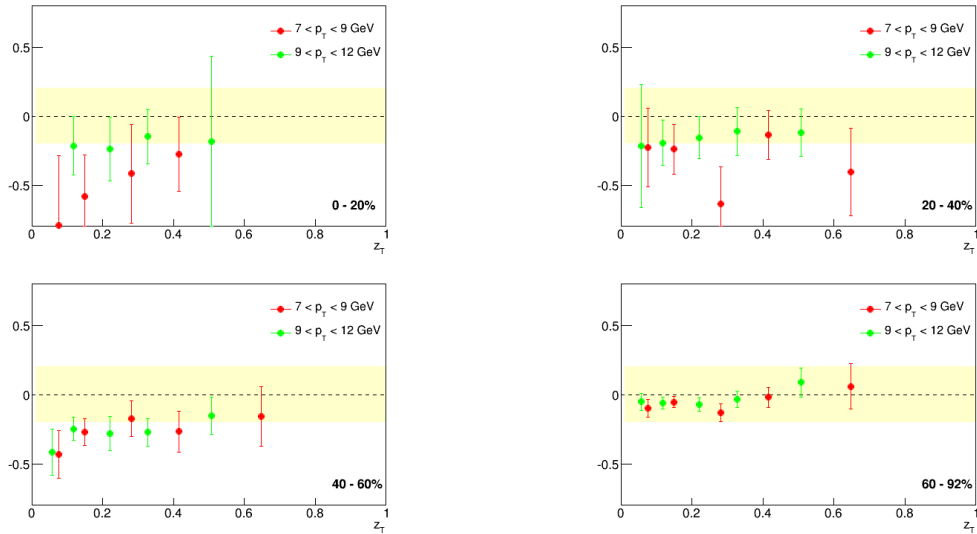


Figure 5.11: The percent difference of the derived with the true isolated  $\gamma_{\text{dir}} - h$  pair jet functions, in terms of  $z_T$  and in all centralities.

## 6 Studies of the modification of the fragmentation function

Earlier measurements of the  $\gamma_{\text{dir}} - h$  correlations have been performed by PHENIX in p+p and Au+Au systems, prior and almost parallel to the one completed in this dissertation work. In this chapter, we will review the results obtained from those measurements and the understandings that were gained regarding the fragmentation function and it's modification in heavy ion collisions.

### 6.1 p+p measurement

Measurement in p+p system has been conducted using the data set collected in 2005 (Run 5) and 2006 (Run 6). The analysis was done in which both data sets are combined. Two steps of additional photon cut were applied; the decay tagging cut and the isolation cut, in order. In the tagging method, we would try to identify the decay photons by measuring the invariant mass of a photon with any other photon in the event. The photons are tagged as decay if the invariant mass of the pair lies within a fixed range centered at the pion mass, and are then removed from the sample. In our analysis, and in most of analysis of Au+Au data, the tagging cut is not used mainly because it is assumed that it will not be effective. The isolation cut that was applied is similar to the one used in our analysis, except for the differences on the choices of the parameters. In the earlier p+p analysis, the parameter used were 0.3, 0.1 and 0.0 for  $R_{\text{cone}}$ ,  $a$  and  $b$  respectively. It was shown that in p+p

collision, the application of the tagging and isolation cut improve the level of the uncertainties on the final results [35].

The integrated away-side ( $\Delta\phi > \pi/2$ ) yield of the  $\gamma_{\text{dir}} - h$  correlations in the p+p system is shown in Fig. 6.1 [16]. The yields shown consist of the compilation from several  $p_T$  combination of the trigger and associated particle, and they are plotted as function of  $x_E$ , where

$$x_E \equiv -\frac{\vec{p}_T^{\text{trig}} \cdot \vec{p}_T^{\text{assoc}}}{|\vec{p}_T^{\text{trig}}|} = -\frac{|p_T^{\text{assoc}}|}{|p_T^{\text{trig}}|} \cos \Delta\phi \equiv z_T \cos \Delta\phi \quad (6.1)$$

The  $x_E$  distribution from the p+p data is interpreted as the fragmentation function of the outgoing partons in the Compton scattering and the annihilation processes, with  $x_E$  playing the role of an approximation to the scaling variable  $x$ . That interpretation is consistent with the fact that we see a scaling behavior, where the  $x_E$  distribution seem to show universal form across different trigger  $p_T$ .

The assumption was tested further using the fragmentation functions measured in  $e^+e^-$  experiment at LEP [37, 38] as references. The fragmentation functions obtained from the LEP experiment were parameterized with exponential function in the region  $0.2 < x < 1.0$ , and the slope of 8.2 and 11.4 were obtained for the quark and gluon respectively [39]. The same parameterization was applied to the p+p results (the dashed line in Fig. 6.1), and the slope found to be 8.2, coincides with the one of the quark fragmentation function [39, 40].

The scaling property of the fragmentation function is not perfect, and it is mostly apparent in the mid-region of the scaling variable ( $0.2 < x < 0.3$ ). An example of the fragmentation function in a wider range, that reaches a much lower  $x$ , is obtained by the TASSO experiment [18]. The fragmentation function is plotted in an alternative variable  $\xi = \ln(1/x)$ , where one can better see the behavior at low  $x$  (high  $\xi$ ), with the PHENIX p+p results overlayed on top of it (see Fig. 6.2). It is

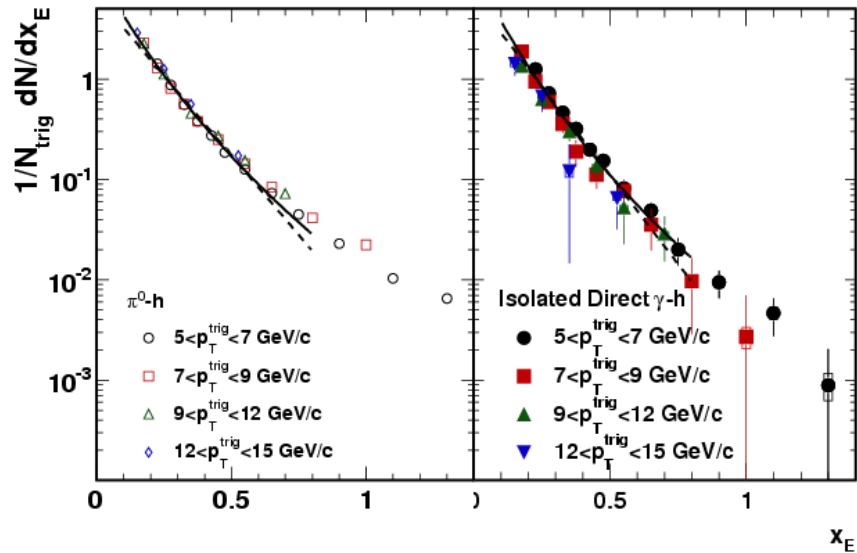


Figure 6.1:  $x_E$  distribution of the away-side yield of  $\pi^0 - h$  (left) and  $\gamma_{\text{dir}} - h$  (right) correlations measured in  $p + p$  [16]. The dashed line is a fit to an exponential function and the solid line is a fit to the Hagedorn function.

clear that a simple exponential parameterization does not apply in the whole range, and that an extention of PHENIX measurement to the low  $x$  region, where scaling violation is prominent, will be interesting.

## 6.2 Au+Au measurement

The first measurement of  $\gamma_{\text{dir}} - h$  correlations in PHENIX was performed on Au+Au data collected in 2004 (Run 4). The most recent results were completed using Run 7 and Run 10 data combined (similar to the work done in this dissertation). In the latest Run 7 and Run 10 analysis an alternative method were adopted, where the pairs are binned directly in  $z_T$ , instead of a separate  $p_T$  binnings of the trigger and associate particles. The disadvantage of the traditional method

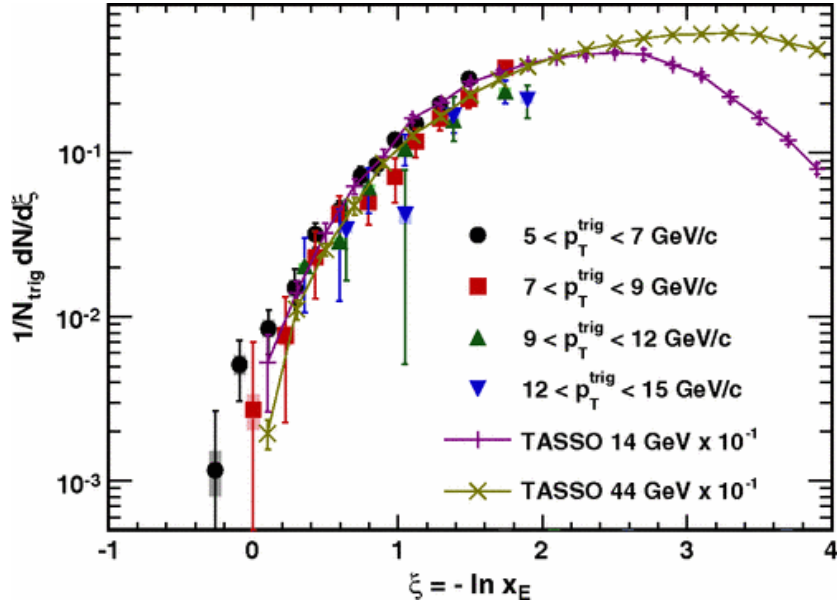


Figure 6.2:  $\xi$  distribution for isolated direct photon data in  $p + p$  for all  $p_T$  ranges combined compared to TASSO measurement in  $e^+e^-$  collisions at  $\sqrt{s} = 14$  and  $44$  GeV [16].

(the  $p_T$  binning), is that one has to perform the transformation

$z_T = \langle p_{T,\text{assoc}} \rangle / \langle p_{T,\text{trig}} \rangle$ , which results in overlapping  $z_T$  values and are inherently coarser. In this dissertation, the newer  $z_T$  binning method was not used.

In Au+Au measurement, the away-side yield is interpreted as a modified fragmentation function. The modification of the fragmentation function is quantified by the  $I_{AA}$  (Eq. 1.5). Fig. 6.3 [17] shows the  $\xi$  distribution of the away-side yield in  $p+p$  and in Au+Au, and the ratio of the two (the  $I_{AA}$ ). In those cases, the  $\xi$  variable is approximated by  $\xi = \ln(1/z_T)$ . The Au+Au results comprise of events with centrality ranging from 0 to 40%. It was found that the measurements in the peripheral bins do not have enough statistical significance such that they don't provide definite conclusions.

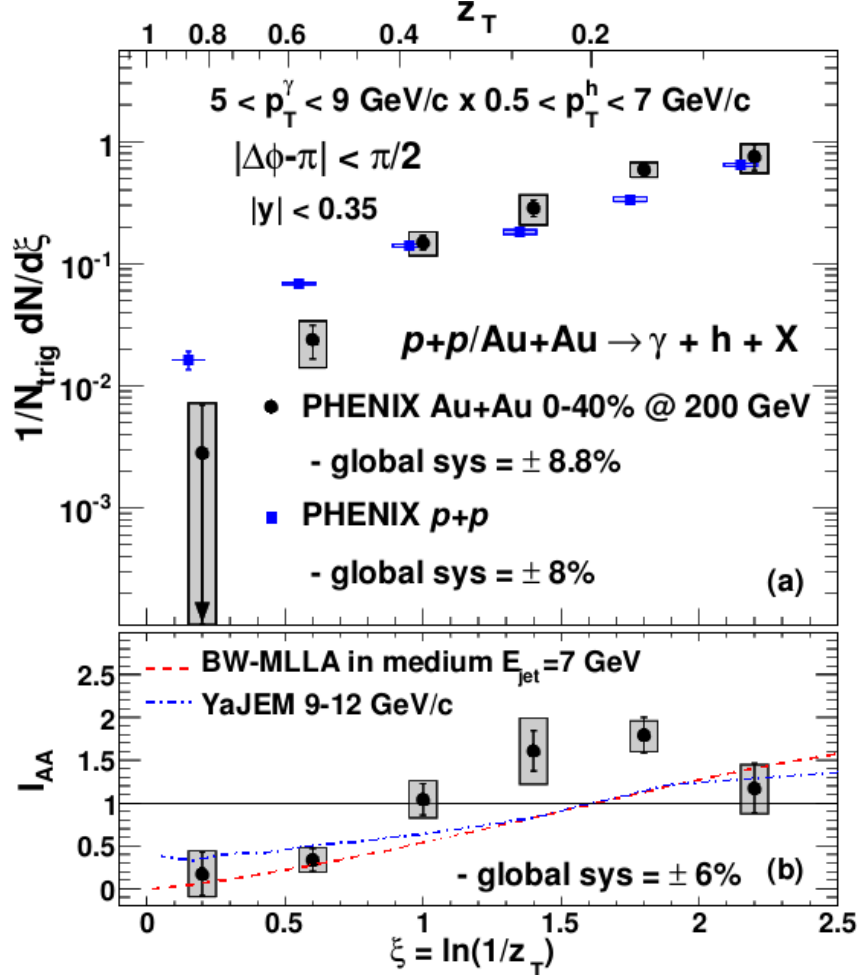


Figure 6.3:  $\xi$  distribution of the away-side yield of  $\gamma_{\text{dir}} - h$  correlations measured in  $p+p$  and in  $\text{Au+Au}$  (top), and the ratio of the two (bottom) [17]. The corresponding  $z_T$  scale is also shown on the top axis.

The  $I_{AA}$  plot in Fig. 6.3 shows that indeed in  $\text{Au+Au}$  the fragmentation function is modified. The interesting results is that the modification is not constant at all  $\xi$ . The fragmentation function is suppressed at low  $\xi$  (high  $z_T$ ) and is enhanced at high  $\xi$  (low  $z_T$ ). This behavior is consistent with the picture where high  $p_T$  jet particles lost energy whilst traveling through the medium, and that the energy loss is redistributed such that production of low  $p_T$  particles is increased.

That idea is incorporated in two theoretical models shown as the dashed and solid line in Fig. 6.3, where the predictions clearly show the suppression and enhancement in two different  $\xi$  regions.

The two model results shown in Fig. 6.3 are YaJEM [14] and BW-MLLA [41]. We have mention in Chapter 1 that YaJEM model implemented the modified parton shower approach, and results in the enhancement prediction. The second prediction comes from the BW-MLLA model [41]. This model is similar to YaJEM in that it follows the modification of parton shower by the medium. But in BW model, the medium effect came in as the factor  $f_{\text{med}}$  that increases the parton splitting probability.

It is also of interest to study the modification as function of the medium density, which is obtained by measuring the  $I_{AA}$  on different centrality bins. A result from PHENIX has been obtained, as shown in Fig. 6.4. This measurement is performed over the smaller Run 4 Au+Au data set. This measurement extends to the mid-peripheral bin, with decent uncertainty level at the most central case but get worse on the other bins. The importance of this result is that it shows the consistency between  $\pi^0 R_{AA}$  and  $\gamma_{\text{dir}} - h I_{AA}$ , to some degree of uncertainty. That shows that both measurements are accessing the same geometry of the medium, which makes sense since the photon triggers are modified,  $\gamma_{\text{dir}} - h I_{AA}$  is an approximate of single hadron  $R_{AA}$ .

In this dissertation, we perform similar measurements that produce Fig. 6.1 and Fig. 6.4, and contribute to Fig. 6.3. We perform the measurements in four centrality bins, and apply the isolation cut. The goal is to get better precision especially in the peripheral cases, that will allow us to study the medium dependence of the modification of the fragmentation function. The results obtained in this dissertation project are presented in the next chapter.

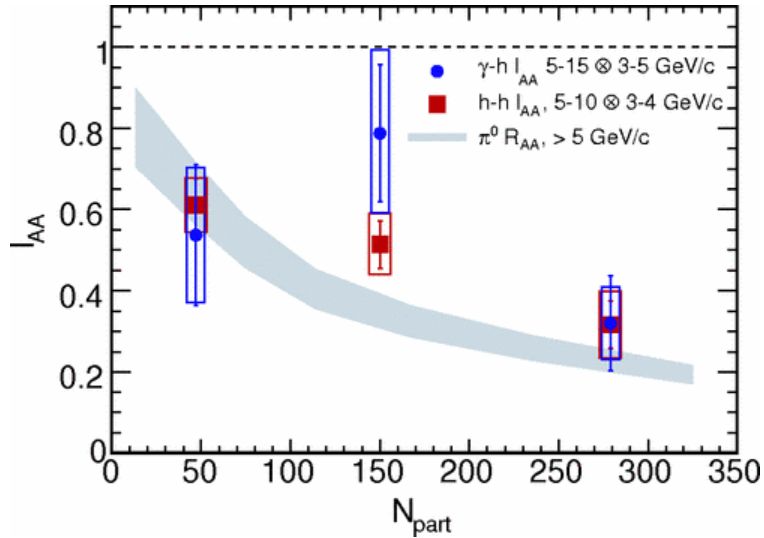


Figure 6.4: The averaged  $I_{AA}$  as function of centrality [40]. The same measurement with improvement is obtained and will be discussed in the next Chapter.

## 7 Results And Discussions

In this dissertation, the analysis is conducted on the Au+Au data set of Run 7 and Run 10, which as indicated previously, are of similar size in terms of numbers of total events available. The measurements of the  $\gamma_{\text{dir}} - h$  pair correlations are performed in four classes of centralities; 0 – 20%, 20 – 40%, 40 – 60% and 60 – 92%. The traditional  $p_T$  binning of the trigger and the associated particles is used. The results from both when isolation is not applied and is applied will be presented. The combination of measurements from two different data sets is done by taking the photon trigger weighted average of the jet functions from each run. Before the combination is performed, comparisons between the jet functions from each run are examined. The jet functions of the  $\gamma_{\text{inc}} - h$  pairs from Run 7 and Run 10, when obtained without applying the isolation cut, show consistency. The full analysis and set of cross checks for the Isolation Cut analysis were not completed for the Run 10 data, Thus Jet Functions with isolation cut applied are not included, in this dissertation. Therefore, on the following, any results that are labelled as "with isolation cut" means it only includes the Run 7 data. This is significant to note, since the improvements to uncertainties highlighted by this first-ever analysis of isolation cuts to the Au+Au environment at RHIC will even be enhanced further in the near future by the addition of an even larger dataset than is currently included as Run7-only. The results in this dissertation are also presented in PHENIX Internal Analysis Note document [44].

## 7.1 $\Delta\phi$ distribution

The jet functions of  $\gamma_{\text{inc}} - h$ ,  $\gamma_{\text{dec}} - h$  (Eq. 3.10) and  $\gamma_{\text{dir}} - h$  pairs (Eq. 3.13) in the most central events are shown in Fig. 7.1. The correlation functions and the combinatoric backgrounds will be shown in the Appendix. At the away-side ( $\Delta\phi = \pi$ ) of the  $\gamma_{\text{dir}} - h$  jet functions we see small peaks, while the near-side ( $\Delta\phi = 0$ ) is consistent with zero. Those features are expected and therefore it is concluded that the subtraction method does give the measurement of direct photons. A non-zero yield on the near side can be attributed to the contribution coming from the fragmentation photons, and it seems to be negligible within the uncertainties. Around the midpoint ( $\Delta\phi = \pi/2$ ) sometimes we see that the jet functions largely fluctuating, and the statistical errors are also larger. That reflects the worst acceptance that resides on the midpoint.

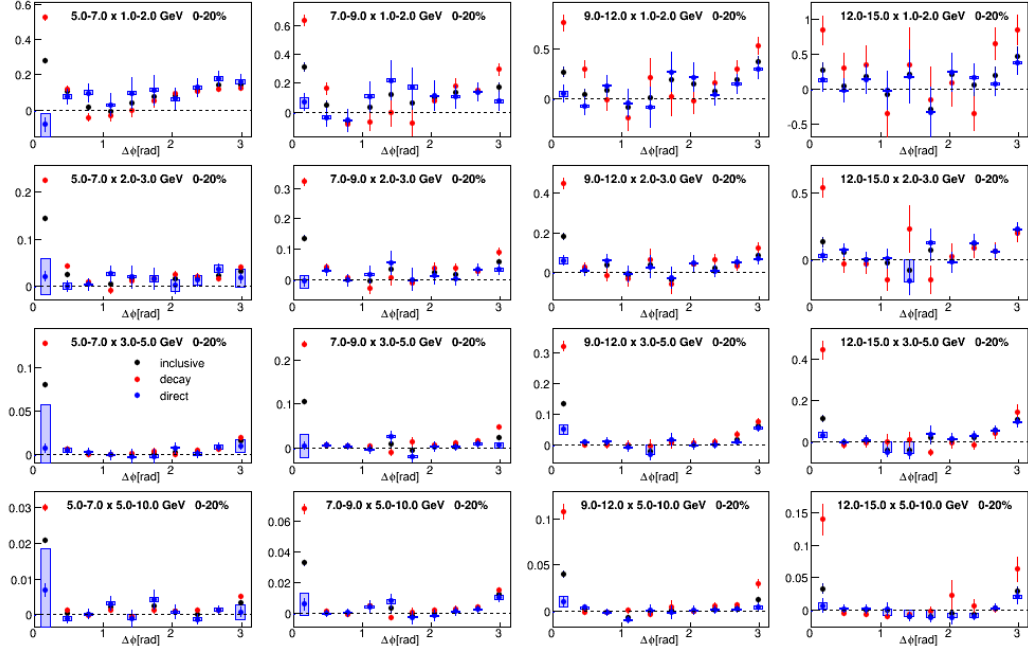


Figure 7.1: The jet functions of  $\gamma_{\text{inc}} - h$ ,  $\gamma_{\text{dec}} - h$  and  $\gamma_{\text{dir}} - h$  pairs 0 – 20% Au+Au.

The propagation of systematic errors to the final  $\gamma_{\text{dir}} - h$  jet functions will be discussed at the later part of this chapter. In Fig. 7.1 the systematic uncertainties on the  $\gamma_{\text{dir}} - h$  jet functions are shown as blue squares. In hindsight, it seems that the statistical errors are growing as we go to higher  $p_T$  bins, while the systematic errors are growing in the opposite direction, which is to the lower  $p_T$  bins. These are understandable since the statistics of high  $p_T$  particles are fastly reduced, while the combinatoric backgrounds mainly consist of low  $p_T$  particles. This illustrates the interplay between the available statistics and the level of the background in determining the total uncertainties.

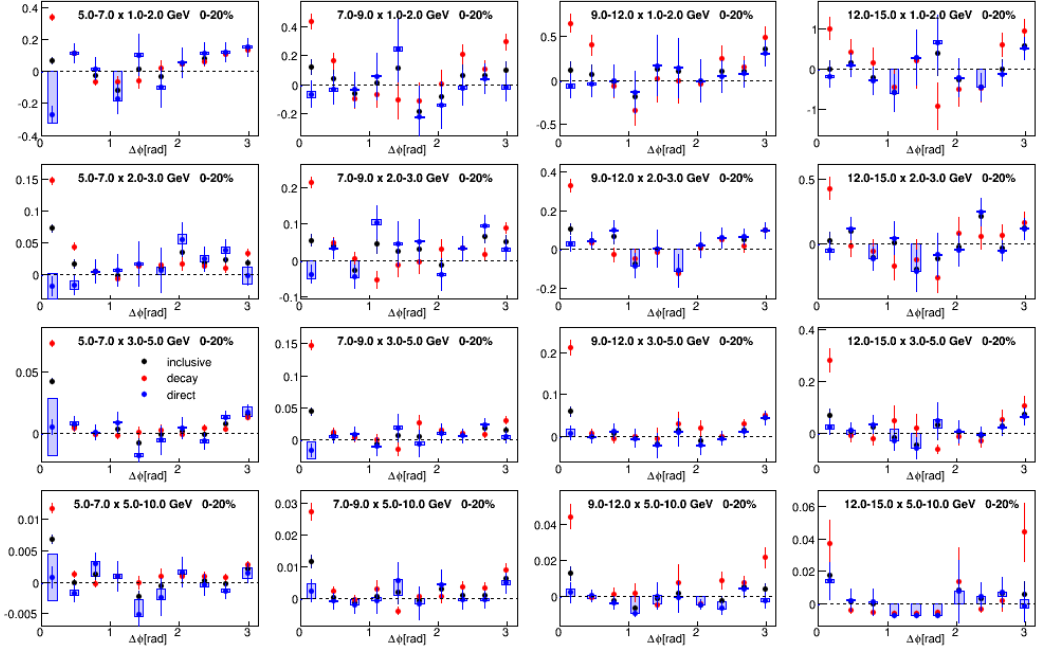


Figure 7.2: The jet functions of  $\gamma_{\text{inc}} - h$ ,  $\gamma_{\text{dec}} - h$  and  $\gamma_{\text{dir}} - h$  pairs 0 – 20% Au+Au with isolation cut applied.

Fig. 7.2 shows the same  $\Delta\phi$  distribution but obtained with isolation cut applied. Many of the same behavior reappear, except that now we found more

negative values on the near-side, when compared to the results without the isolation cut. The negative near-side that occurs when isolation cut is applied is not a physical feature, but instead is caused by the background mixing method.

Within the isolation cut method, the real pairs  $N^{ab}$  are consists of isolated triggers on that event. When forming the mixed pair  $N_{mix}^{ab}$  to get the Acceptance Function (Section 3.1.1), it is computationally inefficient to isolate the trigger based on the cone from all the other particles in the mixed event over the full event sample. Therefore isolation cut is ignored in the mixed events, causing the mixed background on the near-side to always be an overestimate of the Acceptance, and it drives the corrected real pairs down. Because the results in this dissertation focus exclusively on the away-side at angles much larger than the isolation cone sizes ( $R = \Delta\phi < 0.5$ ), this does not affect any of the other derived quantities that follow. A cross check in which a smaller sample of events were processed in a way that the isolation cut was performed on the trigger in mixed events revealed that the shape of the acceptance correction was negligibly different from our method at angles larger than the isolation cone size.

## 7.2 The integrated yields

Fig. 7.3 shows the integrated yield of the away-side jet function in the full region ( $|\pi - \Delta\phi| < \pi/2$ ) for p+p and Au+Au of all centralities. The Au+Au yield obtained from both without and with isolation are applied are presented. The p+p yield in Fig. 7.3 (on both panel) is the same with the one shown in Fig. 6.1 but with less bins of the associate particle  $p_{T\text{S}}$ . The ratio of the yields in Au+Au of all centralities to the p+p yields (the  $I_{AA}$ ) is shown in Fig. 7.4 and in Fig. 7.5 for the without and with isolation cut respectively. As discussed in Chapter 6.2, the measurement  $z_T = \langle p_{T,\text{assoc}} \rangle / \langle p_{T,\text{trig}} \rangle$  values for each point are calculated for each  $p_T$

trigger and  $p_T$  associated bin. A method of direct  $z_T$  binning (for example shown in Figure 6.3 or 7.9) requires some information obtain in the  $p_T$  binned results, therefore direct  $z_T$  binning is a kind of the next step after the  $p_T$  binning. This thesis only includes  $p_T$  binned results and combines information for all contributing  $p_T$  bins by fitting in ranges of  $z_T$ .

The indication of suppression at high  $z_T$  and enhancement at low  $z_T$  are seen in the  $I_{AA}$  (Eq. 1.5) plots, except in the most peripheral events. The error bars on each point of the  $I_{AA}$  are large, such that a constant modification over all  $z_T$  range could be possible alternative to the non-constant behavior. To compare the probability between the two scenarios, constant lines are fitted to the  $I_{AA}$ , over the full ( $0.09 < z_T < 0.80$ ), low ( $0.10 < z_T < 0.28$ ) and high ( $0.28 < z_T < 0.80$ ) ranges of  $z_T$ . The highest point on the  $I_{AA}$  ( $z_T = 1.1$ ) is omitted because the statistical error bar is too large. For the most central case, the fitting procedure gives  $\chi^2/NDf$  values of 1.2/5, 5.32/6, and 22.3/12 for low, high and full ranges respectively. The  $\chi^2/NDf$  is largest when the constant is fitted over the full  $z_T$  range, making it the least probable scenario.

$I_{AA} > 1$  at low  $z_T$  is regarded as indication of the redistribution of energy loss of high  $z_T$  particles to the production of low  $z_T$  particles. This observation favors the theoretical models that are based on modified parton shower, rather than the models of energy absorption (Chapter 1). We would also like to point out, that the same indication is also obtained from the non-constant behavior of the  $I_{AA}$  as function  $z_T$ , shown from the  $\chi^2/NDf$  analysis. In other words, the redistribution of high  $p_T$  particles energy loss is also seen from the relative change of the  $I_{AA}$  over different  $z_T$  ranges, regardless of the absolute value of the  $I_{AA}$  itself.

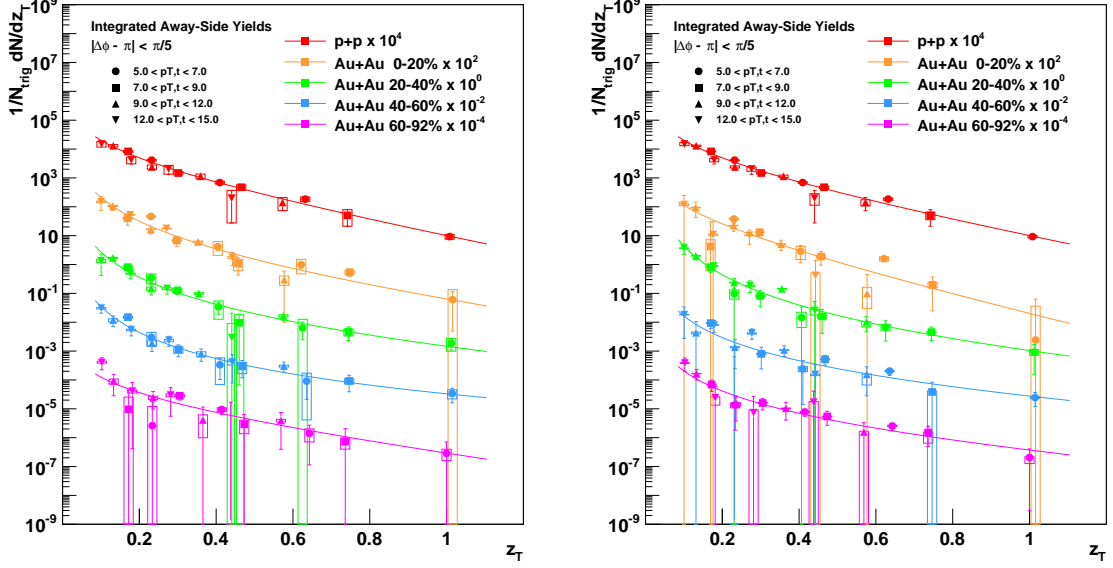


Figure 7.3: The integrated away-side yields of the full region ( $|\Delta\phi - \pi| < \pi/2$ ) in  $p+p$  and in  $\text{Au+Au}$  for all centralities. The  $\text{Au+Au}$  yields on the left panel are obtain without the isolation cut, and on the right panel are obtained with the isolation cut applied. The solid lines are (exponential $\times$ power law) function, used to fit the data plots for illustration.

### 7.3 Systematic uncertainties

Here we will discuss the evaluation of the systematic errors that are included in both the  $\Delta\phi$  distribution and the integrated yields. Sources of the systematic errors are broken down into the uncertainties of inclusive photon measurement, charged hadron measurement,  $v_2$  and the normalization of the combinatoric background, the  $R_\gamma$ , and the decay mapping method. We will discuss the origins of the uncertainties of each sources and how they are determined, and how each of these sources are then propagated to the systematic of the  $\gamma_{\text{dir}} - h$  pair yields.

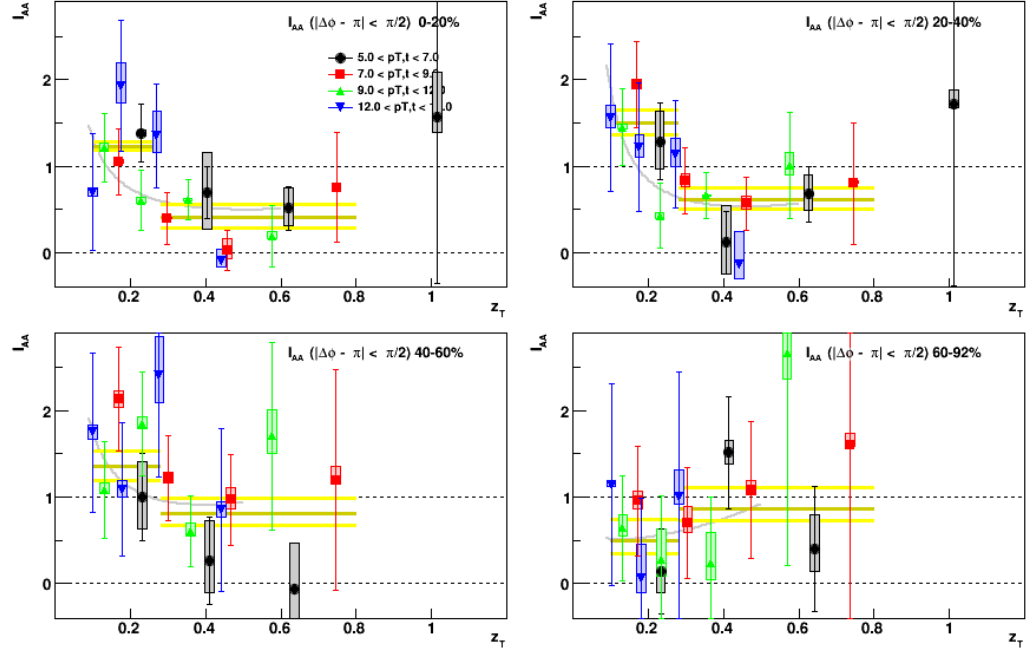


Figure 7.4: The  $I_{AA}$  from each centrality obtained from the integration of the full away-side region ( $|\Delta\phi - \pi| < \pi/2$ ), without isolation cut. Different colors represent different trigger  $p_T$  bins. The solid brown line is a constant function fitted to the  $I_{AA}$ , the solid yellow lines are constant functions fitted to the upper and lower systematic values of the  $I_{AA}$ . A solid grey curve is also shown, it is obtained from the ratio of the fit function used in the away-side yield (Fig.7.3).

### 7.3.1 Sources of the systematic uncertainties

The uncertainty of the inclusive photon measurements is determined previously with the main contribution coming from non-photon background estimation, and a 1% uncertainty was obtained [42]. The 1% error is then propagated conservatively to the final yield of the  $\gamma_{\text{dir}} - h$  correlations.

The charged hadron uncertainties are obtained from the evaluation of the charged hadron efficiency. This study has been conducted over Run 7 data and the

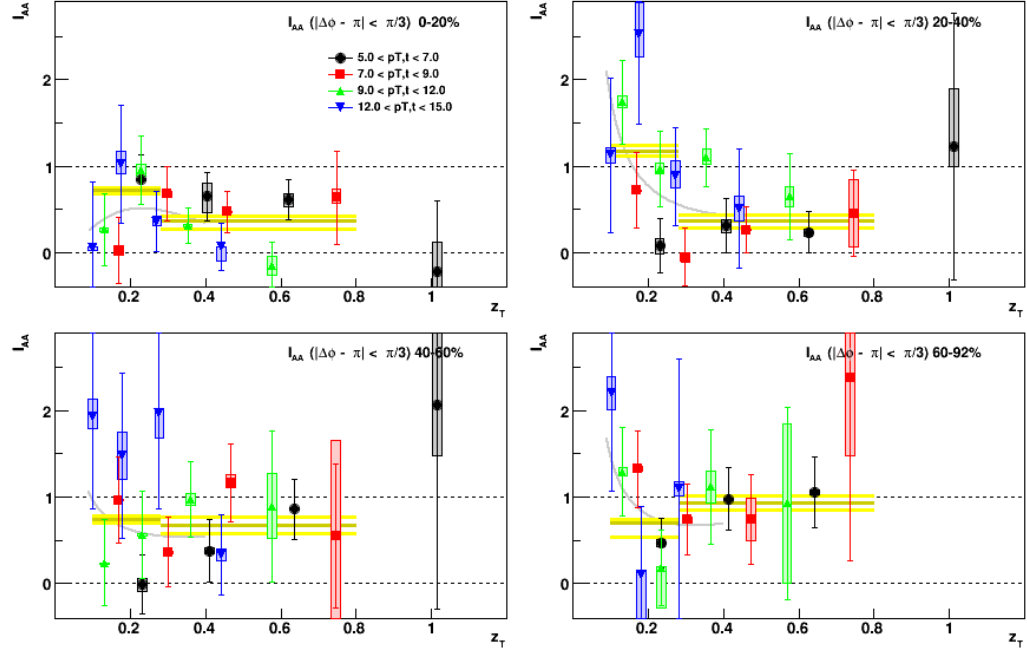


Figure 7.5: The  $I_{AA}$  from each centrality obtained from the integration of the full away-side region ( $|\Delta\phi - \pi| < \pi/3$ ), with the isolation cut applied. Different colors represent different trigger  $p_T$  bins. The solid brown line is a constant function fitted to the  $I_{AA}$ , the solid yellow lines are constant function fitted to the upper and lower systematic values of the  $I_{AA}$ . A solid grey curve is also shown, it is obtained from the ratio of the fit function used in the away-side yield (Fig. 7.3 right). The results are qualitatively similar to those in Fig. 7.4, but with smaller integration region. When compared to the published data [17], the results shown in this figure differ in that they only include  $p_{T,\text{assoc}} > 1$  GeV, not  $p_{T,\text{assoc}} > 0.5$  GeV. The enhancement at low  $z_T$  is not as pronounced (as in Fig. 7.4), which is consistent with the published result [17].

uncertainty of 8.8% was obtained [35]. The charged hadrons appear in the same way on all type of pairs, therefore it appears as global uncertainties in the  $\gamma_{\text{dir}} - h$  pair

yields. The hadronic efficiency as well its uncertainty are expected not to change very much between Run 7 and Run 10. Therefore the global error from the charge hadron measurement of 8.8% also used for the Run 10 and the combined Run 7 + Run 10 analysis. The consistency between Run 7 and Run 10 can be seen from the comparison of the jet functions obtained from the two runs separately.

Determination of the value of  $R_\gamma$  involves the double ratio  $(\gamma_{inc}/\pi^0)/(\pi^0/\gamma_{dec})$ , from which one can see the uncertainty could come from the  $\pi^0$  reconstruction, decay photon extraction, cluster merging and non-linear energy scale [43].

The decay photon extraction error comes from the uncertainties of the mapping method, the  $\pi^0$  cutoff, and the combinatorial error. The main contribution came from the combinatorial error, which is the contribution of fake decay pairs under the peak of  $\pi^0$ 's invariant mass. The combinatorial error is defined as

$\sigma_{\pi_c^0} = (Y_{true} - Y_{meas})/Y_{meas}$ .  $Y_{meas}$  is the measured  $\pi^0$  per-trigger yield and used in the analysis, and it is related to the true and the background per-trigger yield as  $Y_{meas} = (N_{bg}Y_{bg} + N_{sig}Y_{true})/N_{trig}$ . Therefore the combinatorial error is obtained from

$$\sigma_{\pi_c^0} = \frac{1 - Y_{bg}/Y_{meas}}{(N_{sig}/N_{bg})(Y_{bg}/Y_{meas})} \quad (7.1)$$

Usually  $N_{sig}/N_{bg}$  is simply written as  $S/B$ , and it can be calculated from the  $\pi^0$  invariant mass peak.  $Y_{bg}$  is measured from a "side-band" analysis, which basically is the measurement of the yield outside of the  $\pi^0$  peak region.

In this section, we have mentioned the propagation of the uncertainties coming from the inclusive photon and the charged hadron measurements. The propagation of the remaining four sources to the  $\gamma_{dir} - h$  pair yields is discussed in the next subsection.

### 7.3.2 Propagation of the systematic uncertainties

The error propagation could be evaluated analytically, using the error propagation rules, but that produces non-linearity due to the  $(R_\gamma - 1)$  term in the denominator of the subtraction formula. Therefore, the propagation is performed manually, by moving the value of each component in the subtraction formula up and down, according to the uncertainties given by each of the four sources. The direction of the changes from each of the sources is dependent on whether they are correlated or uncorrelated.

The first source of error is the  $v_2$ . Three  $v_2$  are involved in the subtraction formula;  $v_2$  of the inclusive photon, decay photons, charged hadrons. Their propagation depends on whether the uncertainties of the three  $v_2$ s are correlated or not. The main source of  $v_2$  error is the reaction plane resolution, and it is the same in the  $v_2$  measurement of all types. Furthermore, at low  $p_T$ , the majority of photon sample are the decay photons, while at high  $p_T$ , the reaction plane effect dominates. For those reasons, the  $v_2$  errors of the inclusive and decay photons are regarded as correlated. The charged hadrons appear as common factor on the jet function of inclusive and decay photons, therefore the hadron  $v_2$  is completely correlated. Because they are treated as correlated, the inclusive and decay jet functions move up and down on the same direction. Note that for isolation cut results there is an additional uncertainty due to the possible changes of  $v_2$  caused by the isolation cut, mentioned previously in the analysis section and discussed again at the end of this section.

The next source of error is the background normalization, and here we need to consider whether the background in the inclusive and decay photon - hadron pairs are correlated or not. The background normalization of both types of correlation functions are obtained from the same method, it is assumed that should both of the

background level changes, they will shift in the same direction. For that reason the normalization error in the  $\gamma_{\text{dir}} - h$  correlations yield is treated as correlated.

In case of the  $R_\gamma$  error, its propagation to the final  $\gamma_{\text{dir}} - h$  yield is independent, in the way that, we manually move the  $R_\gamma$  values up and down and keeping the other component fixed. Almost similar case is for the last source of uncertainty; the decay error. The error from the decay procedure only effect the decay photon jet functions, and it's manual propagation is done separately from the other sources.

Next we need to consider the correlations of each of these systematics across different  $p_T$  bins. Out of the four sources, the  $R_\gamma$  and the decay mapping errors are considered as correlated, while the background ( $v_2$  and normalization) are considered as uncorrelated. In the plots of the integrated yields, the uncorrelated systematic errors are quadratically summed with the statistical error and presented as the statistical error bar. While the correlated systematic errors are presented as boxes around the data point.

In the  $I_{AA}$  measurements, we need to consider whether the sources of error in p+p and in Au+Au are correlated or not. In p+p, the sources of error are dominated by the  $R_\gamma$  and the decay procedure. There is no  $v_2$  error in p+p and the normalization error can be considered to be statistical and therefore is treated as uncorrelated. The  $R_\gamma$  and the decay error in p+p and in Au+Au are both treated as correlated, therefore the systematic in the  $I_{AA}$  are obtained by raising and lowering the away-side yield in p+p and Au+Au in the same direction.

## 7.4 Physics Discussions

### 7.4.1 High $z_T$ suppression

The values of the  $I_{AA}$  above  $z_T \approx 0.3$  seems to be consistent across all  $p_T$  bins. Therefore, the fit constant that we have mentioned earlier is taken as the average

value of the  $I_{AA}$ , and is used to quantify the suppression. The averaged  $I_{AA}$  are plotted as function of  $N_{part}$ , where its value as function of centrality ranges is known from Glauber Monte Carlo calculation. They are shown in Fig. 7.7, for the case where isolation cut is not applied. This plot is similar to the averaged  $I_{AA}$  in Fig. 6.4 which was measured over the Run 4 data set, although there are differences on the integration range of the yields, as well as the maximum  $p_T$  of the associate hadrons. These two results are compatible to each other and comparison between them can be performed to check for consistencies and improvements. For convenience, we re-introduce the earlier average  $I_{AA}$  vs  $N_{part}$  results from Run 4 in Fig. 7.6.

Within the uncertainties, the measurement of the suppression on the combined data of Run 7 and Run 10 are consistent with the Run 4 results. Regarding the significance, the combined Run 7 and Run 10 give noticeable improvement, based on the smaller error bars, especially in the mid-central 20 – 40% bin ( $N_{part} \approx 150$ ). Improvement from the combined Run 7 and Run 10 data is also shown by a more consistent overall trend of the average  $I_{AA}$  now being qualitatively visible, now more closely following that of the  $\pi^0 R_{AA}$  curve. The version of the average  $I_{AA}$  where isolation cut is applied is shown in Fig. 7.8. We found further improvement of the measurement in that there are significant reduction of the systematic errors in all data points, as well as reduction of the statistical error bar in the two peripheral bins. Presumably the increase of  $R_\gamma$  for the isolated photons leads to better systematics, as expected.

The  $\gamma_{\text{dir}} - h I_{AA}$  seems to be consistent with the  $\pi^0 R_{AA}$ . This can be understood from the fact that the direct photon is emitted from all part of the medium and it is not modified, therefore its production is scaled by  $N_{coll}$  when compared to the production in p+p. That makes for an argument that  $\gamma_{\text{dir}} - h I_{AA}$

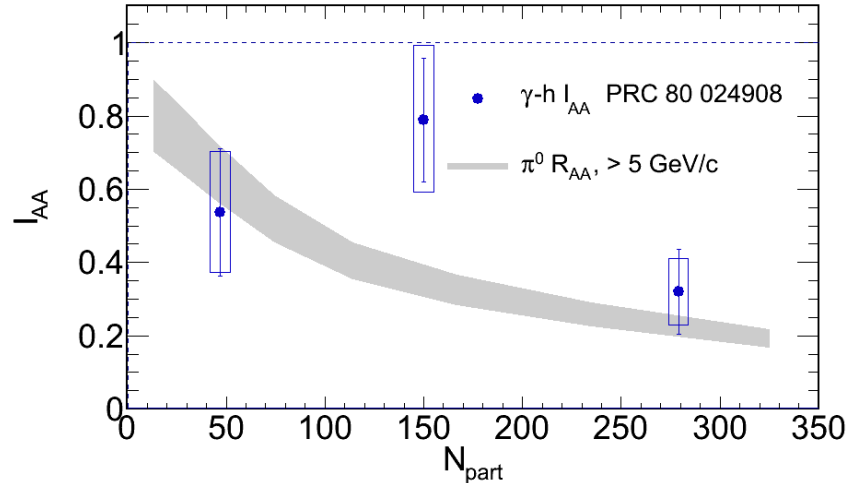


Figure 7.6: The  $I_{AA}$  averaged over the high  $z_T$  regions as function of  $N_{part}$  from the measurement over Run 4 data [40], compared with the  $\pi^0 R_{AA}$  [34].

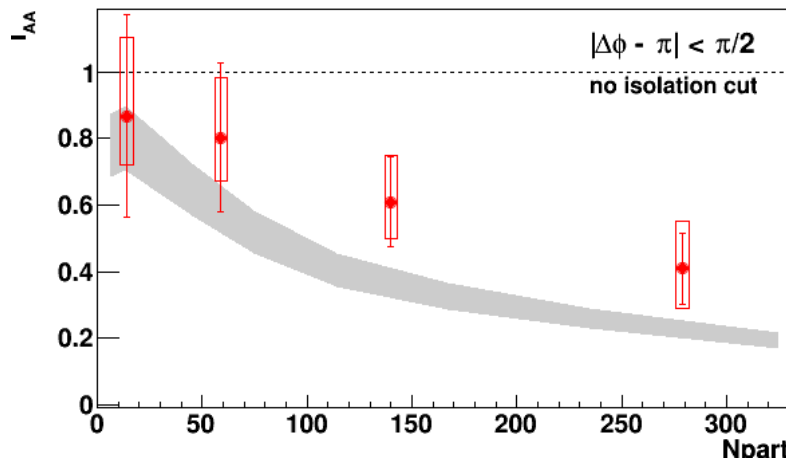


Figure 7.7: The  $I_{AA}$  averaged over the high  $z_T$  regions as function of  $N_{part}$  from the combined Run 7 and Run 10 data without isolation cut applied.

can be seen as an approximate to hadron  $R_{AA}$ . In the previous discussion, we also found that the  $\gamma_{\text{dir}} - h$  is similar to di-hadron  $I_{AA}$  (Fig. 6.4). In principle, the

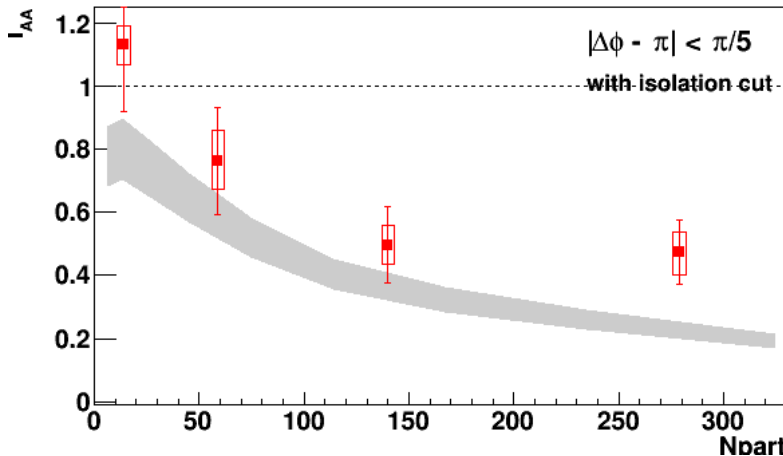


Figure 7.8: The  $I_{AA}$  averaged over the high  $z_T$  regions as function of  $N_{part}$  from the combined Run 7 and Run 10 data with isolation cut applied.

observables  $\gamma_{\text{dir}} - h$   $I_{AA}$ , di-hadron  $I_{AA}$ , and  $\pi^0$   $R_{AA}$  suffer from different kind of geometric effects (or geometric biases), and these differences should be reflected in their  $I_{AA}$  or  $R_{AA}$  value dependence as function of different centralities. To be able to observe the different geometric effects, precise measurement of the three observables should be obtained such that they are significantly disentangled. The evolution of the measurements from Run 4 data (Fig. 7.6) to the combined Run 7 and Run 10 (Fig. 7.7) and to the application of isolation cut (Fig. 7.8) shows that we are on the direction towards the better precision. Further effort should be taken to advance this study. Since the larger Run10 dataset will be added to these current Run7-only isolation cut results in the near future, we can be hopeful of an advance soon.

#### 7.4.2 Low $z_T$ enhancement

The basic result of enhancement in the low  $z_T$  region presumably due to recovery of the jet energy-loss lost energy discussed previously, and recently

published, is shown again in Figure 7.9. The analysis that went into the results from this dissertation for the statistical method shown in the previous section were partially used for this publication ([17]) as a competing analysis that provided cross checks and systematic error exploration, as well as having provided the fine-tuned calibration of the Run10 data included as a key part of the publication. This result establishes, for the first time at RHIC, a statistically significant enhancement in the fragmentation function for jets which is consistent with the recovery of the lost energy of the jets at lower particle momentum.

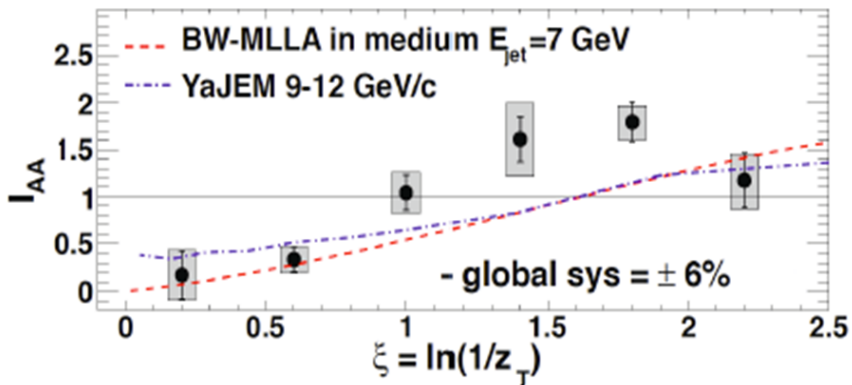


Figure 7.9: The  $I_{AA}$  recently published in [17] to which the analysis in this dissertation made contributions to as well, established a statistically significant enhancement of the fragmentation yield in the low  $z_T$  region.

We quantify this enhancement on the low  $z_T$  region of the  $I_{AA}$  by again taking the average which is obtained from the constant fit, and further explore the centrality dependence of this average. Fig. 7.10 shows the low  $z_T$  average  $I_{AA}$  that is obtained from the statistical method. This is the first look at this centrality dependence at RHIC, therefore there is no previously published measurement by PHENIX that we can use as comparison. The low  $z_T$  averaged  $I_{AA}$  on the most

central event is consistent within the uncertainties with the enhancement that was observed in Fig.'s 6.3 and 7.9. The enhancement above 1 in the value of  $I_{AA}$  seems to slightly increase in mid central 20-40% from the most central 0-20%, although this could just be statistical fluctuation—however it may also be influenced by also the smaller suppression overall as quantified in the previous section, for 20-40%.

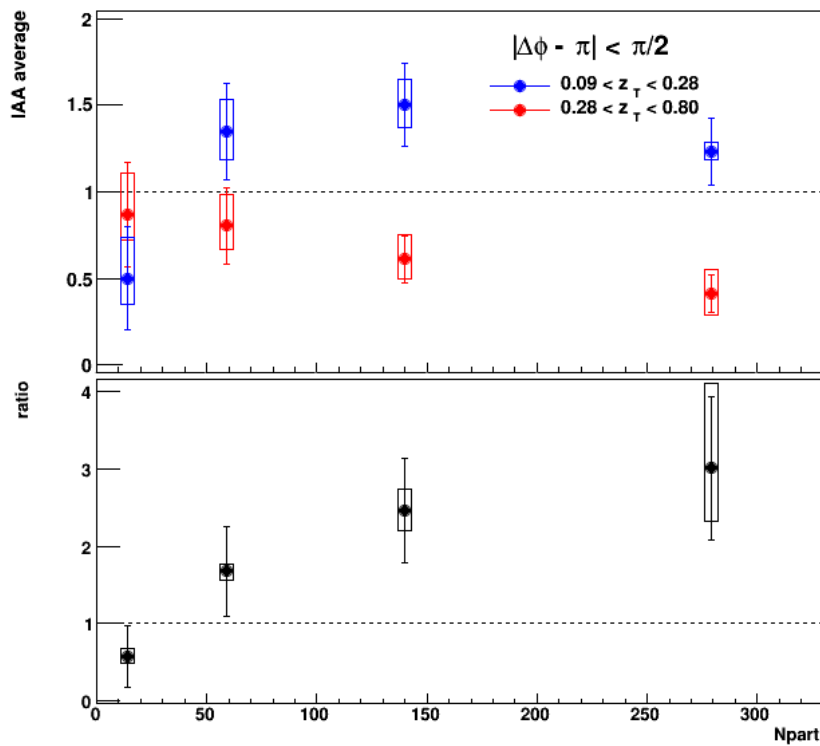


Figure 7.10: (a) The averaged  $I_{AA}$  on the low  $z_T$  regions (blue). The averaged  $I_{AA}$  over the high  $z_T$  region (red) is shown again here for reference, (b) ratio of the low  $z_T$  average to the high  $z_T$  average. These results are obtained without isolation cut applied.

Partially to address this problem, as we mention at the end of Section 7.2, we can use the relative change of the  $I_{AA}$  over different  $z_T$  ranges as indicator of energy loss redistribution, where energy from the yield of high momentum particles is

redistributed to low momentum particles. This is as an alternative to just judging the amount of enhancement by only by how high raw numerical value of  $I_{AA}$  is above 1 by looking at an observable sensitive to potentially statistically significant shape change of the  $I_{AA}$  going from the suppressed high  $z$  region to low  $z$ . We quantify this shape change as the ratio of the  $I_{AA}$  averaged on low  $z_T$  region to the  $I_{AA}$  averaged on high  $z_T$  region, and is shown in the bottom panel of Fig. 7.10. This ratio, that we will refer to as energy recovery factor, gives a value of  $\approx 2$  in general, with small dependency across different centralities. A higher ratio seems to be observed in the most central 0-20% bin compared to the mid-central 20-40%. This is expected, taken that the level of the ratio represents the medium effect of energy redistribution, which should decrease as we go to less dense system.

Similarly, in the mid-peripheral (40 – 60%) bin, an enhancement of low  $z_T$  average  $I_{AA}$  is observed, with a higher level compared to the two more central bins. However, it also shows less amount of energy recovery factor compared to the two more central bins. The reduction of the energy recovery factor seems to be more consistent with the picture of decreasing medium effect at the more peripheral bins, in contrast to looking alone at only the increase of the low  $z_T$  enhancement of the numerical value of  $I_{AA}$  above 1. In the most peripheral (60 – 92%) bin, there is no longer any indication of enhancement, although it's possible that it is not completely ruled out due to the uncertainties. The energy loss recovery factor in this bin is also seems to be more consistent with one, which reflect a smaller medium effect, although again other possibilities are not ruled out.

The low  $z_T$  average  $I_{AA}$  and its ratio to the high  $z_T$  average  $I_{AA}$  is also obtained with the isolation cut method. We found that this measurement over the full away-side region does not provide new informations or add any improvement to the one we have in Fig. 7.10. However, we do found some interesting features when

looking at the  $I_{AA}$  with the away-side integrated over the head region ( $\Delta\phi > 4\pi/5$ ). In Fig. 7.11 we show the  $I_{AA}$  evaluated on different integration range, including the head region, from the previous measurement over the combined Run 7 and Run 10 PHENIX data [17]. The definition of the head region in this dissertation is slightly different with the one in Fig. 7.11. The result of our measurement with the isolation cut is shown in Fig. 7.12.

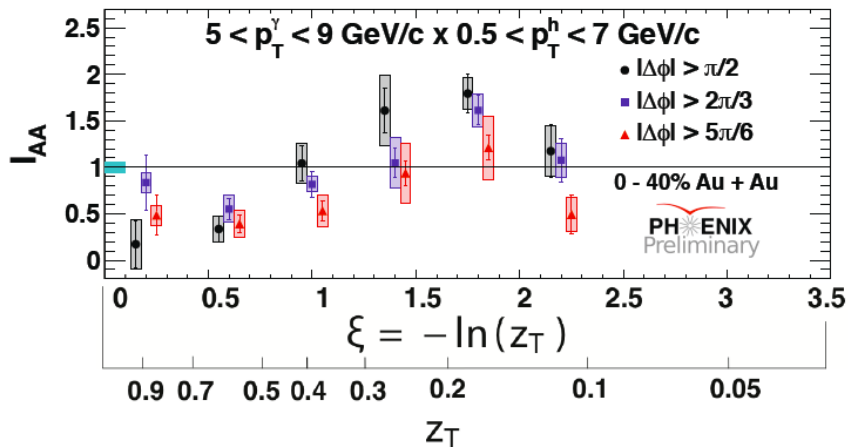


Figure 7.11: The  $I_{AA}$  as function of  $\xi$ , on the central  $0 - 40\%$  centrality bins of the combined Run 7 and Run 10, evaluated at different sizes of integration range [17]. The transformation to the  $z_T$  axis is also shown.

The two central bins in Fig. 7.12 have to be averaged to make a better comparison with what is shown in Fig. 7.11. The combined value of  $I_{AA}$  from the two central bins yield to a value with some probability of being slightly higher than one, means there is an indication of enhancement, which was not observed in the earlier result. To keep in mind, the statistical significance of the estimated average  $I_{AA}$  on two most central bins still allows for the possibility that it is consistent with the previous. However, a more apparent behavior can be seen from the energy loss recovery factor, where it shows a value of about 1.0 to 2.0 for both of the central

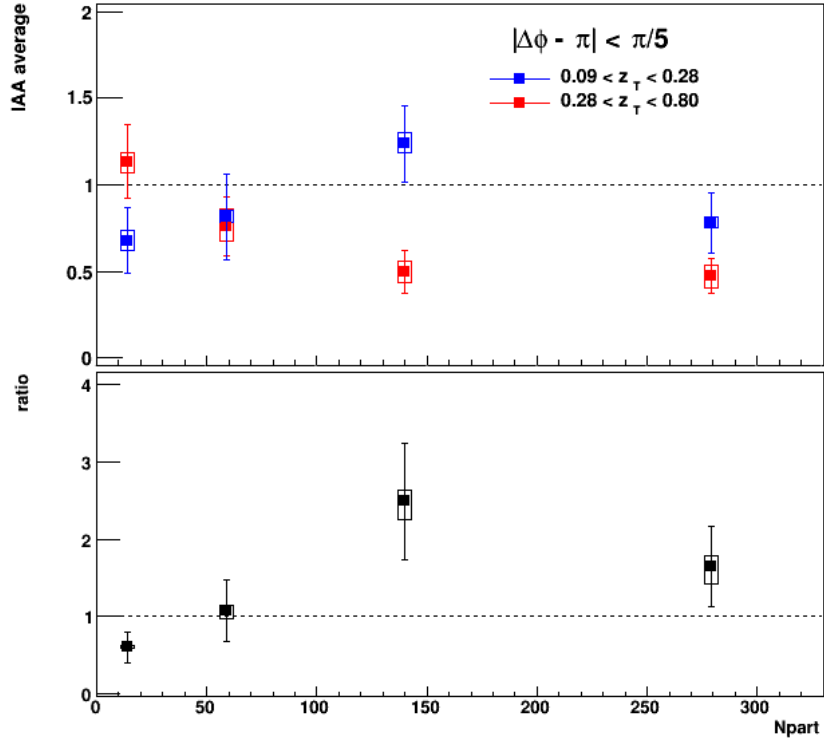


Figure 7.12: (a) The averaged  $I_{AA}$  on the low  $z_T$  regions (blue) and on the high  $z_T$  region (red) is shown again here for reference, (b) ratio of the low  $z_T$  average to the high  $z_T$  average. These results are obtained with the isolation cut applied.

bins, indicating the medium effect. The ratio factor is diminishing as soon as we go to the mid-peripheral 40 – 60% bin, faster than what we observe in the larger integration region of  $\Delta\phi > \pi/2$ . The measurements of different behavior of the energy loss recovery factor on different centralities and different integration regions can provide new constraints to theoretical models of medium induced energy loss.

Previously we mention the changes of the  $v_2$  values of the isolated photons that have to be taken into account as additional systematics to the isolated  $\gamma_{\text{dir}} - h$  yields. Here we show the effect of the changes of isolated photon's  $v_2$  to our results. The low  $z_T$  average  $I_{AA}$  from three different set of  $v_2$  values are shown in Fig. 7.13.

The three scenarios include an unmodified photon  $v_2$ , a zero  $v_2$ , which is the 'expected' value for isolated photons, and a negative  $v_2$ , which gives the conservative estimate of the reduction. These different choices are to be applied to the inclusive isolated photons. We conclude that the all three possibilities are consistent with each other, and any choice of the isolated  $v_2$  value can be used to represent the final results qualitatively. We do not include the addition of the systematics caused by the changes, since full understanding of the isolated photon's  $v_2$  is still in development. We choose not to include this variation in the systematic uncertainty shown in order to highlight the potential of the new method of isolation cuts in A+A for reducing the overall uncertainty since we are confident eventually this additionally  $v_2$  uncertainty will be eliminated.

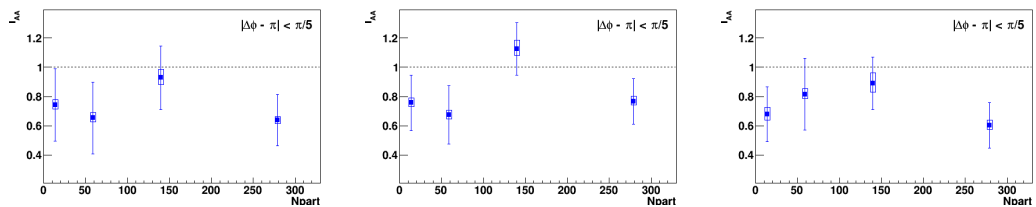


Figure 7.13: The  $I_{AA}$  averaged over low  $z_T$  region as function of  $N_{part}$ , obtained with the isolation cut applied and using the three different values of  $v_2$  for the isolated inclusive and decay photons.

## 8 Summary

### The Analysis

The measurement of the  $\gamma_{\text{dir}} - h$  pair correlations is performed over the PHENIX Run 7 and Run 10 Au+Au data sets. An additional analysis where isolation cut is applied is also developed for the first time at RHIC, and completed for the Run 7 data. Some parts of the measurement are a re-evaluation of earlier studies using the same data set and an older data set of Run 4 Au+Au collision, where substantially increased precision provides more information. Other parts are new results which provide interesting insight into properties of the mechanisms of jet energy loss.

### Comparison with Earlier Studies

The measurement of  $\gamma_{\text{dir}} - h$  pair correlations in p+p system previously made [16] shows that the integrated away-side yields represent the fragmentation function of the quark that is produced in the Compton scattering process. The measurement of  $I_{AA}$  in Au+Au collision shows the modification of p+p fragmentation function, which is interpreted as the effect of medium induced energy loss.

An important part of the away-side yield modification is observed to be clear suppression of particle production at high  $z_T = \langle p_{T,\text{assoc}} \rangle / \langle p_{T,\text{trig}} \rangle$ . This is one of the results that is re-confirmed in this dissertation and can now be seen with more precision and more differentially. In this dissertation the measurement of the suppression is obtained with better significance in four centrality bins. The

improvement is obtained because of the increased statistics from the combined Run 7 and Run 10 data, as well as the application of the isolation cut. A trigger is isolated if the sum of energies of particles around it is less than a certain threshold. In the isolation cut method, only isolated photon triggers are used. The most obvious effect of the isolation cut is the reduction of the systematic errors on the integrated away-side yields.

Additionally, the analysis, new statistics, and methods used in this dissertation contributed to the establishment of the enhancement at low  $z_T$  region of the  $I_{AA}$  with statistical significance (see publication [16]), for the first time at RHIC. This enhancement which has also been confirmed in other observables at the Large Hadron Collider and RHIC, has been widely interpreted as the recovery of the energy lost by the jet's parton into lower momentum fragments. In addition to this basic establishment of this result which only included the behavior in a single centrality bin, the dissertation's results themselves directly also expand the exploration of this low  $z$  enhancement to include its centrality dependence, again for the very first time at RHIC.

### **Implementation and Effect of the Isolation Cut**

Also in this dissertation analysis, event by event isolation cuts are developed and made in Au+Au collisions, including all centralities, in order to improve the identification of direct photons, for the first time at RHIC. Performing this analysis is a non-trivial technical accomplishment because of the large underlying event in Au+Au which strongly affects the probability of the photons to be isolated from other particles. Prior to the implementation of the isolation cut, simulation and optimization studies are conducted. The simulation shows that the level of the uncertainty that came from the decay mapping method and direct photon

subtraction formula are comparable when the isolation cut is applied and not applied. The isolation cut reduces the overall statistics, but it also improves the signal to background ratio. Within the application of the isolation cut, additional procedures to obtain the isolated decay mapping and effective  $R_\gamma$  are introduced. From the optimization study, a set of parameters is obtained and used in the real data analysis. It assumed that these are the parameters that minimizes the combination of the statisticsl and systematic errors.

Overall a fair improvement in the precision of the results is found in the analysis of the real data applied to the Run 7 dataset alone, due to the application of the isolation cut . This is especially true for high  $z_T$  and most peripheral centralites. The improvements indicate that even further improvement and better precision will be imminent with the inclusion of the Run 10 dataset to the isolation cut analysis.

### **New Outlook: The Energy Redistribution Factor**

The measurement on the low  $z_T$  region of the  $I_{AA}$  over different centrality bins could provide a new result that explains the behavior of the enhancement as a function of the medium density. Unfortunately the achieved level of uncertainty does not allow for a precise conclusion on this centrality dependence, especially when judging only by the numerical value of  $I_{AA}$  and its enhancement above 1. One can at least see a hint that the enhancement exists up to mid-peripheral 40-60% bin. The measurement over the isolated photon of Run 7 Au+Au data does not produce overall improvement. We find, however, that more statistically significant information is found by looking at the “energy recovery” factor which is the ratio of low to high  $z$   $I_{AA}$ . This observable shows an even more pronounced effect for the energy recovery, including a previously unnoticed recovery at small angles of the “head” region visible in the isolation cut analysis results.

## Future Prospects

In future, there are many improvements that can be performed based on the measurement completed in this dissertation. One can obtain a better  $z_T$  distribution of the away-side yield and the  $I_{AA}$  by adopting the  $z_T$  binning method. The background level obtained by the  $p_T$  binning procedure in this analysis is needed in the  $z_T$  binning method, therefore one can say the initial step has been taken care of. And finally, the behavior at low  $z_T$  can be further explored by including lower  $p_T$  particles, both in p+p and in Au+Au.

On the theoretical side of this study, the  $I_{AA}$ -modification over different centrality bins can be used to test any model that includes medium density as a factor that determines the energy loss of high- $p_T$  particles, which in turn can provide a solid understanding of energy loss mechanism by the QGP. So far, energy loss models are only available for the most central bins. In future, we hope to see theoretical models that we can compare to, with improvement in our measurement on the suppression and the enhancement,

As a conclusion, the measurements of the  $\gamma_{\text{dir}} - h$  pair correlations have provided interesting results and hints. Advances in the analysis procedure, development of more powerful and larger coverage detectors, as well as a more extensive theoretical study, are still underway. High precision measurements are important contributions to the field of relativistic heavy ion collision. This dissertation yields new insights, and takes another important step in the direction of progressively increasing precision.

## References

- [1] F. Halzen and A. D. Martin, *Quarks and Leptons: An Introductory Course in Modern Particle Physics*, ISBN-13: 978-0471887416 (1984)
- [2] K. Adcox *et al.* (PHENIX Collaboration), Nucl. Phys. A 757, 184 (2005)
- [3] E. V. Shuryak, Phys. Rep. 6171 (1980)
- [4] J. Beringer *et al.*, Phys. Rev. D 86, 010001 (2012)
- [5] Dept. of Energy Dept. of Nuclear Physics Long Range Plan 2007
- [6] D.J. Gross, F. Wilczek, Phys. Rev. Lett. 30, 1343 (1973)
- [7] A. Adare *et al.* (PHENIX Collaboration), Phys. Rev. Lett. 98, 162301 (2007)
- [8] S. S. Adler *et al.* (PHENIX Collaboration), Phys. Rev. Lett. 91, 072301 (2003)
- [9] S. S. Adler *et al.* (PHENIX Collaboration), Phys. Rev. C 76, 034904 (2007)
- [10] S. S. Adler *et al.* (PHENIX Collaboration), Phys. Rev. Lett. 94, 232301 (2005)
- [11] S. S. Adler *et al.* (PHENIX Collaboration), Phys. Rev. C 75, 024909 (2007)
- [12] J. Adams, *et al.* (STAR Collaboration), Nucl. Phys. A 757, 102 (2005)
- [13] J. Frantz, *Direct Photon Shine: Direct Photon and  $\pi^0$  Production in  $\sqrt{s_{NN}} = 200 \text{ GeV } Au + Au \text{ Collisions}$* , Columbia University Ph.D. Thesis (2005)

- [14] T. Renk, Phys. Rev. C 80, 014901 (2009)
- [15] C. A. Salgado and U. A. Wiedemann, Phys. Rev. D 68, 014008 (2003)
- [16] A. Adare *et al.* (PHENIX Collaboration), Phys. Rev. D 82, 072001 (2010)
- [17] A. Adare *et al.* (PHENIX Collaboration), Phys. Rev. Lett. 111, 032301 (2013)
- [18] W. Braunschweig *et al.* (TASSO Collaboration), Z. Phys. C 47, 187 (1990)
- [19] M. Harrison, T. Ludlam, and S. Ozaki, Nucl. Instrum. Meth. A499, 235 (2003)
- [20] PHENIX Collaboration (D. Morrison *et al.*), Nucl. Phys. A638, 565-570 (1998)
- [21] <https://www.phenix.bnl.gov>
- [22] X. N. Wang and M. Gyulassy, Phys. Rev. D 44, 3501 (1991)
- [23] M. Allen *et al.*, Nucl. Instrum. Meth. A499, 549 (2003)
- [24] PHENIX Collaboration (E. Richardson *et al.*), Nucl. Instrum. Meth. A636, 99 (2011)
- [25] A. Adare *et al.* (PHENIX Collaboration), Phys. Rev. Lett. 107, 252301 (2011)
- [26] K. Adcox *et al.*, Nucl. Instrum. Meth. A499, 489 (2003)
- [27] K. Adcox *et al.*, Nucl. Instrum. Meth. A497, 263 (2003)
- [28] M. Aizawa *et al.*, Nucl. Instrum. Meth. A499, 508 (2003)
- [29] L. Aphecetche *et al.*, Nucl. Instrum. Meth. A499, 521 (2003)
- [30] <http://www.rhichome.bnl.gov>
- [31] N. Ajitanand *et al.*, Phys. Rev. C 72, 011902(R) (2005)

- [32] S. Agostinelli *et al.*, Nucl. Instrum. Meth. A506, 250 (2003)
- [33] M. Nguyen, *Two particle correlations with Direct Photon and  $\pi^0$  triggers in 200 GeV  $p+p$  and Au+Au collisions*, Stony Brook University Ph.D. Thesis (2009)
- [34] A. Adare *et al.* (PHENIX Collaboration), Phys. Rev. Lett. 101, 232301 (2008)
- [35] M. Connors, *Direct Photon Tagged Jets in 200 GeV Au+Au Collisions at PHENIX*, Stony Brook University Ph.D. Thesis (2011)
- [36] A. Adare, *Transverse momentum evolution of neutral pion triggered dihadron correlations in Au+Au collisions at  $\sqrt{s_{NN}} = 200$  GeV*, University of Colorado Ph.D. Thesis (2010)
- [37] G. Alexander *et al.* (OPAL Collaboration), Z. Phys. C 69, 543 (1996)
- [38] P. Abreu *et al.* (DELPHI Collaboration), Eur. Phys. J. C 13, 573 (2000)
- [39] S. Adler *et al.* (PHENIX Collaboration), Phys. Rev. D 74, 072002 (2006)
- [40] A. Adare *et al.* (PHENIX Collaboration), Phys. Rev. C 80, 024908 (2009)
- [41] N. Borghini and U. A. Wiedermann, arXiv:hep-ph/0506218v1 (2005)
- [42] S. Adler *et al.* (PHENIX Collaboration), Phys. Rev. Lett. 98, 012002 (2007)
- [43] T. Isobe, *Production of Direct Photons and Neutral Pions in Relativistic Au+Au Collisions*, Center for Nuclear Study, University of Tokyo Ph.D. Thesis (2007)
- [44] N. Rivelis and J. Frantz, *Analysis of Run 7 + Run 10 Au+Au Photon-Hadron Correlations with Isolation CutNote*, PHENIX Internal Analysis Note AN1183 (2014)

## Appendix: Plots

### A.1 Correlations Function with statistical method

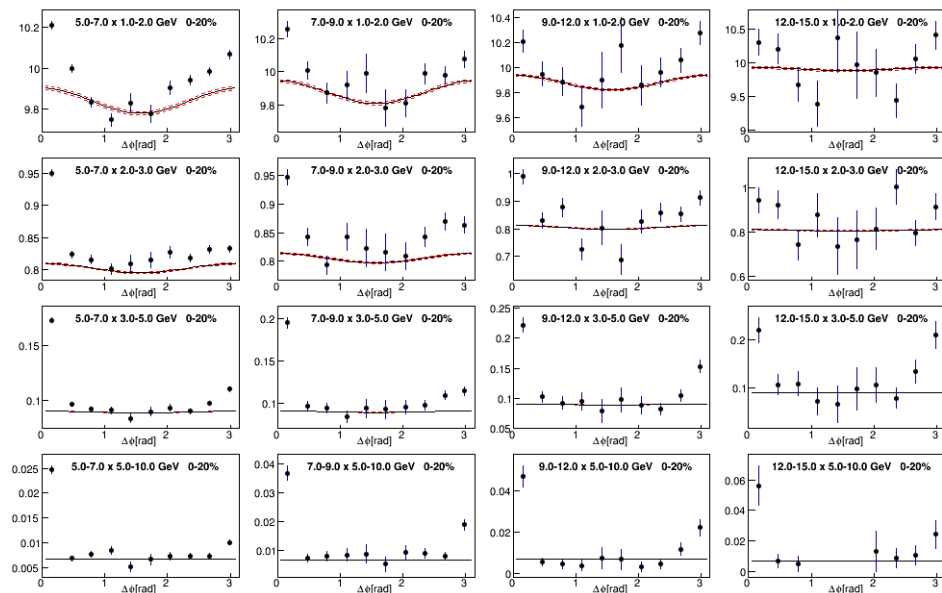


Figure A.1: Correlations function and combinatoric background of  $\gamma_{\text{inc}} - h$  pairs in 0 – 20% Au+Au with statistical method. The  $x$ -axis is the  $\Delta\phi$ .

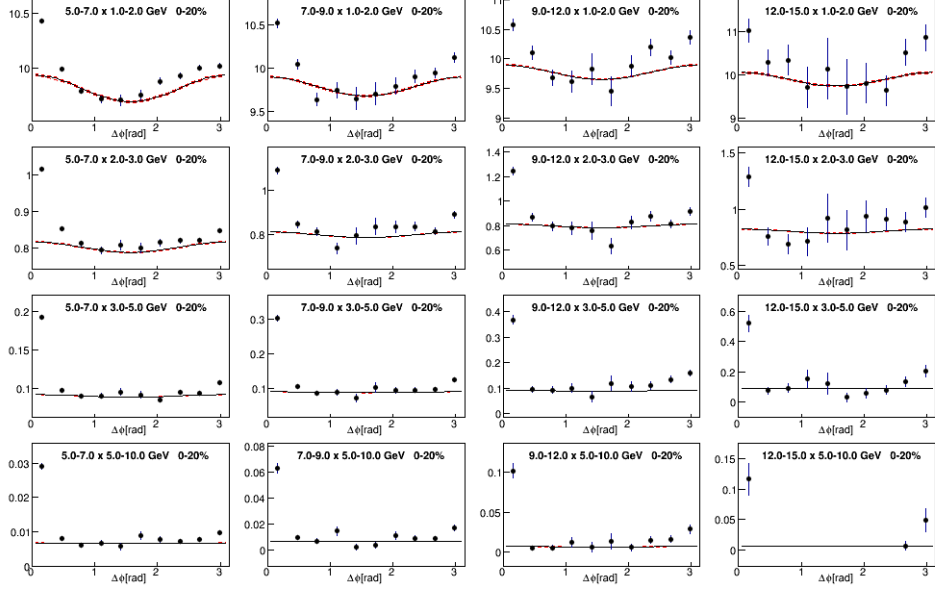


Figure A.2: Correlations function and combinatoric background of  $\pi^0 - h$  pairs in 0 – 20% Au+Au with statistical method. The  $x$ -axis is  $\Delta\phi$ .

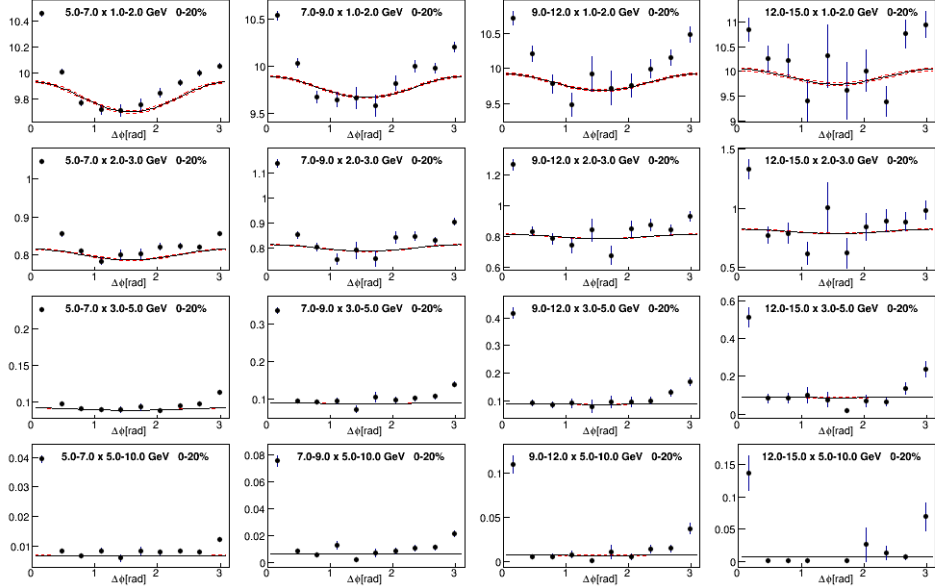


Figure A.3: Correlations function and combinatoric background of  $\gamma_{\text{dec}} - h$  pairs in 0 – 20% Au+Au with statistical method. The  $x$ -axis is  $\Delta\phi$ .

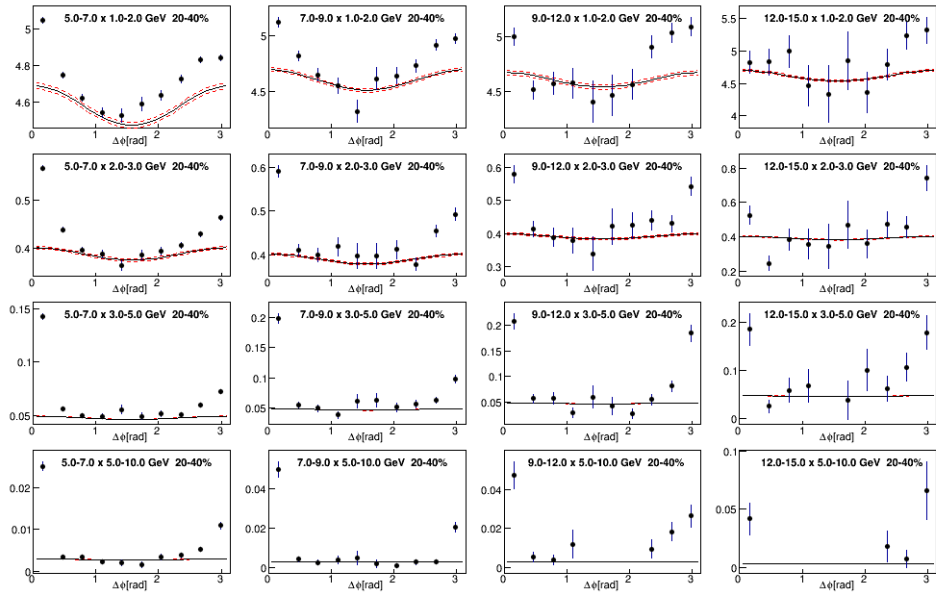


Figure A.4: Correlations function and combinatoric background of  $\gamma_{\text{inc}} - h$  pairs in 20 – 40% Au+Au with statistical method. The  $x$ -axis is  $\Delta\phi$ .

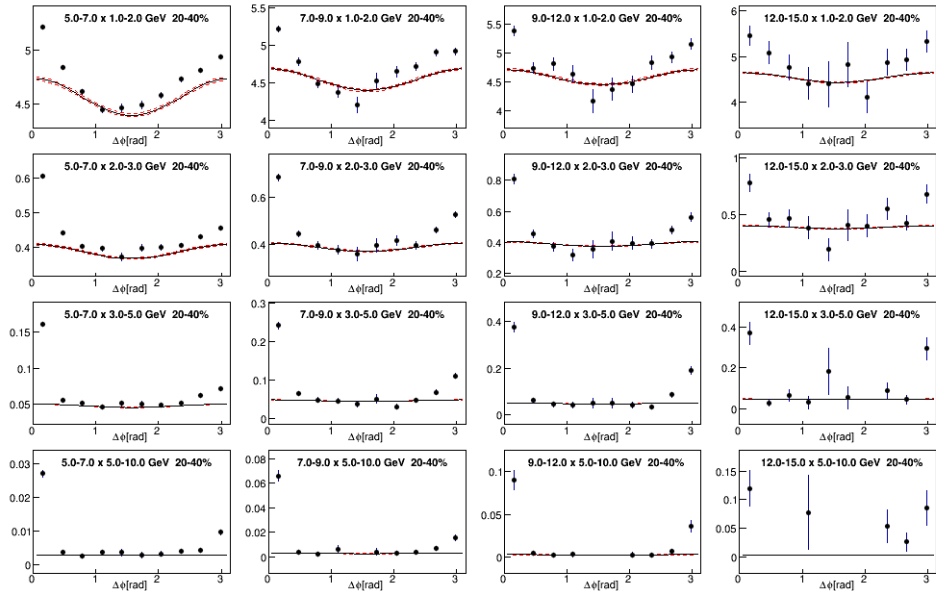


Figure A.5: Correlations function and combinatoric background of  $\pi^0 - h$  pairs in 20 – 40% Au+Au with statistical method. The  $x$ -axis is  $\Delta\phi$ .

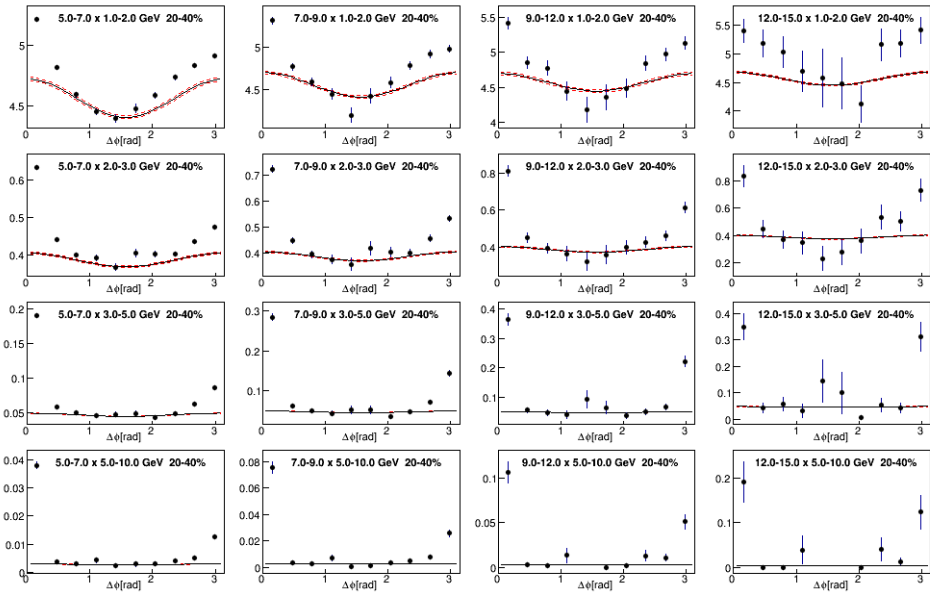


Figure A.6: Correlations function and combinatoric background of  $\gamma_{\text{dec}} - h$  pairs in 20 – 40% Au+Au with statistical method. The  $x$ -axis is  $\Delta\phi$ .

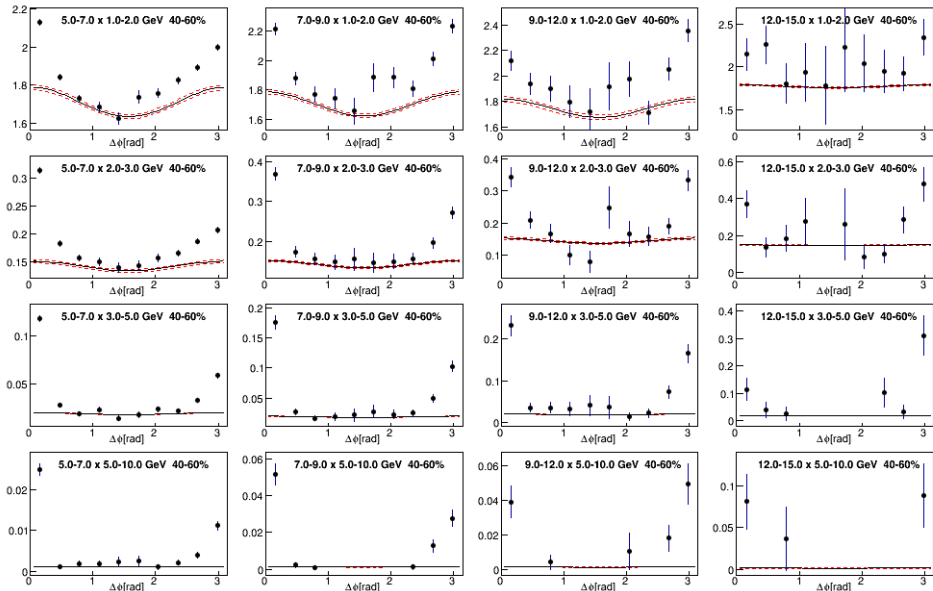


Figure A.7: Correlations function and combinatoric background of  $\gamma_{\text{inc}} - h$  pairs in 40 – 60% Au+Au with statistical method. The  $x$ -axis is  $\Delta\phi$ .

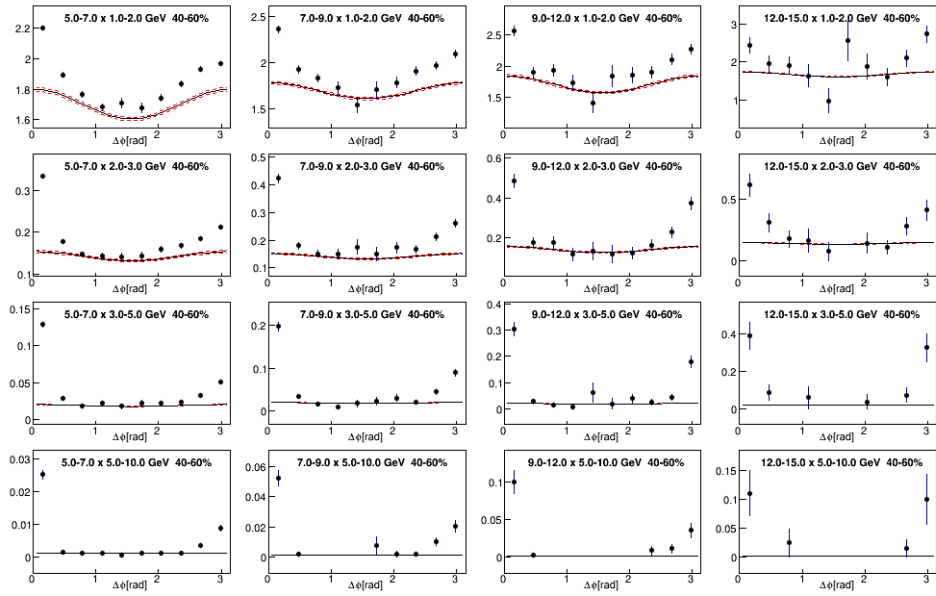


Figure A.8: Correlations function and combinatoric background of  $\pi^0 - h$  pairs in 40 – 60% Au+Au with statistical method. The  $x$ -axis is  $\Delta\phi$ .

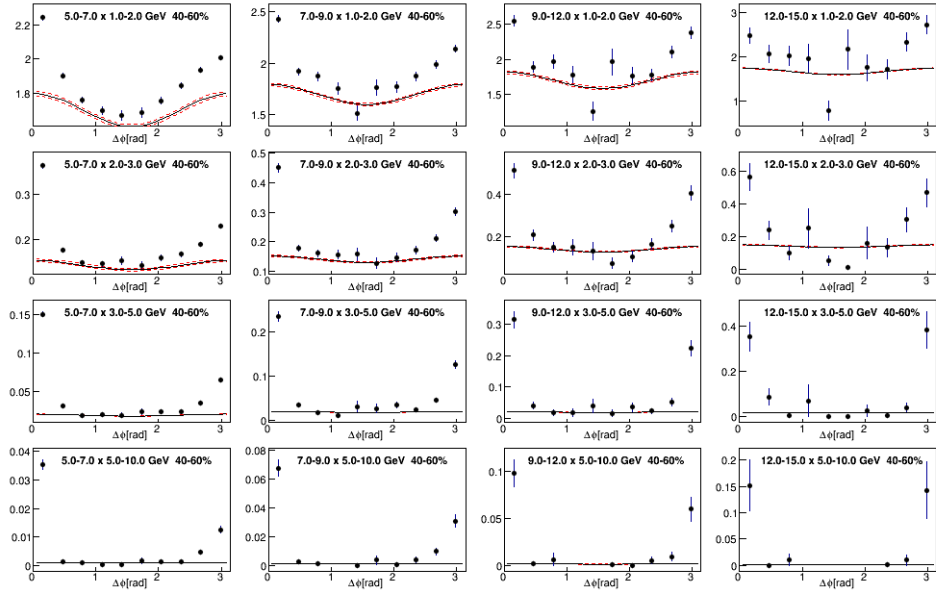


Figure A.9: Correlations function and combinatoric background of  $\gamma_{\text{dec}} - h$  pairs in 40 – 60% Au+Au with statistical method. The  $x$ -axis is  $\Delta\phi$ .

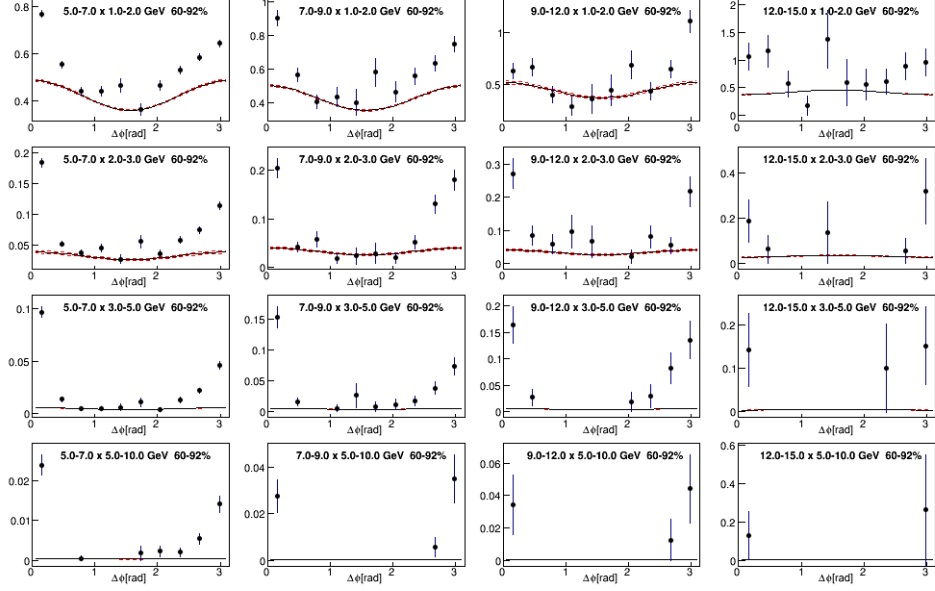


Figure A.10: Correlations function and combinatoric background of  $\gamma_{\text{inc}} - h$  pairs in 60 – 92% Au+Au with statistical method. The  $x$ -axis is  $\Delta\phi$ .

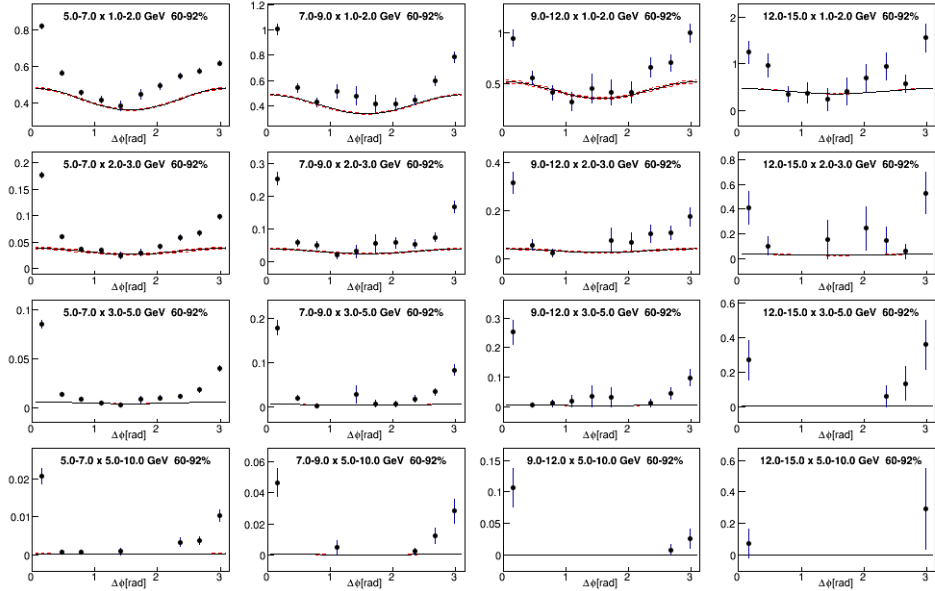


Figure A.11: Correlations function and combinatoric background of  $\pi^0 - h$  pairs in 60 – 92% Au+Au with statistical method. The  $x$ -axis is  $\Delta\phi$ .

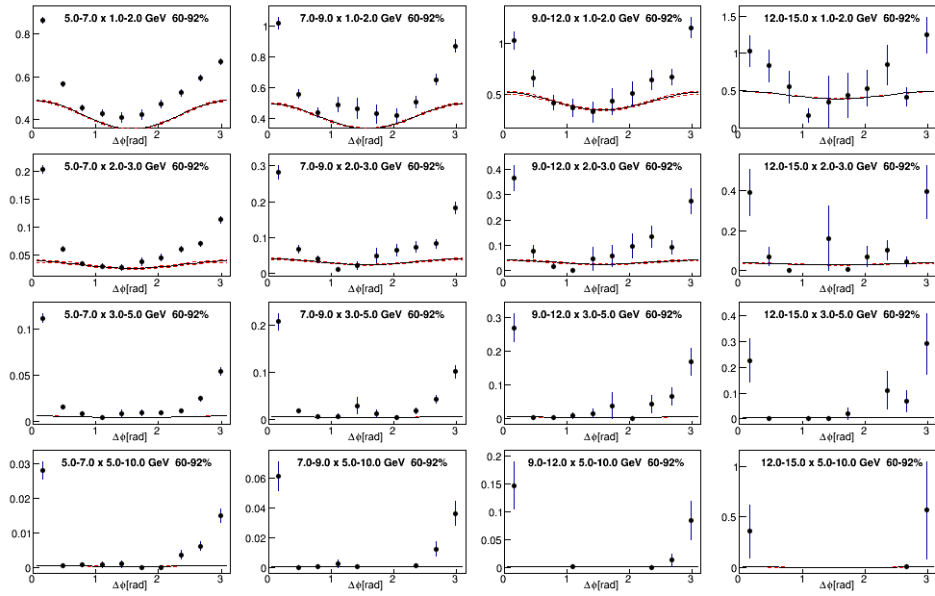


Figure A.12: Correlations function and combinatoric background of  $\gamma_{\text{dec}} - h$  pairs in 60 – 92% Au+Au with statistical method. The  $x$ -axis is  $\Delta\phi$ .

## A.2 Correlations Function with isolation cut method

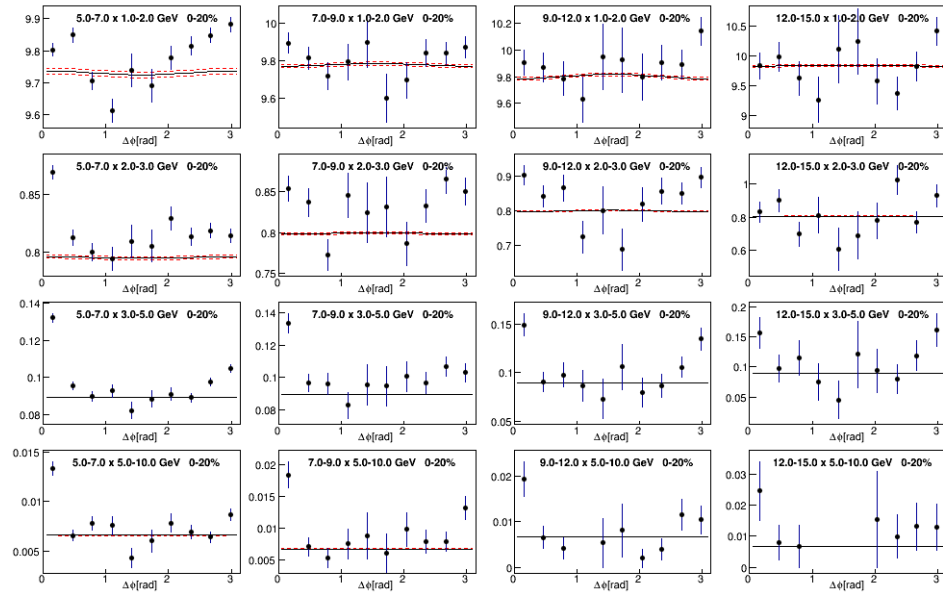


Figure A.13: Correlations function and combinatoric background of  $\gamma_{\text{inc}} - h$  pairs in  $0 - 20\%$  Au+Au with isolation cut method. The  $x$ -axis is  $\Delta\phi$ .

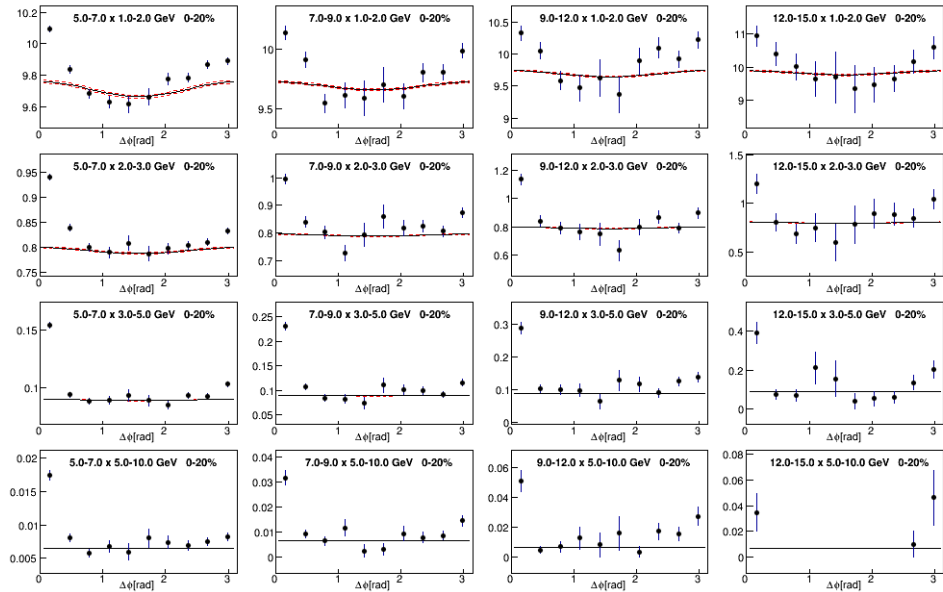


Figure A.14: Correlations function and combinatoric background of  $\pi^0 - h$  pairs in 0 – 20% Au+Au with isolation cut method. The  $x$ -axis is  $\Delta\phi$ .

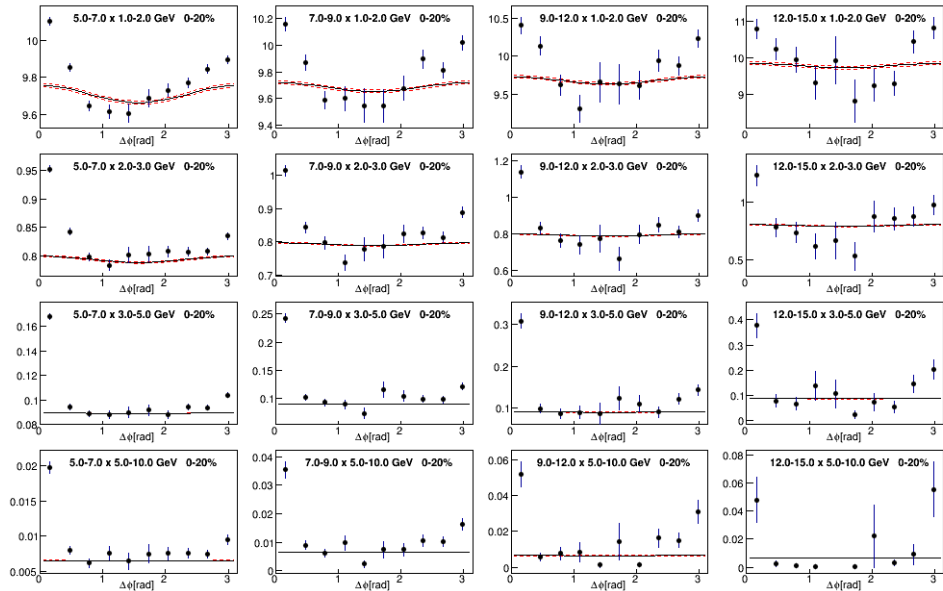


Figure A.15: Correlations function and combinatoric background of  $\gamma_{\text{dec}} - h$  pairs in 0 – 20% Au+Au with isolation cut method. The  $x$ -axis is  $\Delta\phi$ .

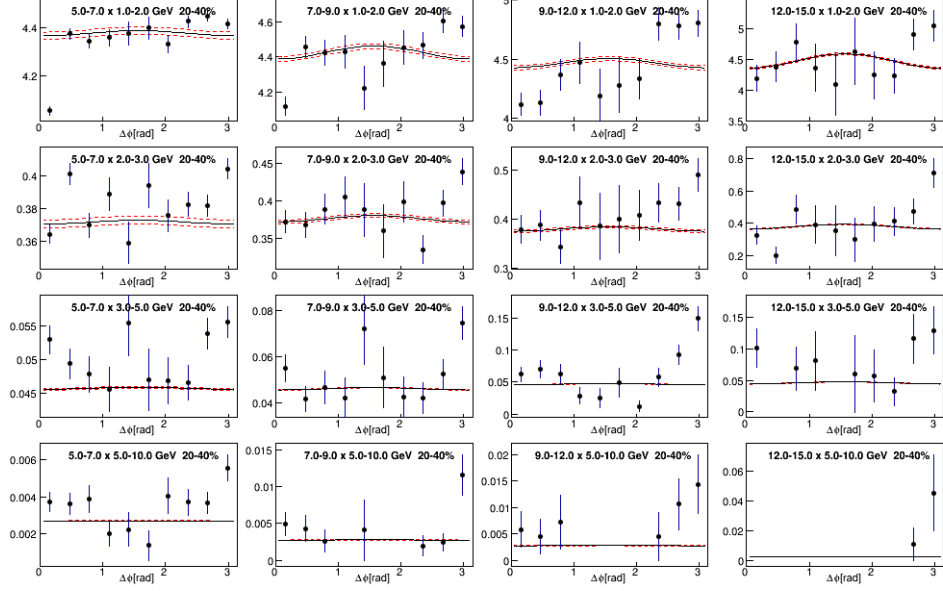


Figure A.16: Correlations function and combinatoric background of  $\gamma_{\text{inc}} - h$  pairs in 20 – 40% Au+Au with isolation cut method. The  $x$ -axis is  $\Delta\phi$ .

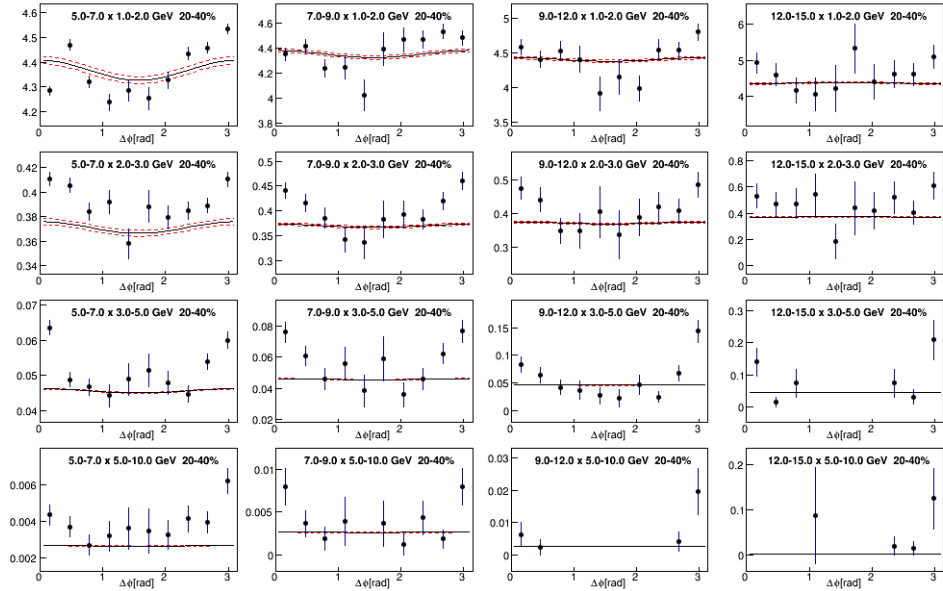


Figure A.17: Correlations function and combinatoric background of  $\pi^0 - h$  pairs in 20 – 40% Au+Au with isolation cut method. The  $x$ -axis is  $\Delta\phi$ .

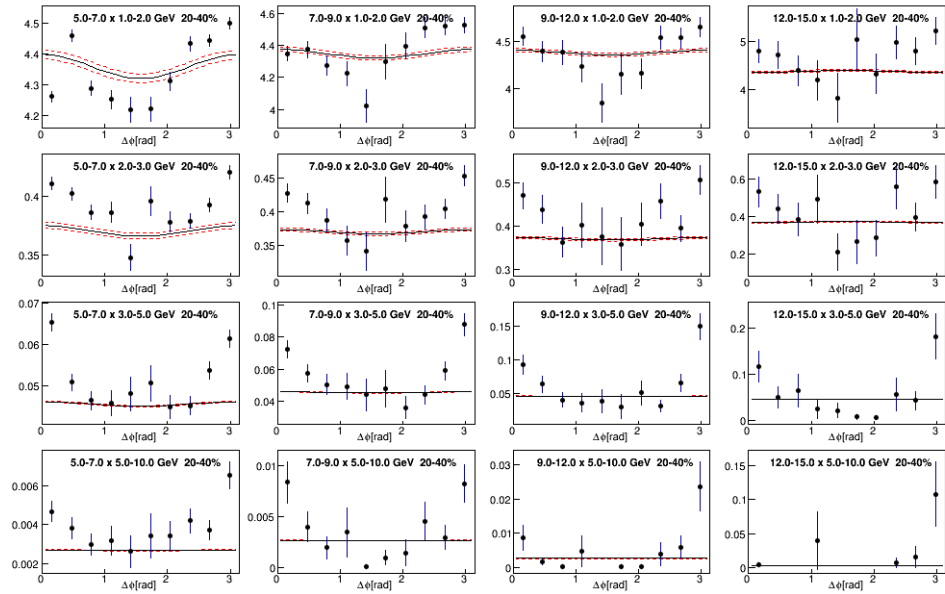


Figure A.18: Correlations function and combinatoric background of  $\gamma_{\text{dec}} - h$  pairs in 20 – 40% Au+Au with isolation cut method. The  $x$ -axis is  $\Delta\phi$ .

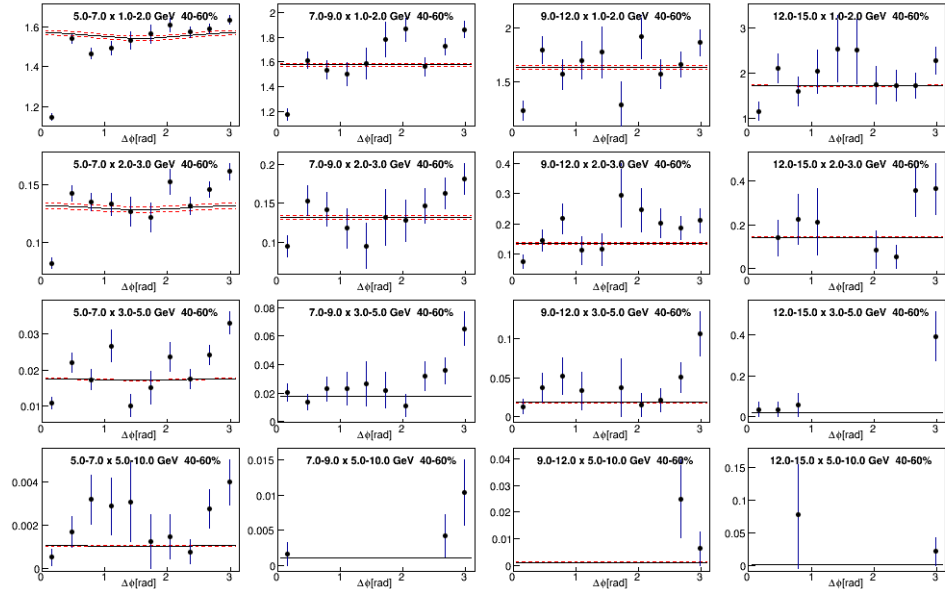


Figure A.19: Correlations function and combinatoric background of  $\gamma_{\text{inc}} - h$  pairs in 40 – 60% Au+Au with isolation cut method. The  $x$ -axis is  $\Delta\phi$ .

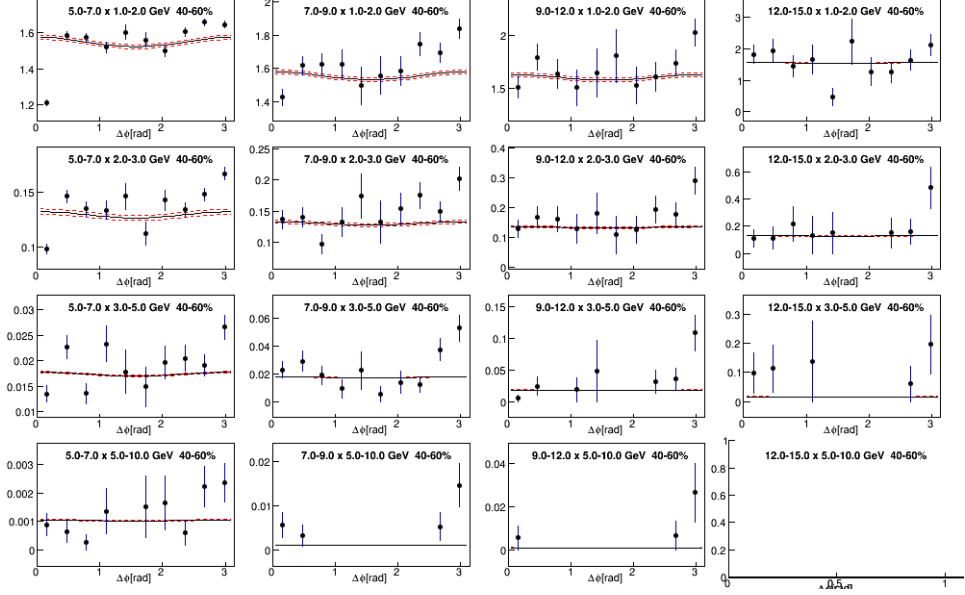


Figure A.20: Correlations function and combinatoric background of  $\pi^0 - h$  pairs in 40 – 60% Au+Au with isolation cut method. The  $x$ -axis is  $\Delta\phi$ .

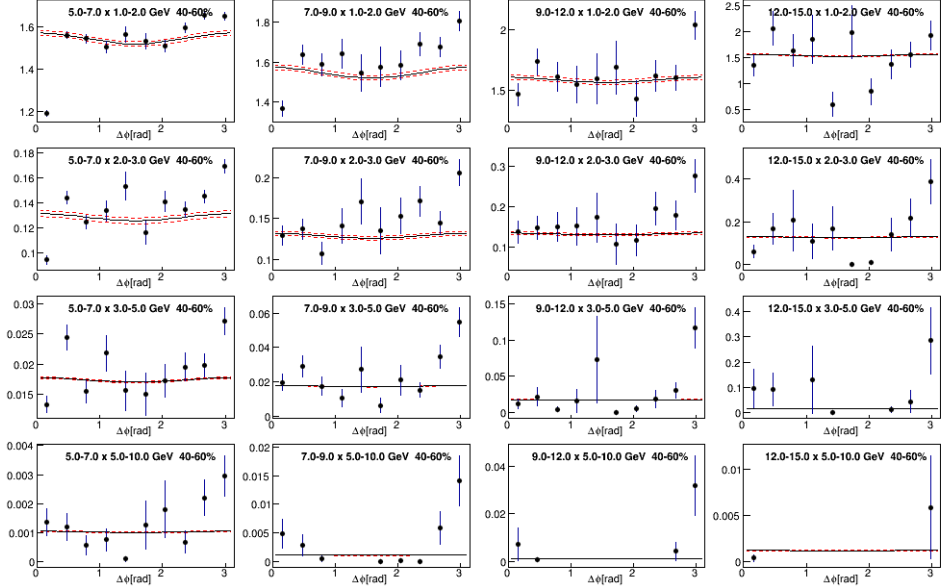


Figure A.21: Correlations function and combinatoric background of  $\gamma_{\text{dec}} - h$  pairs in 40 – 60% Au+Au with isolation cut method. The  $x$ -axis is  $\Delta\phi$ .

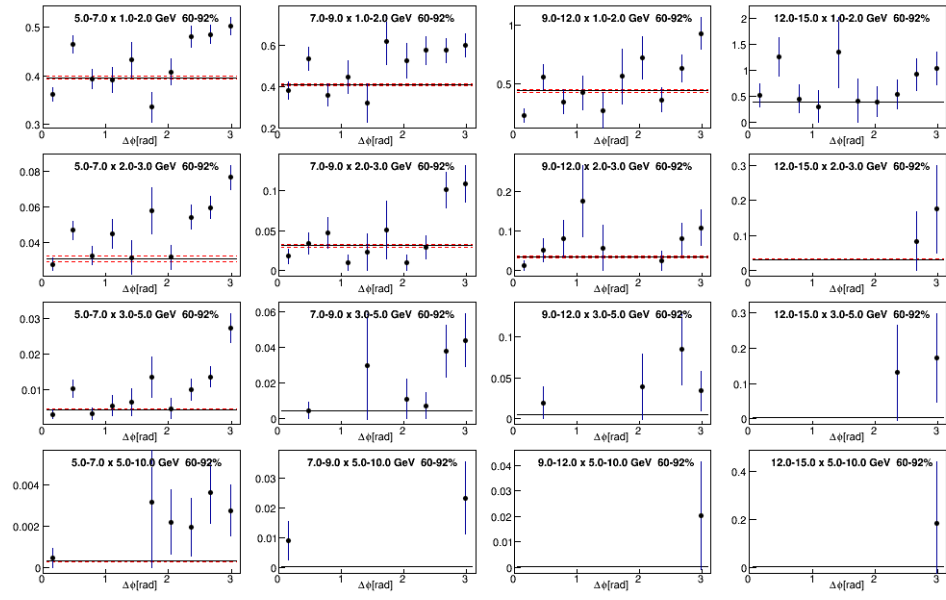


Figure A.22: Correlations function and combinatoric background of  $\gamma_{\text{inc}} - h$  pairs in 60 – 92% Au+Au with isolation cut method. The  $x$ -axis is  $\Delta\phi$ .

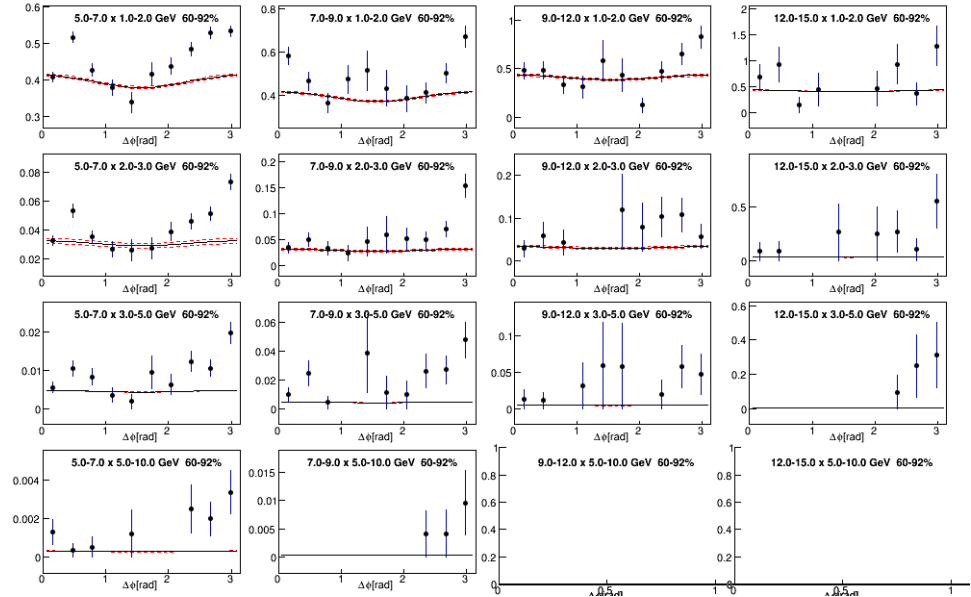


Figure A.23: Correlations function and combinatoric background of  $\pi^0 - h$  pairs in 60 – 92% Au+Au with isolation cut method. The  $x$ -axis is  $\Delta\phi$ .

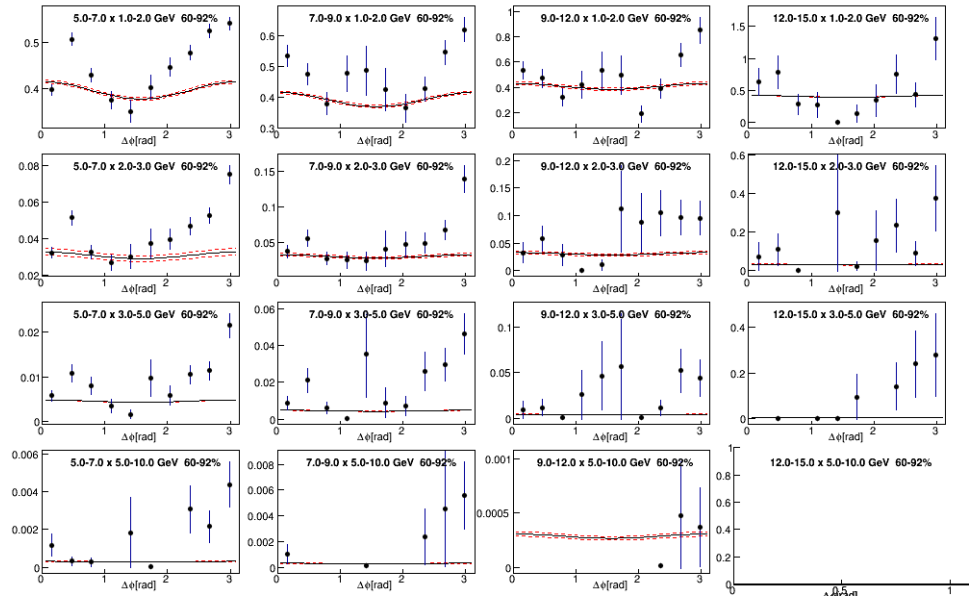


Figure A.24: Correlations function and combinatoric background of  $\gamma_{\text{dec}} - h$  pairs in 60 – 92% Au+Au with isolation cut method. The  $x$ -axis is  $\Delta\phi$ .

### A.3 Jet Functions with statistical method

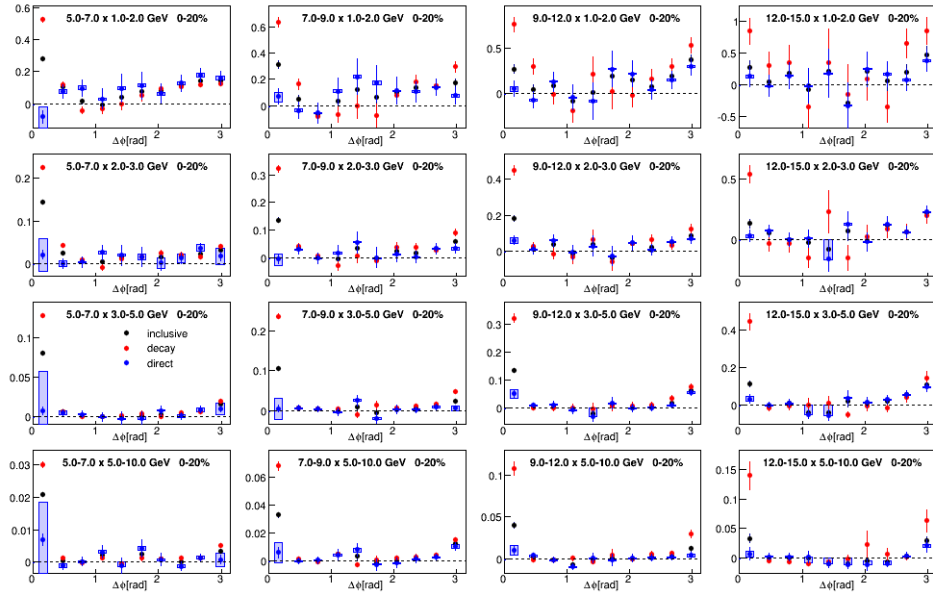


Figure A.25: Jet function of  $\gamma_{\text{inc}} - h$ ,  $\gamma_{\text{dec}} - h$  and  $\gamma_{\text{dir}} - h$  pairs in 0 – 20% Au+Au with statistical method. The  $x$ -axis is  $\Delta\phi$ .

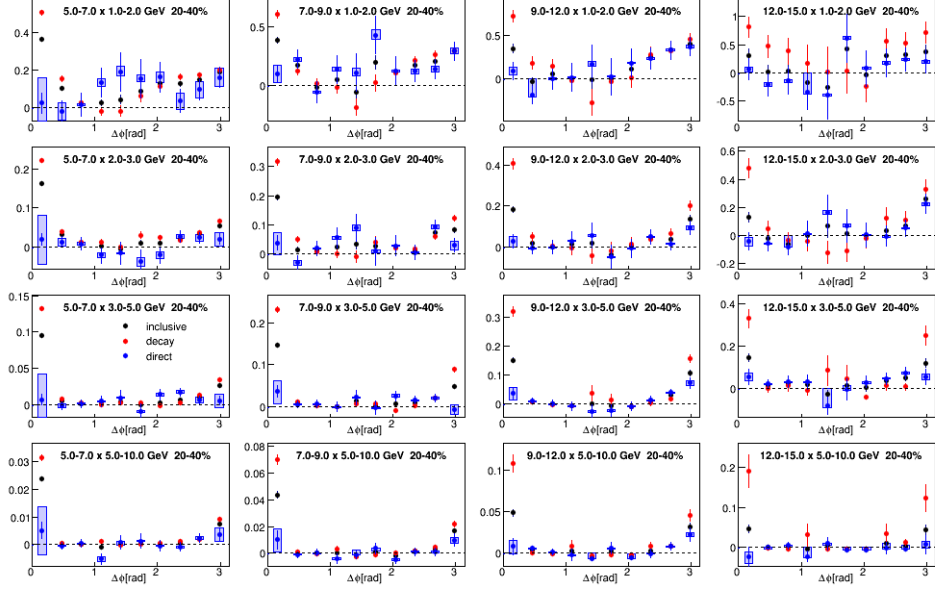


Figure A.26: Jet function of  $\gamma_{\text{inc}} - h$ ,  $\gamma_{\text{dec}} - h$  and  $\gamma_{\text{dir}} - h$  pairs in 20 – 40% Au+Au with statistical method. The  $x$ -axis is  $\Delta\phi$ .

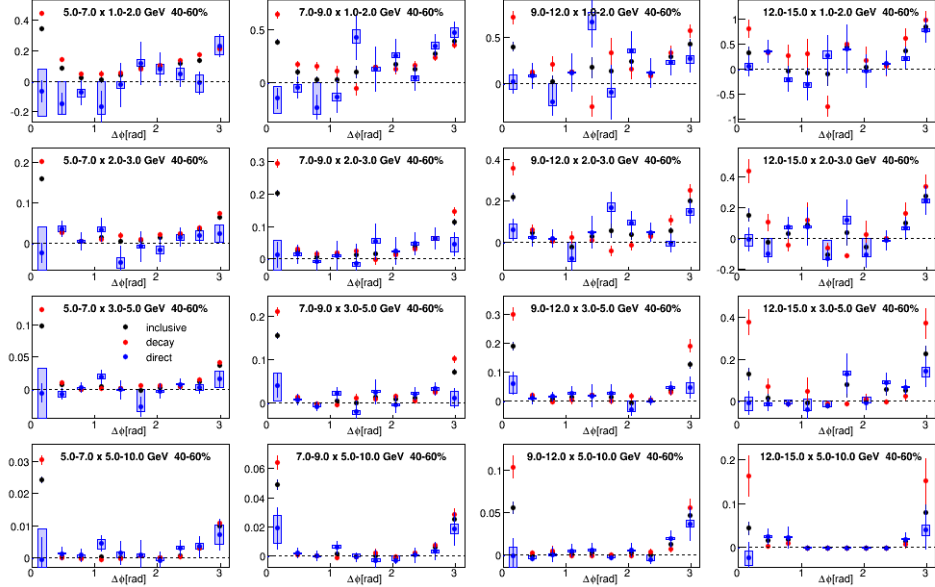


Figure A.27: Jet function of  $\gamma_{\text{inc}} - h$ ,  $\gamma_{\text{dec}} - h$  and  $\gamma_{\text{dir}} - h$  pairs in 40 – 60% Au+Au with statistical method. The  $x$ -axis is  $\Delta\phi$ .

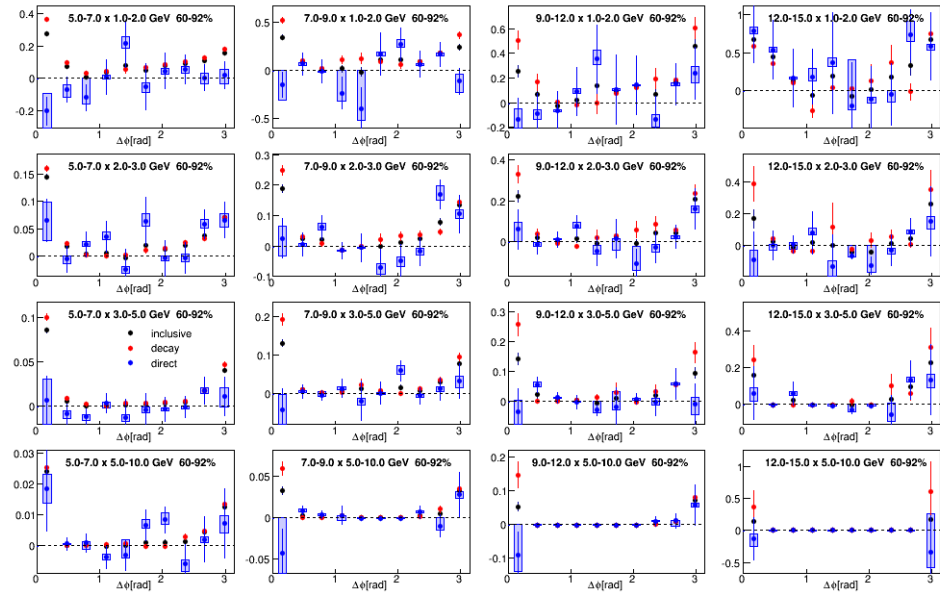


Figure A.28: Jet function of  $\gamma_{\text{inc}} - h$ ,  $\gamma_{\text{dec}} - h$  and  $\gamma_{\text{dir}} - h$  pairs in 60 – 92% Au+Au with statistical method. The  $x$ -axis is  $\Delta\phi$ .

#### A.4 Jet Functions with isolation cut method

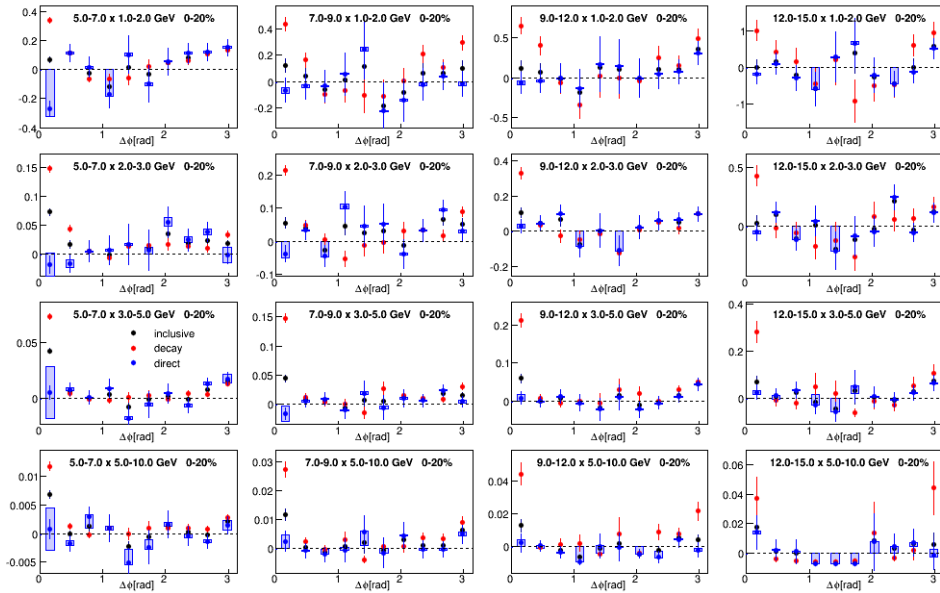


Figure A.29: Jet function of  $\gamma_{\text{inc}} - h$ ,  $\gamma_{\text{dec}} - h$  and  $\gamma_{\text{dir}} - h$  pairs in 0 – 20% Au+Au with isolation cut method. The  $x$ -axis is  $\Delta\phi$ .

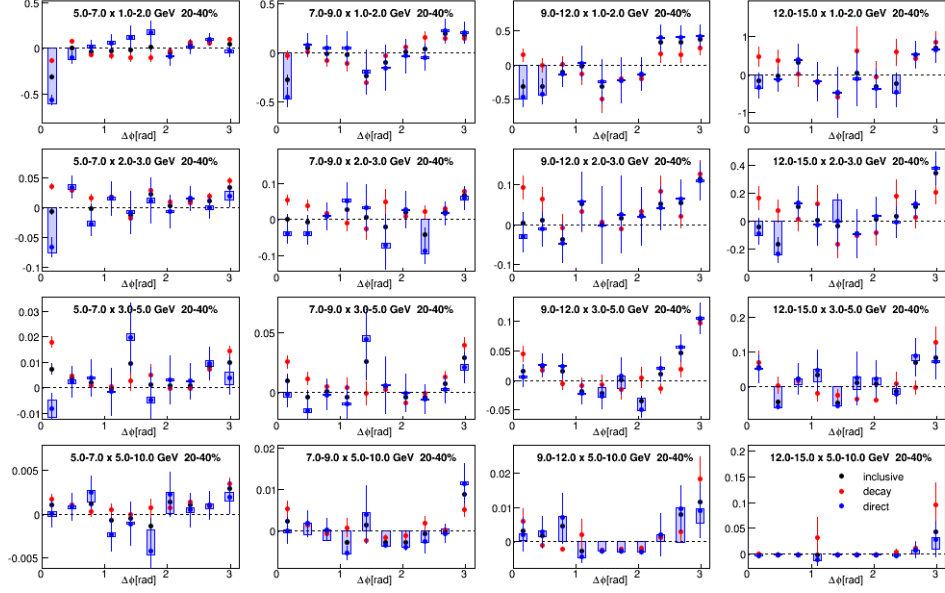


Figure A.30: Jet function of  $\gamma_{\text{inc}} - h$ ,  $\gamma_{\text{dec}} - h$  and  $\gamma_{\text{dir}} - h$  pairs in  $20 - 40\%$  Au+Au with isolation cut method. The  $x$ -axis is  $\Delta\phi$ .

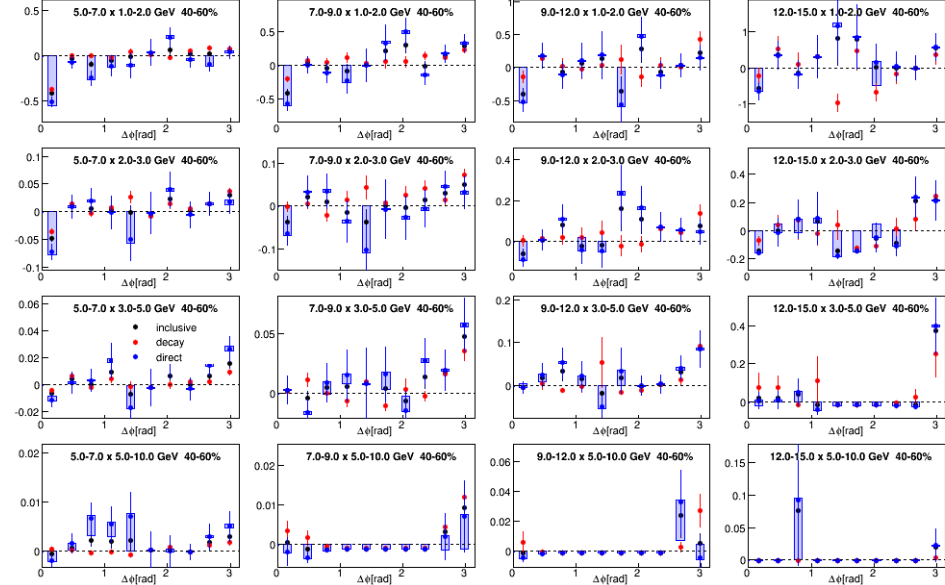


Figure A.31: Jet function of  $\gamma_{\text{inc}} - h$ ,  $\gamma_{\text{dec}} - h$  and  $\gamma_{\text{dir}} - h$  pairs in  $40 - 60\%$  Au+Au with isolation cut method. The  $x$ -axis is  $\Delta\phi$ .

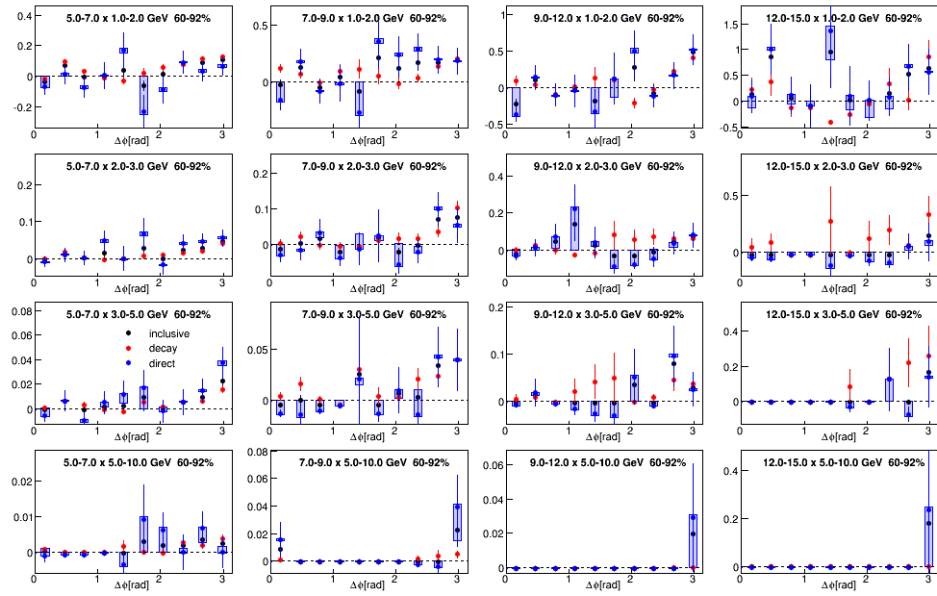


Figure A.32: Jet function of  $\gamma_{\text{inc}} - h$ ,  $\gamma_{\text{dec}} - h$  and  $\gamma_{\text{dir}} - h$  pairs in 60 – 92% Au+Au with statistical method. The  $x$ -axis is  $\Delta\phi$ .